Spring 2015

Freezing-induced deformation of biomaterials in cryomedicine

Altug Ozcelikkale
School of Mechanical Engineering, Purdue University, West Lafayette, IN

Graduate School Form 30
Updated 1/15/2015

PURDUE UNIVERSITY
GRADUATE SCHOOL
Thesis/Dissertation Acceptance

This is to certify that the thesis/dissertation prepared

By Altug Ozcelikkale

Entitled

Freezing-Induced Deformation of Biomaterials in Cryomedicine

For the degree of Doctor of Philosophy

Is approved by the final examining committee:

Bumsoo Han
Chair

Suresh Garimella

Xianfan Xu

Sherry Voytik-Harbin

To the best of my knowledge and as understood by the student in the Thesis/Dissertation Agreement, Publication Delay, and Certification Disclaimer (Graduate School Form 32), this thesis/dissertation adheres to the provisions of Purdue University's "Policy of Integrity in Research" and the use of copyright material.

Approved by Major Professor(s): Bumsoo Han

Approved by: Ganesh Subbarayan 4/28/2015

Head of the Departmental Graduate Program Date

FREEZING-INDUCED DEFORMATION OF BIOMATERIALS IN CRYOMEDICINE

A Dissertation

Submitted to the Faculty

of

Purdue University

by

Altug Ozcelikkale

In Partial Fulfillment of the

Requirements for the Degree

of

Doctor of Philosophy

May 2015

Purdue University

West Lafayette, Indiana

To my wonderful wife, Zeynep

ACKNOWLEDGMENTS

Completion of this dissertation would not be possible without the guidance of my committee members, help from friends, and support from my family.

I would like to express my deepest gratitude to my advisor, Dr. Bumsoo Han, for providing me with a most meaningful and productive research experience through his guidance, caring and patience. I would also like to thank the other members of my advisory committee, Dr. Suresh Garimella, Dr. Xianfan Xu and Dr. Sherry Voytik-Harbin for their valuable feedback in shaping my research projects and dissertation.

I would also like to thank all current and former members of Biotransport Phenomena Lab. (BPL) for their help and friendship especially for all those memorable times that we had fun together while finding humor in rather awkward moments. A special thanks goes to Ka Yaw Teo who has been the mentor and friend I needed during my first year at Purdue. His way of research and sense of responsibility has been guiding my work in BPL since.

I would also like to thank my parents, Gülsen and Levent Özçelikkale, and my sister, Ayça Özçelikkale Hünerli. All the hard work and intellect I put in to come up with this dissertation wouldn't be possible if it wasn't for their love and unconditional support through the years.

Finally, I would like to thank my wife, Zeynep for the ultimate companionship she has provided me with through the years of my studies. As our shared quest in Graduate School is coming to an end, I still can not believe my good fortune for always having her on my side.

TABLE OF CONTENTS

Page

LIST OF TABLES

LIST OF FIGURES

ABSTRACT

Ozcelikkale, Altug PhD, Purdue University, May 2015. Freezing-Induced Deformation of Biomaterials in Cryomedicine. Major Professor: Bumsoo Han, School of Mechanical Engineering.

Cryomedicine utilizes low temperature treatments of biological proteins, cells and tissues for cryopreservation, materials processing and cryotherapy. Lack of proper understanding of cryodamage that occurs during these applications remains to be the primary bottleneck for development of successful tissue cryopreservation and cryosurgery procedures. An engineering approach based on a view of biological systems as functional biomaterials can help identify, predict and control the primary cryodamage mechanisms by developing an understanding of underlying freezing-induced biophysical processes. In particular, freezing constitutes the main structural/mechanical origin of cryodamage and results in significant deformation of biomaterials at multiple length scales. Understanding of these freezing-induced deformation processes and their effects on post-thaw biomaterial functionality is currently lacking but will be critical to engineer improved cryomedicine procedures. This dissertation addresses this problem by presenting three separate but related studies of freezing-induced deformation at multiple length scales including nanometer-scale protein fibrils, single cells and whole tissues. A combination of rigorous experimentation and computational modeling is used to characterize post-thaw biomaterial structure and properties, predict biomaterial behavior and assess its post-thaw biological functionality. Firstly, freezing-induced damage on hierarchical extracellular matrix structure of collagen is investigated at molecular, fibril and matrix levels. Results indicate to a specific kind of fibril damage due to freezing-induced expansion of intrafibrillar fluid. This is followed by a study of

freezing-induced cell and tissue deformation coupled with osmotically driven cellular water transport. Computational and semi empirical modeling of these processes indicate that intracellular deformation of the cell during freezing is heterogeneous and can interfere with cellular water transport, thereby leading to previously unconsidered mechanisms of cell freezing response. In addition, cellular water transport is identified as the critical limiting factor on the amount of freezing-induced tissue deformation, particularly in native tissues with high cell densities. Finally, effects of cryopreservation on post-thaw biological functionality of collagen engineered tissue constructs is investigated where cell-matrix interactions during fibroblast migration are considered as the functional response. Simultaneous cell migration and extracellular matrix deformation are characterized. Results show diminished cell-matrix coupling by freeze/thaw accompanied by a subtle decrease in cell migration. A connection between these results and freezing-induced collagen fibril damage is also suggested. Overall, this dissertation provides new fundamental knowledge on cryodamage mechanisms and a collection of novel multi-purpose engineering tools that will open the way for rational design of cryomedicine technologies.

1. OVERVIEW

We are living in an era that has witnessed development of numerous biotechnologies made possible mainly by application of engineering principles to biological systems. Advances in structural biology and biomedical imaging have led to a new view of proteins, cells and tissues as units of hierarchically organized composite biomaterials whose structures are fine-tuned to achieve specific biological functionalities. By combining this biomaterial view with an engineering framework, it has become possible to (i) identify various biophysical processes using principles of material science, heat transfer, fluid and structural mechanics, and (ii) design, model, preserve or alter biomaterial structure and properties to elicit the desired biological response.

The unified engineering approach has provided solutions to biomedical problems for instance by thermal therapies where patients are treated by locally applied cold or heat to destroy/normalize diseased tissues [1, 2]. Another example is emergence of tissue engineering, an active research area that has enabled the design and development of artificial engineered tissues to fulfill certain native tissue functionalities [3, 4]. Some of the tissue engineering based solutions such as dermal tissue equivalents have already transitioned into commercial products that are being used in clinics [5].

This unified engineering approach can also revolutionize applied cryomedicine by enabling development of new and better technologies for cryopreservation [6–9], freezing based biomaterial processing [10, 11] and cryotherapy [1, 12]. Cryopreservation is made possible by storage of biomaterials at cryogenic temperatures[1] where chemical reactions that drive metabolic activity are slowed down and life is suspended [13].

[1] -80 to -196 °C often realized by either direct contact with liquid nitrogen or storage in gas phase that is in equilibrium with liquid nitrogen.

While the ultimate aim in cryopreservation is recovery of biomaterial's structure and functionality at post-thaw conditions, this prospect currently remains to be elusive especially in tissues due to cryo damage occuring in multiple tissue components during the preservation procedure [7, 14–17]. This is in direct contrast with cryotherapy where damage is deliberately inflicted on *in vivo*[2] tissue by extreme cold. However in this case also, improved control on extent of tissue damage is still highly desired since effectively destroying the diseased tissue while keeping the damage localized to the target site can be difficult to achieve [12]. Therefore a proper understanding of ways cryo damage occurs is important in all cryomedicine applications especially in designing new protocols that will provide improved outcome.

Ice formation has long been recognized as a main source of cryo damage both in isolated cells and in tissues [6, 18]. Conventional treatment of biomaterials with low temperatures results in freezing of physiological solutions. This is marked by formation and growth of ice crystals in tissue interstitial space and possibly interior of the cells. Ice formation is detrimental to cell and tissue structure due to several reasons. First of all, significant deformation occurs in cell and tissues by local volumetric expansion during water-to-ice phase change. In particular freezing in tissues alters the microstructure of extracellular matrix (ECM), a fibrous mesh of proteins surrounding the cell [19]. Similarly intracellular ice formation is considered to destroy subcellular structures and organelles including membrane and cytoskeleton [20–23]. In addition to this direct structural/mechanical effect of ice, freezing also causes indirect changes in biomaterials. Most prominently local expansion of ECM is known to induce pressure gradients that cause redistribution of interstitial fluid [24]. Likewise, solutes excluded from freezing interface lead to a gradual increase in concentration of physiological solutions. When cells are present in the freezing environment, they respond to this

[2]Within the living biological organism. Here *in vivo* refers to tissues in patient's body environment.

concentration increase by excluding part of their water to extracellular space [20]. The cellular water transport is osmotic in nature and causes significant deformation of cell even in the absence of intracellular ice. It is clear that mechanisms of freezing damage with respect to deformation of cells and tissues needs to be considered in the context of both structural/mechanical and transport aspects of ice formation.

Detrimental effects of freezing have been recognized especially in studies of tissue cryopreservation and since then have motivated significant amount of research to develop ice-free cryopreservation techniques. Among those, vitrification in particular has showed promise in preserving post-thaw tissue structure [8, 17]. In vitrification, freezing-induced expansion associated with crystalline ice is circumvented by formation of amorphous (i.e. vitrified) ice. There are multiple reports indicating excellent preservation of tissue structure by vitrification [17, 25]. However this is sometimes overshadowed by its poor performance in preserving cell viability [16, 26]. This drawback is partly explained by the necessity of vitrification to use high concentrations of potentially toxic cryoprotectant cocktails [27]. This, combined with the need for fast cooling limits widespread application of vitrification to bulk tissues. While this situation is likely to change in the future, conventional freezing is still the practical reality of cell and tissue cryopreservation as well as cryosurgery. In all these cases, freezing damage needs to be understood, minimized and controlled.

Effects of cryogenic temperatures on biomaterial structure and functionality have also been considered based on thermodynamic grounds that is irrespective of freezing. There has been a rising concern on appropriateness of low temperature storage for protein preservation, motivated by observations of diminishing protein activity after storage [28–30]. Some recent studies of protein thermal stability have provided a possible explanation to this issue by showing that low temperatures can lead to changes in protein conformational structure referred to as *cold denaturation* in analogy to more

widely known heat induced thermal denaturation [31, 32]. Cold denaturation has been reported for various proteins at above freezing temperatures, often in the presence of destabilizing agents [33, 34], at sub-zero temperatures for proteins that are isolated by nano-confinement [35, 36] and also encountered with cellular proteins under cryogenic storage conditions [37]. These protein-level studies indicate to a second mechanism for cryo damage, which is thermodynamic/biochemical in origin.

There are still unanswered questions that need to be addressed to properly understand cryo damage mechanisms. A particularly important one is how to distinguish between structural/mechanical and thermodynamic/biochemical origins of cryo damage in tissue ECM especially at small length scales. A useful and accurate view of ECM in this respect is that of a hierarchically organized hydrated porous mesh work of collagen formed by self-assembly of tropocollagen protein molecules into fibrils few hundreds of nanometers in diameter [38]. This hierarchy is distinctly identified by tissue, fibril and molecular levels each of which is prone to cryo damage. It has been suggested that freezing-induced changes in ECM tissue level properties such as porosity and hydration are governed by local competing mass transport processes associated with ice formation and redistribution of interstitial fluid. [19, 39]. At a lower length scale, an increase in fibril dimensions and disruption of architecture are also reported. However, the underlying mechanisms of such change are unclear [19, 40–42]. It is possible that a combination of ice formation and destabilizing effects of low temperatures is responsible for changes in collagen fibril and molecular levels, yet the relative importance of the two cryo damage mechanisms are not well identified. A systematic investigation of freezing-induced changes in thermodynamic properties of collagen and its structural evaluation at each level of ECM hieararchy could help identify the dominating mechanism of cryo damage.

An equally important problem is the way cellular water transport is considered with respect to cell and tissue deformation during freezing. The transport of water in suspended cells is traditionally identified by a membrane limited transport process [43] but it also needs to be considered as a main source of deformation in intracellular structures. This deformation can potentially interact and even interfere with the water transport. Furthermore when freezing occurs in cell-laden tissues, cellular water transport can happen simultaneously with freezing of interstitial fluid and can provide an excess amount of water for extracellular freezing. Then the local rate of tissue expansion will depend on both ice formation kinetics and rate of cellular water transport. Understanding the currently unexplored interactions between freezing, intracellular/extracellular deformation and cellular water transport can provide explanations to observed cell and tissue type dependence in freezing responses [7, 44].

Studies addressing above problems will provide new relations for post-thaw tissue structure and properties as well as conceptual information on fluid-structure interactions that occur during freezing. These results will need to be complemented by applied studies on assessment of post-thaw tissue functionality to identify *practically important* aspects of cryo damage.

This dissertation contributes to the broad field of work on cryomedicine by addressing the above problems through a combination of experimental characterization and computational biophysical modeling. Experimentation involves characterization of post-thaw biomaterial properties including thermodynamic stability, mechanical stiffness and hydraulic conductivity. Biomaterial structure is assessed by various microscopy techniques including fluorescence and scanning electron microscopy. Furthermore, dynamics of cell and tissue level deformation are characterized by two time-resolved image based deformetry techniques, namely fluorescence particle track-

ing cryomicroscopy and incremental particle image velocimetry. Biophysical processes are modeled by principles of structural mechanics and transport in porous medium. In particular, representative elementary volume analysis [45, 46] and poroelastic formulation [47, 48] are used to predict biomaterial behavior and perform property estimation based on comparison with experiments.

Chapter 2 presents a study on collagen ECM hierarchy that explores how F/T induced thermal stability changes of collagen are related to its distinct structures at matrix, fibril and molecular levels. Measurements of post-thaw thermal stability by modulated temperature differential scanning calorimetry together with morphological examination of collagen fibrils and matrix by scanning electron microscopy indicate to a specific type of fibril deformation that involves expansion of intrafibrillar space as a result of ice formation. Solely thermodynamics effects of low temperatures on collagen thermal stability remain secondary when compared to fibril deformation. The results are supported by simulations of a computational model developed to relate changes in thermal stability to expansion of collagen fibrils.

Chapter 3 focuses on osmotically driven cellular water transport that occurs during freezing [49]. In the first part of this study nonuniform intracellular deformation is proposed as a new additional mechanism that governs cellular water transport. A novel computational model that considers cytoplasm as a porous structure saturated with interstitial fluid is developed. The model simulations are compared to intracellular deformation measurements performed by fluorescence particle tracking cryomicroscopy. Results indicate to a previously unreported role of intracellular structure in cell osmotic response that involves gradual collapse of outer layers of the cytoplasm by water efflux and that can also result in entrapment of water in the cell by a hydraulic locking effect. In the second part of Chapter 3 the role of cellular water transport in freezing-induced tissue deformation is investigated by development of a semi-empirical representative

elementary volume model [50]. In this model, tissue freezing-induced expansion is simulated based on experimentally determined freezing kinetics and cellular water transport characteristics. Results of these simulations indicate that cellular water transport becomes the critical limiting factor of freezing-induced deformation when cells are present at native tissue like concentrations.

Chapters 2 and 3 are mainly focused on identification of biophysical processes that occur during freezing and determination of post-thaw structure-property relations. Chapter 4 presents an applied study that builds on this knowledge to assess post-thaw tissue functionality. Freezing effects on collagen ECM are relevant to cryopreservation of collagen based engineered tissue constructs. These biomaterials are used as a provisional matrix for improved healing of deep tissue wounds [5]. Interactions of fibroblast with the ECM defines the main functional response that needs to be preserved upon cryopreservation of the construct. In this study, effects of F/T on complex cell-ECM interactions that involve both cell migration and matrix deformation were investigated on acellular collagen hydrogels using a newly developed image based tissue deformetry technique. Results indicate to decreased cell-mediated matrix deformation in the case of F/T suggesting that freezing-induced changes in collagen structure adversely affect cell-matrix adhesion.

2. THERMAL DESTABILIZATION OF COLLAGEN HIERARCHICAL STRUCTURE BY FREEZE/THAW

2.1 Introduction

Collagen is the primary structural component of tissue extracellular matrix (ECM) and plays a critical role for tissue integrity and mechanical strength. Collagen ECM is also an integral part of the cell mechanical environment that directs cellular processes such as proliferation, differentiation and migration through cell-matrix interactions [51]. Because of its wide biological functionality, collagen is also used as biomaterial for studying cell and tissue behavior in vitro and developing scaffolds for tissue engineering applications [4, 52].

Thermal insult of collagen by exposure to temperatures lower or higher than physiological levels is encountered in a variety of applications. Frostbite and burn injuries are practical examples of detrimental effects of extreme temperatures. During cryopreservation, tissues are exposed to extreme cold and stored at cryogenic temperatures for an extended period of time. Preservation of tissue structure and functionality post-thaw are highly desired but there has only been limited success in this area due to freezing damage occurring at multiple tissue components [7, 14–17]. Other applications include thermal therapies such as cryosurgery, hyperthermia and thermal ablation that utilize cold or heat to destroy diseased tissues [1, 2]. Proper evaluation and prediction of the extent of thermal damage are of the uttermost importance for the success of these techniques. Understanding how collagen ECM structure is affected by heat, cold or a combination of both could help develop improved cryopreservation and thermal therapy modalities.

Collagen ECM is a hydrated porous meshwork hierarchically organized from mechanically entangled and chemically cross-linked fibrils formed by self-assembly of tropocollagen molecules [38]. This hierarchical structure is distinctly identified by tissue, fibril and molecular levels, each prone to damage by low temperatures and/or mechanical and osmotic stress induced by freeze/thaw (F/T). It has been reported that freezing-induced changes in ECM tissue level properties such as porosity and hydration are governed by local competing mass transport processes associated with ice formation and redistribution of interstitial fluid. [19,39]. At a lower length scale, an increase in fibril dimensions and disruption of architecture are also reported. However, the underlying mechanisms of such change are unclear [19, 40–42]. It is possible that the mechanisms involving ice formation and fluid transport also contribute to changes in collagen fibril organization.

In the above view thermodynamic effects of low temperatures on collagen molecule are not involved. However it is well known that collagen, like all proteins, has limited thermal stability. At temperatures exceeding its thermal stability limit, collagen undergoes a conformation change where its native triple-helical tertiary structure unfolds and transitions into a more disordered configuration. In addition to that, destabilizing effects of low temperatures on proteins has also long been a concern [28]. There is now substantial evidence that proteins can have a lower temperature limit for their stability that is marked by cold denaturation (or unfolding), a transition analogous to heat induced thermal denaturation [31, 32]. Cold denaturation has been reported for various proteins at above freezing temperatures, often in the presence of destabilizing agents [33, 34], at sub-zero temperatures for proteins that are isolated by nano-confinement [35, 36] and also encountered with cellular proteins under cryogenic storage conditions [37]. However, whether collagen ECM in a physiological tissue

environment maintains its thermal stability at sub-zero temperatures remains to be unknown.

Evaluation of collagen structure and properties in aqueous and physiologically relevant environment are important for proper characterization of real tissue behavior. However under these settings it becomes difficult to obtain direct measurements of F/T induced protein thermal processes due to interference from water-to-ice phase change and subsequent presence of ice in the sample. On the other hand, heat induced thermal denaturation conveniently occurs above phase change temperature and can be characterized by multiple measurement techniques including differential scanning calorimetry (DSC) [53–55], second harmonic generation microscopy [56] and circular dicroism [57]. Therefore it is hypothesized that the post-thaw structural and thermodynamic state of collagen can be characterized by measuring thermal denaturation and relate those to events that take place during F/T. A similar approach has been previously employed to determine protein freezing denaturation in AT-1 prostate tumor cells [37]. Furthermore, F/T induced structural damage to collagen can also be estimated based on established relations between the denaturation temperature and collagens fibrillar packing [58]. There are only a few studies that report post-thaw denaturation metrics in cryopreserved collagenous tissues. A net decrease in denaturation temperature was observed in tendons stored at -80 °C [40]. In contrast, thermal stability was enhanced after the F/T of arteries [39]. These tissue dependent results indicate a clear need for systematic characterization of thermal stability of collagen hierarchical structure upon F/T and identification of specific damage mechanisms associated with observed changes in thermal stability.

In this study, we address this gap by providing measurements of post-thaw collagen thermal stability using modulated temperature differential scanning calorimetry (MTDSC). Measurements were performed on both collagen molecular solutions and

hydrogels with different collagen concentrations. Since hydrogels exhibit a fibrous mesh microstructure that is absent in molecular solution, it was possible to relate the F/T induced thermal stability changes of collagen to its distinct structures at matrix, fibril and molecular levels. In addition, morphological examination of collagen fibrils and network were performed with SEM and a rudimentary model explaining freezing-induced structural damage of collagen based on its post-thaw thermal stability was developed. Our findings indicate to a specific type of fibril damage that involves expansion of intrafibrillar space as a result of ice formation.

2.2 Materials and Methods

2.2.1 Collagen

Collagen (fibrillar) hydrogels were prepared from rat tail collagen type-1 solution (Corning) at final collagen concentrations of 3 and 6 mg/mL. A neutralized collagen solution with isotonic ionic strength was obtained by mixing appropriate amounts of 10X Dulbecco's Phosphate-Buffered Saline (10X DPBS, Life Technologies), 1.0 N NaOH and cell culture grade distilled water with the collagen stock. The neutralized collagen solution was then dispensed into chamber slides (Nunc™ Lab-Tek™ II, Thermo Scientific) and allowed to polymerize for 1 hour at 37 °C in a CO_2 incubator. Then isotonic saline solution (1X DPBS) was added on top of the hydrogel to prevent dehydration and incubation was continued overnight and until the experiments.

Collagen molecular solutions were prepared from a rat tail collagen type-1 stock solution that was diluted to a final concentration of 3 mg/mL in 20 mM acetic acid. This preparation prevented collagen assembly during experiments since the pH of the solution was below collagens isoelectric point.

2.2.2 MTDSC Measurements

Differential scanning calorimeter (Q200, TA Instruments) was calibrated with indium, water and sapphire prior to experiments. Circular sections of hydrogels were cut with a 3 mm biopsy punch and placed in DSC pans. For molecular solution experiments, 10 μL of solution was directly dispensed in the DSC pan. Pans were hermetically sealed to prevent dehydration during the experiments. Samples prepared following this procedure weighted between 5 and 15 mg.

Experiments involved heating from 25 to 60 °C (molecular solution) or 30 to 65 °C (hydrogel) with an underlying heating rate of 1 °C/min. A sinusoidal temperature modulation with amplitude of 0.75 °C and a period of 80 s was superimposed on the underlying linear temperature program. Measurements were performed 3-4 times for each treatment group and results were averaged based on standard statistical methods.

2.2.3 Freeze/Thaw Treatments

For freezing temperature studies, samples were cooled to either -20 °C or -60 °C in the DSC cell at a rate of 50 °C/min, kept isothermal for 2 minutes and warmed back to 20 °C with 50 C/min. MTDSC measurements were initiated within 10 minutes of thawing.

In order to investigate the effects of ice formation, sample in DSC pan was placed on a temperature controlled stage (MDS 600, Linkam, U.K.). The sample was monitored for ice nucleation while stage temperature was decreased to -15 °C with a rate of 10 °C/min and maintained at that temperature for 2 minutes. Small volume of the DSC sample enabled substantial supercooling allowing it to remain ice-free unless ice nucleation was deliberately induced by a liquid nitrogen cooled needle. Ice formation

controlled this way enabled preparation of samples that were either supercooled and ice-nucleated or supercooled only.

Different ice formation kinetics were obtained with a procedure similar to above. Samples were first cooled to -2 °C where ice was nucleated and presence of small ice crystals in the sample was verified under microscope. Then, the samples were cooled to -20 °C with two different cooling rates at 1 or 50 °C/min. These two cooling rates were observed to generate different rates of ice growth in the samples.

For scanning electron microscopy, collagen samples prepared in chamber slides were placed on a directional solidification stage [24] and frozen by a temperature gradient developed from -60 °C to 4 °C across a 6 mm gap. During this process only half of the sample was frozen while the rest remained unfrozen.

For experiments with cryoprotectant dimethyl sulfoxide (Me_2SO, DMSO), hydrogels were incubated in saline solution including DMSO at concentrations ranging between 0.25 M and 1 M for 30 minutes before freezing. After 10 minutes of passive thawing at room temperature, samples were sectioned and transferred to DSC pans followed by freezing in the DSC cell as explained before. Since DMSO in the hydrogels was not unloaded after F/T samples contained DMSO during the MTDSC measurements. In order to control for confounding effects of DMSO in the measurements, experiments were also performed on DMSO loaded unfrozen collagen hydrogels and the results were compared with 0 M DMSO case.

2.2.4 Scanning Electron Microscopy Imaging

Hydrogels were F/T on a directional solidification stage as described above and passively thawed at room temperature for 15 minutes. The samples were then immediately fixed with 2.5% glutaraldehyde and 2% formaldehyde in 1X DPBS and stored in fixation solution at +4 °C overnight. Afterwards circular sections

were punched out from unfrozen and F/T regions, dehydrated against ethanol and dried in a CO_2 critical point dryer. Through the sample preparation, the sizes of specimens unfrozen or F/T with DMSO remained unchanged while notable shrinkage was observed for the specimens frozen and thawed without DMSO. Specimens were then imaged using a scanning electron microscope (Nova NanoSEM 450, FEI, OR). At least 3 randomly selected fields of views were imaged per sample. The fibril diameters were estimated by manually tracing the boundaries of approximately 100 fibrils per each group using ImageJ [59].

2.2.5 Kinetic Model of Collagen Denaturation

In this study, we considered collagen thermal denaturation as a single step irreversible rate reaction based on earlier work of Miles et al. [53]. The denaturation reaction is,

$$N_{UF} \overset{k_{UF}}{\rightarrow} D_{UF} \text{ and } N_{F/T} \overset{k_{F/T}}{\rightarrow} D_{F/T} \tag{2.1}$$

Here N and D are the native and denatured states of collagen, respectively. Both unfrozen (UF) and frozen/thawed (F/T) collagen is assumed to go through the same reaction but at possibly different rates. For both UF and F/T, kinetics of denaturation is described by the rate law,

$$\dot{\alpha} = k(T)f(\alpha) \tag{2.2}$$

where α is the extent of conversion from native to denatured state, $\dot{\alpha}$ is the conversion rate, k is the rate constant and f is the reaction model. We assumed Arrhenius type temperature (T) dependence for the rate constant and an nth order reaction model [60] as follows:

$$k(T) = A \, \exp\left(\frac{-E_a}{RT}\right), \; f(\alpha) = (1-\alpha)^n \tag{2.3}$$

In Equation (2.3) A is commonly referred to as pre-exponential factor and E_a is the activation energy. These together with the reaction order n, are the kinetic parameters that are to be estimated by fitting the above model to experimental data. The fitting procedure used in this study is due to earlier work of Borchardt and Daniels [61]. Rearranging Equations (2.2) and (2.3) and taking the logarithm of both sides,

$$\ln(k) = \ln\left(\frac{\dot{\alpha}}{(1-\alpha)^n}\right) = \ln(A) - \frac{E_a}{RT} \tag{2.4}$$

Therefore a linear relationship exists between ln(k) and the reciprocal of temperature. Here, α and $\dot{\alpha}$ are derived from DSC endotherm peak. Then, if n is known E_a and A can be estimated from the slope and intercept of a line best fitting the experimental data. The goodness of fit is often measured by:

$$R^2 = 1 - \frac{\sum (y_e - y_m)^2}{\sum (y_e - \bar{y}_e)^2} \tag{2.5}$$

Given experimental data points, y_e, model predictions y_m and mean of experimental data, $\bar{y}_e$. An optimal value of n is assumed to scale the experimental data such that R^2 obtained from the linear best fit is maximized. The search for optimal n was performed by a black-box optimization routine developed in MATLAB®. Once n was determined E_a and A were estimated as described above. Only conversion levels between 0.10 and 0.90 were considered in the analysis. Finally, DSC thermograms were simulated using the estimated parameters in the kinetic model and another set of R^2 parameters were calculated based on the comparison of these simulations with the corresponding experimental profiles. Only kinetic parameters that resulted in excellent fits ($R^2 > 0.995$) were included in further analysis.

2.2.6 Theoretical Model of Fibril Expansion and Thermal Stability

The increase of thermal stability of collagen upon assembly into fibrils is based on the reduction of configurational entropy due to molecular confinement effects [58, 62]. Therefore the observed decrease in thermal stability upon freezing of fibrils is expected to be due to relaxation of the confinement. This entropic destabilization effect can be expressed as a relationship between activation entropy of denaturation $\Delta S^{\updownarrow}$, and confinement diameter, d, based on statistical mechanics modeling of a polymer in a tube [58, 63],

$$\Delta S^{\updownarrow} = \Delta S_o^{\updownarrow} - \frac{4\pi R N b^2}{d^2} \tag{2.6}$$

where $\Delta S_o^{\updownarrow}$ is the activation entropy of denaturation under unconfined state, such as dilute molecular solution. N is the number of links in the thermally labile domain of collagen ($N = 65$ [58]), b is the effective bond length that is taken to be same as the actual bond length ($b = 0.35$ nm [58]) and R is the universal gas constant. During this derivation, it is assumed that the activated state of collagen acts as a Gaussian chain while the native triple helix is a rigid worm-like polymer. Therefore confinement effects become significant only for the activated state [64, 65]. The activation entropy is related to the pre-exponential factor, A, in the previously described kinetic model as:

$$A = B(T) \exp\left(\frac{\Delta S^{\updownarrow}}{R}\right) \tag{2.7}$$

where $B(T)$ is a slowly varying function of temperature [66]. By considering Equations (2.6) and (2.7) for an arbirary configuration with confinement diameter d_2 in comparison to a reference configuration with confinement diameter d_1,

$$\frac{A_2}{A_1} = \exp\left[4\pi N b^2 \left(\frac{1}{d_1} - \frac{1}{d_2}\right)\right] \tag{2.8}$$

Therefore, reaction kinetics of an arbitrary confinement level can be predicted based on the reaction kinetics and confinement level of the reference state.

Freezing induced expansion of fibril was modeled by a unit cell / representative volume approach that was previously used for modelling freezing-induced expansion of tissues [50]. The periodic molecular arrangement in fibril was represented with a hexagonal unit cell that expands by freezing of intrafibrillar fluid as shown in Figure 2.7A. The relative increase in unit cell dimensions is given by:

$$\frac{d_c^*}{d_c} = \sqrt{1 + \phi\left(\frac{\rho_f}{\rho_i} - 1\right)} \tag{2.9}$$

where d_c is the side of the unit cell and phi is the fibril porosity at unfrozen state. d_c^* is the side of the unit cell at frozen state. ρ_f and ρ_i are the densities of intrafibrillar fluid and ice. Porosity is calculated from geometric relationships as:

$$\phi = 1 - \frac{\pi}{2\sqrt{3}}\left(\frac{d_m}{d_c}\right)^2 \tag{2.10}$$

where d_m is the collagen molecular diameter that was varied between 1.3 and 1.5 nm [58, 67]. The confinement diameter is obtained as $d = 2d_c - d_m$ again based on unit cell geometry. Equations (2.8) and (2.9) were used together with kinetic model to predict the denaturation temperature depression with freezing-induced fibril expansion.

2.2.7 Statistical Analysis

Differences in treatment means were tested by one-way ANOVA. Multiple comparisons were performed by Tukeys test. The differences were considered statistically

significant when p-value was less than 0.05. Experimental data are reported in terms of mean ± standard deviation unless otherwise is noted.

2.3 Results and Discussion

2.3.1 Denaturation Endothermic Peak in MTDSC Thermograms

Denaturation endothermic peak in MTDSC thermograms Heat absorbed by collagen during thermal denaturation results in an endothermic peak in a typical DSC heating thermogram where the temperature is increased at a constant rate with time. In our experiments, we used a sinosoidal temperature modulation superimposed on constant heating rate. The resulting MTDSC technique enabled deconvolution of specific heat signal into two components that distinguish processes that are irreversible or reversible within the timescale of modulation period [68].

Figure 2.1A shows the three specific heat signals obtained from a representative MTDSC thermogram for collagen hydrogel. The total signal is the summation of reversing and non-reversing components and is equivalent to the signal that would be obtained by standard DSC. Collagen heat denaturation appeared as a distinct endothermic peak in non-reversing specific heat and was associated with only a subtle increase in reversing specific heat. The change in non-reversing specific heat is attributed to heat absorption associated with the denaturation reaction and is similar to what has been reported with conventional DSC [53]. The relatively small change in reversing specific heat is attributed to the sensible heat transfer to the sample and indicates an increase in partial specific heat upon denaturation of fibrillar collagen. This positive change is in agreement with previous studies [54]. The distinct peak in non-reversing signal provides more information on denaturation and is associated with higher signal-to-noise ratio than the reversing signal. Therefore, quantification

Table 2.1. Collagen thermal denaturation characteristics for selected treatments. Values are reported as mean ± standard deviation.

Sample	Treatment	DMSO Conc. (M)	T_d (°C)	$\Delta T_{1/2}$ (°C)	ΔH_d (J/g collagen)
Hydrogel	F/T -60 °C	0	44.17 ± 0.07	3.00 ± 0.13	114 ± 23
	F/T -60 °C	0.25	44.16 ± 0.35	3.17 ± 0.81	88 ± 43
	F/T -60 °C	0.5	45.19 ± 0.16	2.92 ± 0.21	80 ± 16
	F/T -60 °C	1	45.41 ± 0.16	2.46 ± 0.49	53 ± 45
	UF	-	45.71 ± 0.32	2.57 ± 0.23	79 ± 28
Molecular Solution	F/T -60 °C	-	38.76 ± 0.07	1.97 ± 0.05	52 ± 2
	UF	-	38.59 ± 0.04	1.99 ± 0.05	48 ± 7

Notes: DMSO: Dimethyl sulfoxide (ME_2SO) T_d : denaturation temperature, $\Delta T_{1/2}$: peak width at half height, ΔH_d : denaturation enthalpy.

of denaturation metrics was done using the non-reversing signal. Denaturation temperature, T_d was determined based on the location of maximum specific heat after subtraction of a linear baseline from the original signal. Peak width at half height, $\Delta T_{1/2}$ which indicates the temperature span of the transition and denaturation enthalpy, ΔH_d i.e. the area under the endothermic peak are also calculated from the baseline subtracted thermogram. T_d, $\Delta T_{1/2}$ and ΔH_d are reported for selected treatments in Table 2.1.

2.3.2 Thermal Destabilization of Collagen ECM upon F/T

Using MTDSC, we discovered that F/T treatment has a destabilizing effect on collagen ECM. Thermal stability of collagen hydrogels after F/T was found to be consistently lower than that of unfrozen control (UF). This is illustrated by the denaturation peaks shown in Figure 2.1B. The denaturation peak of the F/T hydrogels occurred at lower temperatures compared to UF. However, a similar shift in temperature was not observed for F/T molecular solution.

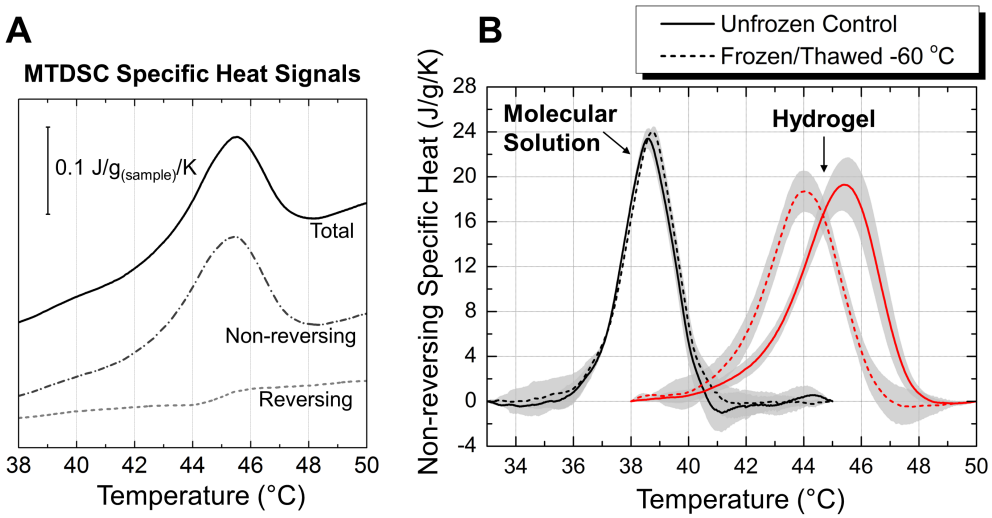

Figure 2.1. (A) Representative MTDSC heating thermograms that show collagen thermal denaturation in multiple specific heat signals. (B) Denaturation peaks of frozen/thawed versus unfrozen collagen in hydrogel and molecular solutions. Lines and shaded regions indicate the mean and standard deviation respectively.

Figure 2.2 shows T_d for collagen molecular solutions and hydrogels after F/T treatments. Collagen as a macromolecule maintains its level of thermal stability even after F/T to -60 °C (Figure 2.2A). $\Delta T_{1/2}$ and ΔH_d of F/T and UF for molecular solution were also considerably close with differences being not statistically significant (Table 2.1). In the case of hydrogels on the other hand, F/T resulted in a significant decrease in T_d regardless of the freezing temperature, -20 °C or -60 °C. The amount of the decrease was between 1.4 and 1.6 °C and also did not depend on collagen density of the hydrogel ($p > 0.05$) (Figure 2.2A).

There are several important implications of the results presented above. First of all, if there are any changes that take place during F/T at collagen molecular level, possibly through cold unfolding, those changes are not reflected in the post-thaw thermal stability. Secondly, unlike single collagen molecules in solution, stability of collagen in hydrogel is affected by F/T suggesting there might be structural changes at fibril or matrix level that are responsible for the observed decrease in Td. In addition our results indicate the extent of this F/T effect is indifferent to varying network architectures generated by different concentration of collagen in ECM. Therefore matrix level properties such as porosity are ruled out as factors related to changes in thermal stability. To this end, fibril appears to be the level of collagen ECM hierarchy that is most related to the measured destabilization of collagen by F/T. As a result it is possible to explore the previously unexplained F/T induced changes in fibril dimension and architecture [19, 40–42] using post-thaw thermal denaturation measurements.

2.3.3 Ice Formation

In light of above findings, we anticipated that F/T induced structural changes of collagen ECM takes precedence over purely thermodynamic effects of low temperatures in determining the change in post-thaw thermal stability. We therefore investigated

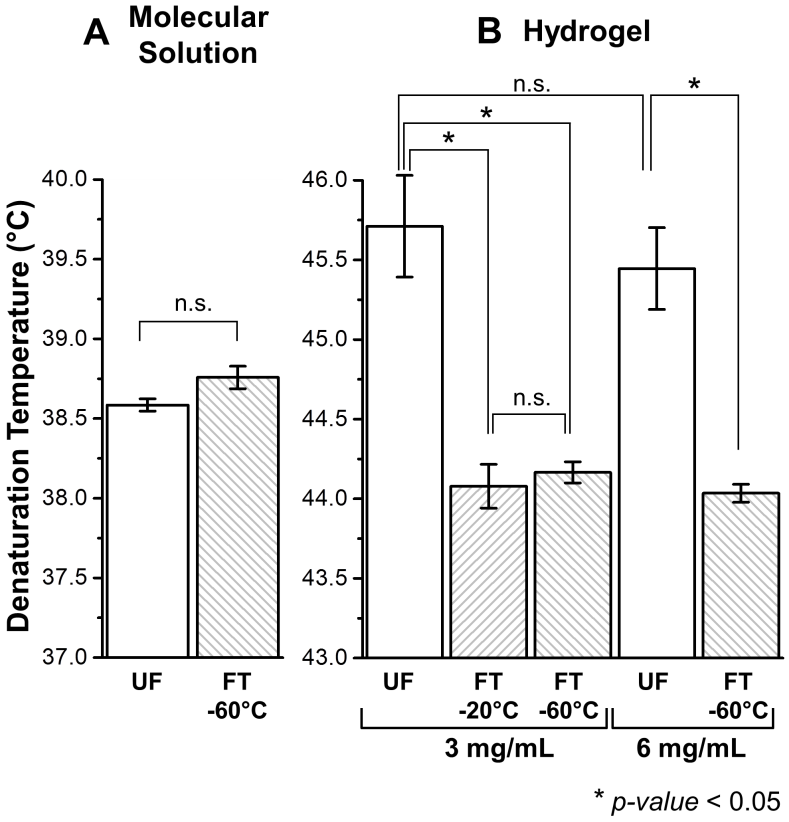

Figure 2.2. Denaturation temperature of collagen in (A) hydrogel and (B) molecular solution.

whether ice formation had any role in the observed changes in thermal stability. Prior to MTDSC, samples were super-cooled to -15 °C on a temperature controlled stage where ice was manually induced in a group of samples while the others remained ice-free. Consistent with the previous results, the hydrogels that experienced ice formation denatured at a significantly lower temperature than UF (Figure 2.3). Furthermore the T_d decrease caused by ice formation was comparable to those from freeze/thaw at -20 °C and -60 °C. Interestingly hydrogels that have undergone the same temperature history but without ice also had a slightly lower T_d than UF but the difference was not statistically significant. Therefore we concluded that ice formation is the dominant mechanism for the destabilization of collagen. For the temperature regime studied (-15 °C to -60 °C), purely thermodynamic effects of low temperatures were indeed found to be secondary when compared to effects of ice formation.

2.3.4 Freezing-induced Fibril Expansion

The seemingly spontaneous effect of ice formation on thermal stability resembles freezing-induced expansion of engineered tissues where tissue deforms due to water-to-ice phase change of interstitial fluid. In that case local amount of deformation depends on the balance between rates of ice formation and redistribution of interstitial fluid [24, 50, 69, 70]. Likewise, we hypothesized that collagen fibrils are deformed due to internal stresses generated by freezing-induced expansion of intrafibrillar fluid. From statistical mechanical point of view, such change in fibril packing would be consistent with the decrease of T_d. It is theoretically established for proteins in general [62] and has been experimentally demonstrated for collagen in particular that changes in confinement of collagen in fibrils through dehydration or addition of crosslinkers has an impact on its denaturation temperature [58, 71]. In particular, decreasing confinement is expected to destabilize native collagen by decreasing the entropic cost of

unfolding. Based on this theory, freezing-induced expansion of fibril will also decrease the confinement of collagen in fibril and result in a decrease in thermal stability that is consistent with the experiments.

We next considered the possibility whether the amount of fibril expansion can depend on the rate of ice formation. Ice formation kinetics may indeed be important if exclusion of intrafibrillar fluid from fibril is fast enough to relieve some of the pressure increase caused by ice formation. If this is the case then faster cooling rates should result in larger amounts of expansion and greater Td depression. To test this hypothesis, ice was nucleated in the samples at just below the phase change temperature and the samples were cooled to -20 °C with either 1 or 50 °C/min. It was indeed found that 50 °C/min resulted in slightly lower T_d than 1 °C/min as shown in Figure 2.3, however the difference between 1 °C/min and 50 °C/min was not statistically significant. This result suggests that ice formation results in bulk expansion of fibril and that intrafibrillar transport of water may not be a significant determinant of freezing-induced expansion of fibril.

2.3.5 Recovery of Collagen Post-thaw Thermal Stability by Use of a Cryoprotectant

During cryopreservation, cells and tissues are often loaded with cryoprotectants such as dimethyl sulfoxide (DMSO) that helps reduce freezing damage by decreasing the amount of phase-change induced expansion [72]. It is therefore hypothesized that use of DMSO during F/T will decrease the change in Td by reducing the amount of freezing-induced expansion of collagen fibrils. Hydrogels were treated with up to 1 M DMSO in physiological buffer prior to freeze/thaw treatment. The results are shown in Figure 2.4. It was indeed observed that the thermal stability of frozen-thawed hydrogels were gradually recovered to unfrozen levels with increasing concentration of DMSO. On the other hand, DMSO did not change the denaturation temperature

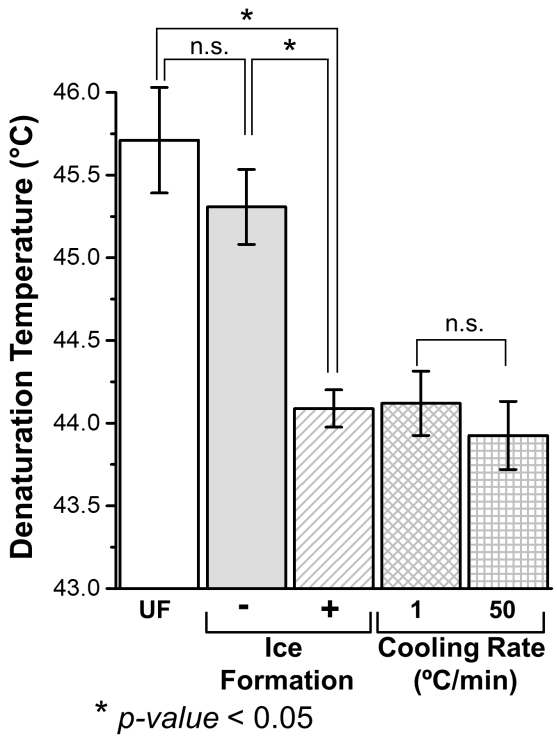

Figure 2.3. Effects of F/T conditions on post-thaw denaturation temperature. * indicates statistically significant difference ($p < 0.05$).

of unfrozen controls. Concentrations above 0.25 M DMSO effectively increased the denaturation temperature and 1 M DMSO was sufficient for almost complete recovery of thermal stability in frozen and thawed samples.

Examination of collagen hydrogel microstructure with scanning electron microscopy revealed dramatic changes in both network and fiber level upon F/T as shown in Figure 2.5A. Hydrogels frozen with and without DMSO both showed large pores (white arrows in top panel) that were not present in unfrozen controls. The sizes of these pores were not comparable due to differential shrinkage of SEM specimens during preparation. The case of 0.5 M DMSO showed fibrils bundled together. F/T in the absence of DMSO also disrupted the fibril morphology. The case of 0 M DMSO showed collection of thin filaments with a mean diameter of $d = 18.1 \pm 4.1$ nm (yellow arrows, bottom middle). These filaments seemed to be a part of multiple, thick but loosely packed bundles ($d = 83.9 \pm 36.0$ nm) which could have originated from fibrils that have unraveled during F/T due to expansion. This was in contrast to the smooth, uniformly sized fibrils observed in unfrozen control ($d = 43.3 \pm 7.4$ nm). The extent of this fibril level damage was alleviated by use of DMSO during freezing. The case of 0.5 M DMSO also showed mostly intact fibrils with diameters, $d = 42.9 \pm 9.4$ nm, similar to that of unfrozen control. The distributions of fibril diameters are shown in Figure 2.5B.

2.3.6 Modeling of Thermal Destabilization Based on Freezing-induced Fibril Expansion

A rudimentary computational model was developed to better explain the measured trends of T_d by freezing-induced fibril expansion. The model is based on Polymer-in-a-box model that has been previously used to explain the effects of dehydration on collagen thermal stability limit [58, 63]. First, kinetic parameters necessary to

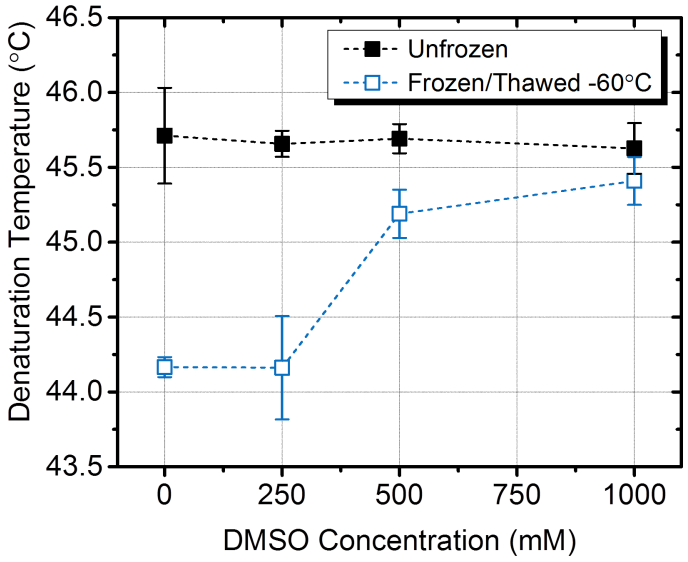

Figure 2.4. Recovery of collagen post-thaw thermal stability by use of cryoprotectant, DMSO.

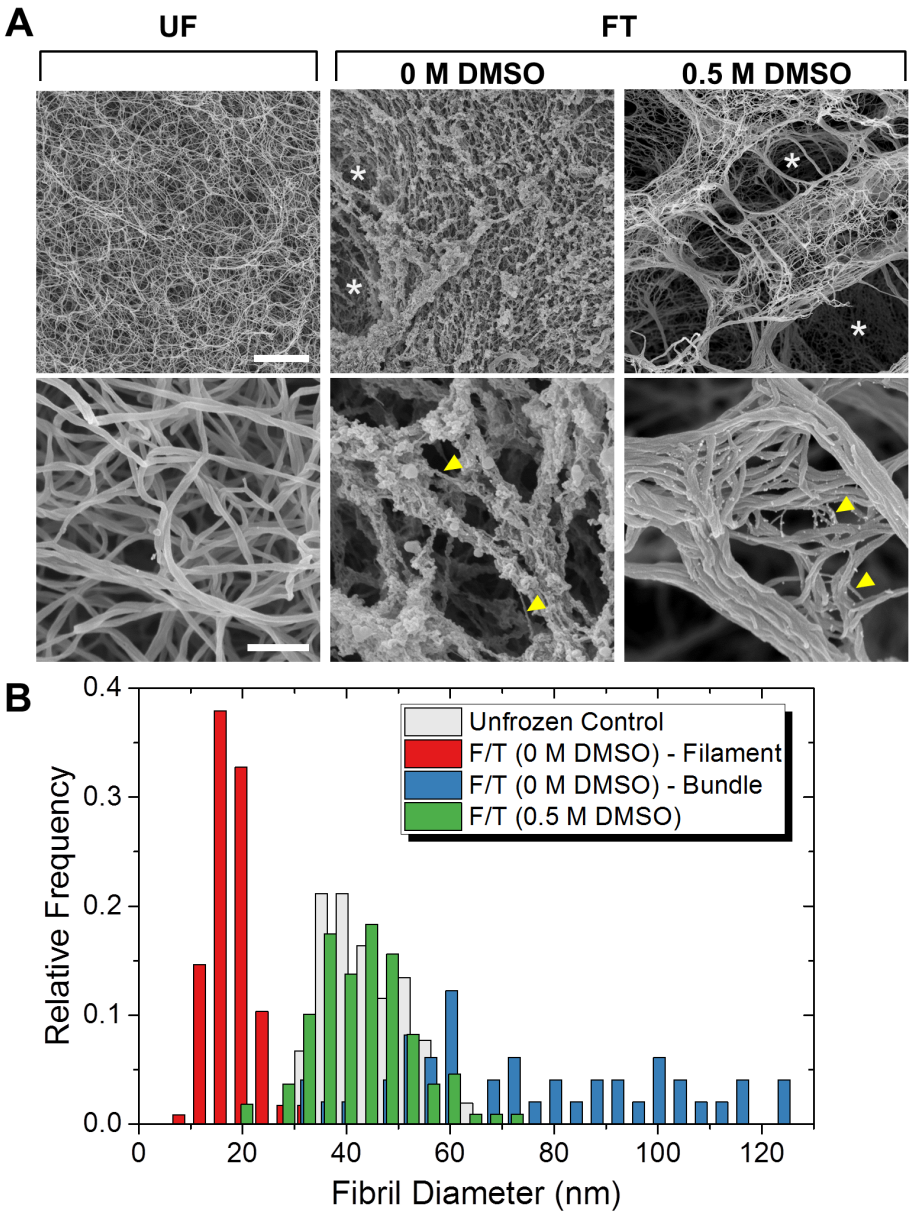

Figure 2.5. (A) SEM images showing the freezing-induced morphological changes in collagen hydrogels at network (top) and fibril level (bottom). Scale bars are 5 μm and 500 nm for top and bottom panels respectively. (B) Hydrogel fibril diameter distributions.

simulate thermal denaturation were determined by fitting an irreversible rate law to experimental thermograms. The Arrhenius coefficients and reaction order were determined from the Arrhenius plot as illustrated in Figure 2.6A. Thermograms that were simulated using these set of parameters were in excellent agreement with ones experimentally determined ($R^2 > 0.996$ for hydrogels and $R^2 > 0.978$ for molecular solution) (Figure 2.6B). The best fitting values of model parameters, reaction order, n, activation energy E_a, and the pre-exponential factor A are reported in Table 2.2 for selected F/T and UF cases.

Then freezing-induced expansion of a collagen fibril was modeled by considering an quasi-hexagonal unit cell as shown in Figure 2.7A depicting a single tropocollagen molecule surrounded by six other neighbors. The space between the molecules are filled with intrafibrillar fluid. Upon freezing, the unit cell expands. The amount of this expansion mainly depends on UF porosity. The redistribution of intrafibrillar fluid was neglected since it was considered to be insignificant based on our experiments with different cooling rates (see Figure 2.3). Upon expansion the confinement diameter, d, increases resulting in a decrease in level of collagen molecular confinement in fibril. Details of the model are provided in Material and Methods section.

Figure 2.7B shows the change in Td as a function of fibril expansion in the case of a tightly packed fibril. It is seen that even a small amount of increase in fibril volume, less than 2%, results in significant decrease of T_d. The effect is almost linear and shows small variation with respect to reported values of collagen molecular diameter [58, 67]. Figure 2.7C shows the effect of unfrozen fibril porosity on freezing-induced expansion of the fibril and the associated decrease in T_d. Interestingly, the change in T_d shows a biphasic behavior with respect to fibril porosity with the greatest amount of decrease occurring at an intermediate porosity level. This is explained by the diminishing effect of confinement on thermal stability as intermolecular distances increase.

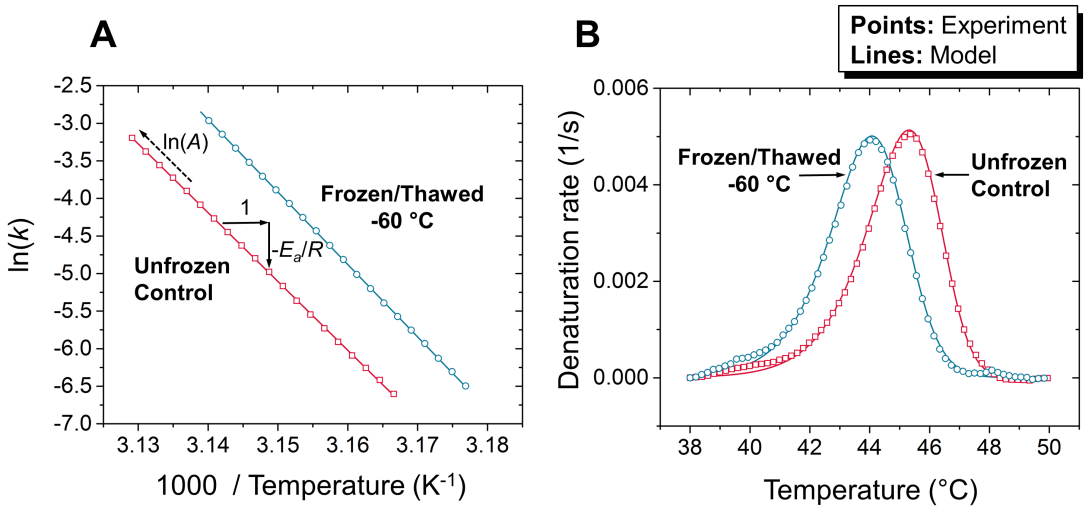

Figure 2.6. (A) Estimation of kinetic model parameters from experiments. (B) Comparison of simulated and experimentally obtained denaturation peaks. Experimental data is rarefied for illustration. Each point in trends corresponds to 100 data points.

Table 2.2. Estimated kinetic model parameters.

Sample	Treatment	lnA (A in 1/s)	E_a (kJ/mol)	n	R^2
Hydrogel	F/T -60 °C	307 ± 10	821 ± 25	1.55 ± 0.14	> 0.996
	UF Control	262 ± 19	705 ± 49	1.10 ± 0.07	> 0.997
Molecular Solution	F/T -60 °C	446 ± 24	1167 ± 62	1.26 ± 0.04	> 0.994
	UF Control	445 ± 18	1164 ± 51	1.11 ± 0.14	> 0.978

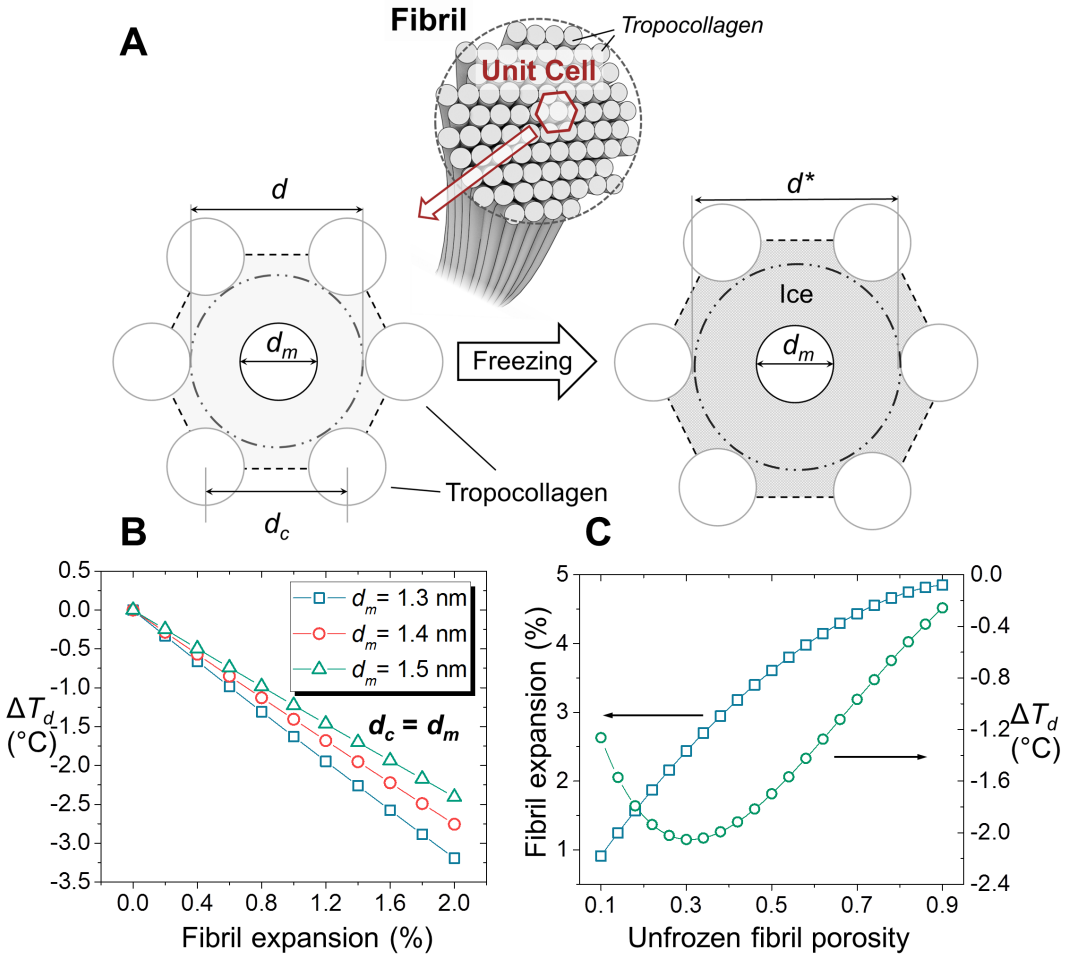

Figure 2.7. (A) Hexagonal unit cell of a fibril as it expands upon freezing. dm is tropocollagen nominal diameter, d is confinement diameter, dc: side of the unit cell. (B) The change in denaturation temperature upon hypothetical expansion of a tightly packed fibril (minimum porosity). (C) The amount of freezing-induced fibril expansion and change in denaturation temperature as a function of unfrozen fibril porosity.

2.3.7 Implications to Cold Denaturation of Collagen upon F/T

There has been a great concern in especially cell and tissue preservation community regarding low temperature stability of proteins [28, 29]. In this study we didnt encounter any lasting effect of F/T on stability of molecular collagen. Irreversible denaturation of collagen during F/T under the studied conditions is unlikely since denaturation enthalpies were considerably close between F/T and UF treatments. Since such a transition would be associated with a decrease in the number of native molecules available for denaturation during post-thaw experiments, one would expect the denaturation enthalpy of F/T to be lower than that of UF. While irreversible denaturation of cellular proteins was reported at low temperature storage conditions [37], cold denaturation in respect to unfolding of protein due to purely thermodynamic effects of temperature is commonly regarded as a reversible process [73]. Due to the post facto nature of post-thaw measurements, our results does not explain whether collagen has undergone such a transition during F/T and reverted back to its original state after F/T.

2.3.8 Collagen Thermal Denaturation Reaction and Calculated Metrics

The endothermic peak of collagen thermal denaturation showed up in the non-reversing specific heat signal identifying the reaction as being irreversible at least within the time frame of modulation period. This observation is in agreement with the kinetic model in our study that assumes a single-step irreversible process [53] More recently collagen denaturation is identified as a multi-step process that can also be approximated by a single-step irreversible process for slow heating rates such as the one used in the current study [74]. The reaction order estimated for unfrozen and frozen-thawed treatments was significantly different and exhibited itself as a widening

of endothermic peak. This curious effect points to the existence of new unknown intermediate denaturation processes in the case freeze/thaw and needs to be further investigated.

It is important to note that measurements of ΔH_d had significant variability. This is expected since collagen hydrogel specimens in this study contained only a small amount of collagen, particularly less than 0.6% w/w which is considerably less than native tissue specimens such as rat tail used in other studies [53]. This, combined with small sample preparation necessary for DSC could result in significant variations in relative collagen content in each sample. Denaturation temperature on the other hand is an intrinsically intensive property that does not depend on the mass of collagen. Therefore it can be determined with high precision. The measurements of temperature metrics were indeed highly reproducible as indicated by small standard deviations (less than 0.8 °C). We focused our discussion in this study on these precise temperature metrics.

3. THE ROLE OF CELLULAR WATER TRANSPORT IN FREEZING-INDUCED CELL AND TISSUE DEFORMATION

3.1 Introduction

When cell is frozen in suspension, ice first forms in extracellular space. As ice grows by decreasing temperature, extracellular solution becomes more concentrated by exclusion of solutes at phase change interface. Then, cell loses part of its water by transport across the membrane due to osmotic pressure difference with its surroundings [43]. This cellular water transport (CWT) process plays a key role in freezing outcome since the amount of water remaining in the cell during freezing is connected to multiple cryoinjury mechanisms [7, 75]. It is therefore necessary to accurately determine the rate and extent of CWT to be able to optimize freezing procedures.

Since the pioneering work of Mazur [20], CWT in context of freezing has been investigated extensively, mainly based on the perception that cell is a membrane bound, fluid filled domain and cell membrane is the only significant transport barrier during freezing. This approach has resulted in reasonably good measures for cryopreservation of cells in suspension, enabling formation of cell banks for many cell lines [76]. However, the concept of CWT as a mere membrane transport process does not explain the large cell-to-cell variations in transport parameters for cells from the same population as well as the effects of cell attachment state on water transport [44, 77, 78]. Moreover, recent studies show that distribution of intracellular water becomes spatially heterogeneous during freezing [79] and that modifications in the cytoskeletal organization have been found to affect the cellular water transport properties [80]. In addition, studies indicate that osmotically dehydrated cells become mechanically stiffer [81]. It is possible that

deformation of intracellular structures that result in mechanical property changes may also interfere with intracellular fluid transport. However, whether and how intracellular structures can act on osmotically-driven CWT during freezing still needs to be identified.

In the first part of this study, we address the above problem by considering cytoplasm as a porous solid structure and investigate its potential to hinder osmotically driven water transport during freezing. Unlike the previous models of CWT, it is hypothesized that cytoplasm introduces an intracellular component for resistance to flow as well as to deformation. This is illustrated in Figure 3.1. As the cell dehydrates, the porous cytoplasm collapses resulting in even higher resistance to water transport at highly deformed regions. As the dehydration continues some parts of the cytoplasm may fully collapse and result in a locking effect i.e. trapping the water in the cell. In addition, the deformation may also result in a decline in the interstitial fluid pressure which may create a suction pressure at the inner side of the cell membrane and counteract the osmotic pressure driven outflow of water. The hypothesis was tested by simulations of CWT based on poroelastic theory [47, 48] combined with experiments that involve measurement of intracellular deformation in suspended cells during freezing. Results indicate to significant heterogeneity in intracellular deformation that can interfere with CWT under certain conditions and propose hydraulic conductivity of the cytoplasm as the key transport property that governs the intracellular fluid transport.

In the second part of this study, implications of freezing-induced CWT at tissue scale is considered. Cellular water can contribute to freezing induced deformation of tissues and can be a determining factor on the post-thaw tissue fate. When native or engineered tissues are frozen inside a controlled rate freezer, temperature gradients are developed within the tissue. As the freeze front propagates from its outer to

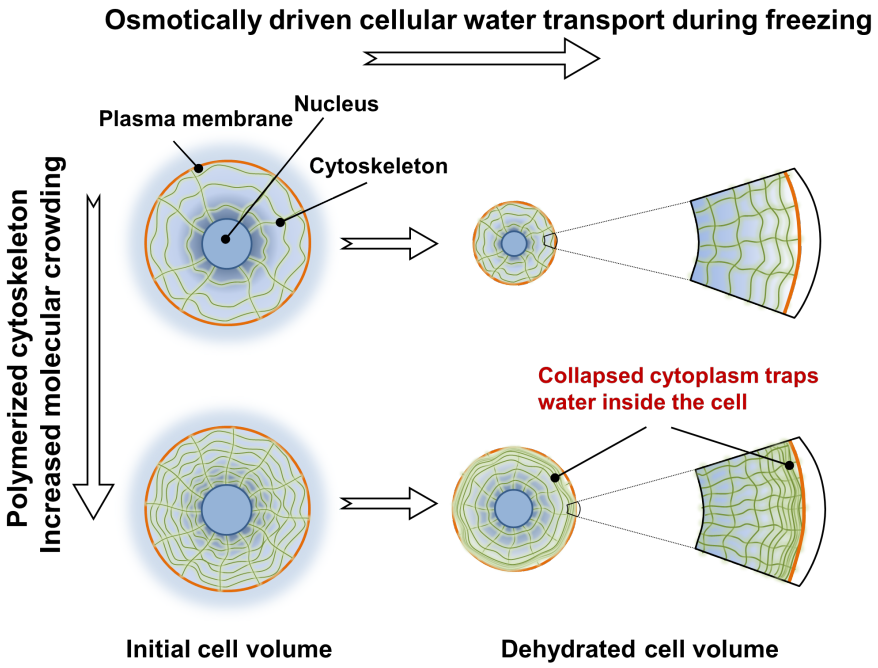

Figure 3.1. Cytoskeletal matrix introduces an intracellular component of resistance to flow.

inner layers tissue locally expands due to freezing of interstitial fluid and at the same time interstitial fluid is redistributed due to pressure gradients that arise from ice growth [19, 70]. This freezing-induced deformation of the tissue results in changes in its microstructure [19, 24, 69]. When cells are also present in the tissue, they interact with extracellular space and can affect the amount of freezing-induced deformation. By so-called freezing-induced cell-fluid-matrix interactions [69, 82], cells are thought to contribute to deformation by supplying excess water via osmotic pressure-driven cellular water transport. However whether CWT can be a significant factor on freezing-induced tissue deformation is not clear.

In order to address the above gap a semi-empirical model was developed. Representative elementary volume (REV) analysis was used to relate the freezing-induced expansion of the tissue to extracellular freezing kinetics and cellular water transport. For determination of the empirical parameters, first, freezing response of MCF-7 breast cancer cells was observed by cryomicroscopy, and the membrane permeability parameters were estimated with similar methods used in previous studies [24,78,83,84]. In addition, the latent heat release of the engineered tissue was measured by differential scanning calorimetry (DSC) to estimate the rate and extent of extracellular ice formation within the ET. Finally, the cellular water transport and extracellular ice formation data were combined to estimate the freezing-induced dilatation rate using the model. The results of the model are compared to a companion experimental study that provided tissue deformetry measurements under similar conditions to model simulations [50]. The model is also used to explore the effects of cellular water transport at cell concentrations corresponding to native tissues that were not possible to investigate experimentally.

3.2 Materials and Methods

3.2.1 Cell Culture and Reagents

A human breast carcinoma cell line (MCF7) was maintained in culture medium (DMEM/F12, Invitrogen, Grand Island, NY) with 5% fetal bovine serum, 2 mM L-glutamine, 100 μg/mL penicillin/streptomycin, and 10 μg/mL insulin. The MCF7 cells were cultured in 20 mL of supplemented culture medium in 75 cm^2 T-flasks at 37C and 5% CO2. Cells were collected by using 0.05% trypsin and 0.53 mM EDTA.

Early passage human foreskin fibroblasts, BR5 were provided by Dr. Frederick Grinnell (Department of Cell Biology, University of Texas Southwestern Medical Center) and maintained in culture medium DMEM/F12, (Invitrogen, Grand Island, NY) supplemented with 10% fetal bovine serum, 2 mM L-glutamine, and 100 μg/ml penicillin/ streptomycin. The fibroblasts were cultured up to the 20th passage in 75 cm^2 T-flasks at 37 °C and 5% CO2. The cells were consistently harvested at 80% confluency by using 0.05% trypsin and 0.53 mM EDTA.

For intracellular deformation analysis, up to 1×10^6 cells were replated in 100 mm cell culture plates and allowed to attach overnight. 500 nm fluorescent polystyrene nanoparticles (NPs) (G500, Thermo Fisher Scientific) coated with fibronectin (Invitrogen) were used as markers for intracellular deformation. NP internalization protocol was based on a previous study with the same cell line [85]. 6.08×10^9 NPs were mixed with 30 μg fibronectin in 500 μL culture medium and incubated at 37 °C for 10 minutes. After dilution in 4 mL culture medium, the NP suspension was placed on top of adherent cell monolayer and incubated at 37 °C for 2 hours. During that time, NPs attached to the cell membrane and internalized by cells through endocytosis. After 2 hours, the cell monolayer was washed with physiological phosphate buffered saline (1X PBS, Invitrogen) three times and incubated overnight to achieve distribution of

NPs throughout the cytoplasm. The cells were then retrieved as described before and suspended in culture medium with a concentration: 5×10^6 cells/mL. The cell suspension was kept in ice during the experiments. For estimation of membrane permeability parameters, cells were used as they are without NP internalization.

3.2.2 Measurement of Cellular Water Transport by Cryomicroscopy

For determination of membrane permeability parameters, MCF7 and BR5 were first prepared in suspension, dispensed in a quartz crucible and loaded on a temperature-controlled stage (MDS 600, Linkam). As cell suspension was frozen, images were acquired by a microscope (BX 51, Olympus) equipped with a CCD camera (Retiga 2000R, Qimaging). Cell concentrations in this study ranged from 2 × 105 to 1 × 106 cells/mL, such that cell-to-cell separation distances were large (cytocrit < 0.003), and cell concentration was not expected to have an effect on water transport [86]. In order to prevent substantial supercooling and spontaneous ice nucleation, the sample was initially cooled to -2 C, and ice was seeded by touching the edge of the sample with a liquid nitrogen-cooled needle. Afterwards, the temperature was increased by 0.9 to 1.2 °C and kept constant at just below the phase change temperature for 3 to 5 minutes to obtain small ice crystals in equilibrium with the extracellular medium. Then temperature was decreased at a controlled rate down to -40 °C. The cooling rates employed in this study were 5, 10 and 30 °C/min. For analysis, the projected cell area, A_p, was quantified at selected temperatures using image processing software (Fiji/ImageJ [87]). Then the cell volume, V, was estimated by assuming spherical geometry and using the relation:

$$V = \frac{4}{3}\sqrt{\frac{{A_p}^3}{\pi}} \tag{3.1}$$

For each cooling rate, 28 to 81 cells were analyzed. The osmotically inactive volume of the cell was estimated through an equilibrium freezing procedure in which the freezing was performed at a relatively slow cooling rate (2 °C/min, to -40 °C while the cells were allowed to reach osmotic equilibrium with their surroundings by holding the temperature at -5, -10, -15, -20 and -30 °C for 5 minute intervals.

In order to measure intracellular deformation during freezing, a slightly modified procedure as above was followed. BR5 in suspension were loaded and frozen in a PDMS microchannel (600 or 900 μm wide and 50 or 100 μm high) clamped on the temperature-controlled stage while simultaneous bright field and fluorescence (FITC, excitation / emission = 495 nm / 519 nm) images were acquired every 4 or 5 seconds. The end freezing temperature was -30 °C and the cooling rates considered were 5, and 30 °C/min.

3.2.3 Estimation of Membrane Permeability Parameters

The analysis of cellular water transport follows the previous studies e.g. [78, 84, 88], based on the membrane transport model of Mazur [20] with some modifications by Levin et al. [89]. Briefly, the rate of change of the cell volume is given by:

$$\frac{dV}{dt} = -J_w A = \frac{L_p A R T}{\nu_w} \left[\ln \left(\frac{(V - V_b)}{(V - V_b) + n_s \nu_s \nu_w} \right) - \frac{\Delta H_f}{R} \left(\frac{1}{T_{ref}} - \frac{1}{T} \right) \right] \tag{3.2}$$

where the cell membrane permeability to water, L_p, was assumed to depend on temperature only with its dependence modeled by Arrhenius Equation as follows:

$$L_p(T) = L_{pg} \exp \left[\frac{-E_{Lp}}{R} \left(\frac{1}{T} - \frac{1}{T_{ref}} \right) \right] \tag{3.3}$$

The membrane permeability parameters investigated in this study were L_{pg}, the membrane permeability at the reference temperature, and E_{Lp}, the activation energy

Table 3.1. Definitions and values of parameters used in cellular water transport study.

Symbol	Definition	Value(s)	Unit
R_o	Initial Cell Radius	8.6*	μm
ϕ_o	Initial porosity	0.69*	-
K_o	Initial hydraulic conductivity	1×10^{-13} 1×10^{-14} 1×10^{-15}	m^2/Pa·s
E	Elastic modulus of solid part	200**	Pa
V	Cell volume	Variable	μm^3
V_o	Initial cell volume	2978 ± 127*	μm^3
V_b	Osmotically inactive cell volume	$(0.31 \pm 0.02)\ V_o$*	μm^3
A	Cell surface area	Variable	μm^2
ν	Poisson's ratio for solid part	0.30**	-
J_w	Osmotic water efflux from cell	Variable	μm/s
T	Temperature	Variable	K
T_{ref}	Reference temperature	273.15	K
ΔH_f	Latent heat of fusion	33.5	kJ/kg
R_g	Universal gas constant	8.314	J/mol/K
B	Cooling rate	5	°C/min
ν_w	Partial molar volume of water	1.8×10^{13}	μm^3/mol
ν_s	Dissociation constant of salt	2	-
n_s	Number of moles of salt in the cell	3.031×10^{-13}	mol
L_p	Membrane permeability for water	Variable	μm^3/N/s
L_{pg}	Membrane permeability for water at T_{ref}	0.403*	μm^3/N/s
E_{Lp}	Activation energy for membrane water transport	175*	kJ/kg

* Value provided for MCF7.
** From [91].

for water transport across the membrane. The definitions of the other symbols used in Equations. (3.2) and (3.3) are provided in 3.1.

The membrane permeability parameters were estimated by fitting the model predictions to experimental data. A nonlinear least-squares curve fitting procedure was performed in MATLAB® using Levenberg-Marquardt algorithm [90].

3.2.4 Estimation of Intracellular Deformation

The time-lapse cryomicroscopy images were cropping into 256 × 256 pixel regions showing individual cells. Then the positions of selected NPs were tracked over up to 50 frames using TrackMate Jaqaman, 2008 in Fiji/ImageJ.

The deformation analysis was performed by assuming initially undeformed cell and a reference frame fixed to the microscope stage. Then the displacement of particle i was defined as $\vec{u}_i(t) = \vec{x}_i(t) - \vec{x}_{i,o}$ in terms of particle position at time t, $\vec{x}_i(t)$, and initial position, $\vec{x}_{i,o}$. The intracellular displacement field, $\vec{u}$, was approximated using a linear finite element method (FEM) interpolation scheme based on triangulation of the cellular domain with intracellular particles as nodes. This approximation was used to calculate the displacement and deformation gradient tensors, $\nabla\vec{u}$ and $\mathbf{F} = \mathbf{I} + \nabla\vec{u}$, $\mathbf{I}$ being the identity tensor. Then the Cauchy finite strain tensor was calculated by,

$$\mathbf{C} = \mathbf{F}^T\mathbf{F} \tag{3.4}$$

Areal strain, E_A that provides the relative change in the area of a finite element was selected as a two-dimensional direction-independent measure of intracellular deformation. E_A is given by,

$$E_A = \sqrt{\det(\mathbf{C})} - 1 \tag{3.5}$$

One should note that, due to 1st order differentiability of the FEM interpolation, The resulting E_A field was constant across each triangular element.

In order to distinguish the variation of intracellular deformation at different regions of the cell, the intracellular space was divided into three deformation zones with varying distance from cell centroid as shown in the top left inset in Figure 3.6. All zones are equal in area with zone 1 and zone 3 being closest to the cell centroid and

cell membrane respectively. Then the elements of triangular grid were grouped into zones based on the positions of their centroids and a mean value for E_A over each zone was calculated by,

$$\bar{E}_A = \frac{\iint\limits_A E_A \, dA}{A} \tag{3.6}$$

Where A is the total area of elements included in that zone.

3.2.5 Poroelastic Model of Cytoplasm for Prediction of Intracellular Deformation by CWT

A poroelastic formulation of cytoplasm is developed by considering it as a two-phase system that is composed of a fibrous cytoskeletal matrix as the solid phase (denoted by subscript, s) which is saturated with the cytosol that is considered as the fluid phase (denoted by subscript f). The space occupied by the solutes and organelles is neglected in this analysis. Therefore the volume fractions of solid and fluid phases, ϕ_s and ϕ_f, satisfy the following relationship:

$$\phi_f + \phi_s = 1 \tag{3.7}$$

The mass and momentum conservation laws can be summarized as follows:

Mass conservation of fluid phase:

$$\frac{\partial}{\partial t}\left(\phi_f \rho_f\right) + \nabla \cdot \left(\phi_f \rho_f \vec{v}_f\right) = \rho_f \left(q_B - q_L\right) \tag{3.8}$$

where ρ_f is the density of the fluid phase, and $\vec{v}_f$ is the intracellular fluid velocity while the right hand side of Equation (3.8) represents the contribution from volumetric source and sink. In the remaining part of this section, we assume no injection or drainage occurs in the cell such that $q_B = q_L = 0$.

Similarly, the mass conservation of solid phase follows as:

$$\frac{\partial}{\partial t}\left(\phi_s \rho_s\right) + \nabla \cdot \left(\phi_s \rho_s \frac{\partial \vec{u}}{\partial t}\right) = 0 \tag{3.9}$$

where ρ_s is the density of the solid phase, and $\vec{u}$ is the displacement of solid phase with respect to an initial state, which can be arbitrary without loss of generality.

The momentum conservation of fluid phase is governed by the Darcys Law:

$$\phi_f \left(\vec{v}_f - \frac{\partial \vec{u}}{\partial t}\right) = -K_{hyd} \nabla p \tag{3.10}$$

where K_{hyd} is the hydraulic conductivity of the cytoplasm and p is the intracellular fluid pressure.

Finally, under the assumption that the cytoskeleton remains in a quasi-static state through the cellular dehydration, the momentum conservation of solid phase is expressed by the stress equilibrium:

$$\vec{\nabla} \cdot \sigma = \mu_s \nabla^2 \vec{u} + \lambda_s \nabla e - \nabla p = \vec{0} \tag{3.11}$$

Here, σ is the Cauchy stress tensor, μ_s and λ_s are the first and second Lame's constants and e is the dilatation (or volumetric strain) of the cytoskeleton. In obtaining Equation (3.11), the solid matrix is assumed to be a linear elastic material. Note that dilatation approximates the areal strain introduced in Equation (3.5) and $e = E_a$ for infinitesimally small deformations.

Under the assumption that both phases are incompressible, the mass conservation Equations, (3.8) and (3.9), can be combined together to arrive at:

$$\nabla \cdot \left(\phi_f \vec{v}_f + \phi_s \frac{\partial \vec{u}}{\partial t}\right) = 0 \tag{3.12}$$

By rearranging the terms and substituting Equation (3.10) in above, one obtains:

$$\frac{\partial e}{\partial t} = K\nabla^2 p + \nabla K \cdot \nabla p \tag{3.13}$$

Furthermore, the divergence of stress equilibrium, $\nabla\cdot$(3.11) also yields a relationship between the dilatation and intracellular fluid pressure only:

$$\nabla^2 \left(p - \mu^* e\right) = 0 \tag{3.14}$$

where the parameter $\mu^* = 2\mu_s + \lambda_s$ is the aggregate modulus. In Equation (3.14) the mechanical properties of the solid matrix are assumed to be uniform across the cell.

Equations (3.13) and (3.14) together represent a dilatation-pressure formulation where e and p are the dependent variables. For the special case of constant hydraulic conductivity, the second term in the right hand side of Equation (3.13) drops and the two equations can be combined into the well-known Consolidation Equation introduced by Biot [47],

$$\frac{\partial e}{\partial t} = D\,\nabla^2 e \tag{3.15}$$

where $D = K_{hyd}/\mu^* = K_{hyd}/\left(2\mu_s + \lambda_s\right)$ is the coefficient of consolidation. However, in our case, the deformation of cytoplasm is large and the variations in the hydraulic conductivity cannot be neglected. Therefore, we cannot use the Consolidation Equation directly.

Now restricting the attention to the case of spherical geometry with radial symmetry, Equation (3.13) is solved for intracellular fluid pressure:

$$p = \mu^* e + p_o \tag{3.16}$$

where p_o is the pressure near the cell membrane.

Substituting Equation (3.16) in Equation (3.13), the dilatation formulation for the cytoplasm is obtained:

$$\frac{\partial e}{\partial t} = D\frac{1}{r^2}\frac{\partial}{\partial r}\left(r^2\frac{\partial e}{\partial r}\right) + \mu^*\frac{\partial K}{\partial r}\frac{\partial e}{\partial r} \tag{3.17}$$

Equation (3.17) is an extended form of Consolidation Equation that accounts for the spatial variations in the hydraulic conductivity. However, it is important to remember that this equation is only valid for the spherical geometry with radial symmetry, which is the case considered in our study.

In order to investigate the freezing-induced deformation of cytoplasm, we consider Equation (3.17) together with appropriate initial and boundary conditions. Figure 3.2A illustrates the main features of the problem setup. For a spherical cell with a radius: $R = R(t)$, which is initially undeformed, the initial condition is:

$$e = 0 \text{ for all } r \in (0, R(t)) \text{ and } t = 0 \tag{3.18}$$

For the boundary condition at the cell membrane ($r = R(t)$) osmotically driven water efflux, J_w from membrane transport model in Equation (3.2) is related to dilatation by considering the Darcys Law together with Equation (3.16) to obtain:

$$\left.\frac{\partial e}{\partial r}\right|_{(R(t),t)} = -\frac{J_w}{D} \tag{3.19}$$

(3.18) And finally, radial symmetry at cell center implies:

$$\left.\frac{\partial e}{\partial r}\right|_{(0,t)} = 0 \tag{3.20}$$

(3.19) The variations in hydraulic conductivity due to deformation of cytoplasm is related to dilatation based on the work of Kim et al. [92]:

$$K = K_o \left[\left(\frac{1}{\phi_o} \right) (1+e)^{2/3} - \left(\frac{1-\phi_o}{\phi_o} \right) (1+e)^{-1/3} \right]^3 \tag{3.21}$$

where K_o and ϕ_o are the initial (undeformed) hydraulic conductivity and porosity respectively.

Note that, the governing Equation (3.17) is a nonlinear partial differential equation that is difficult to solve analytically. Therefore a numerical solution procedure is followed. Furthermore, the problem is a moving boundary problem since the cell radius decreases by time due to dehydration. This also complicates the numerical solution procedure. Therefore the moving boundary is eliminated by using a transformation for both the r-coordinate and dilatation as follows:

$$\hat{r} = \frac{r}{R(t)} \text{ and } \hat{e} = R(t) \cdot e \tag{3.22}$$

(3.21) where the quantities indicated by '$\hat{\cdot}$' are the new variables. Solution domain that is obtained by the transformation is shown in Figure 3.2B. Applying the transformation to the governing equation as well as the initial and boundary conditions, the governing equation becomes

$$\frac{\partial \hat{e}}{\partial t} = \frac{D}{R^2} \hat{r}^2 \frac{\partial}{\partial \hat{r}} \left(\hat{r}^2 \frac{\partial \hat{e}}{\partial \hat{r}} \right) + \frac{D}{R^2 K} \frac{\partial K}{\partial \hat{r}} \frac{\partial \hat{e}}{\partial \hat{r}} - \frac{1}{R} J_w \hat{e} \tag{3.23}$$

With initial and boundary conditions:

$$\begin{aligned} &\hat{e} = 0 \text{ for all } \hat{r} \in (0,1) \text{ and } t = 0 \\ &\left. \frac{\partial \hat{e}}{\partial \hat{r}} \right|_{(0,t)} = 0 \text{ and } \left. \frac{\partial \hat{e}}{\partial \hat{r}} \right|_{(1,t)} = -\frac{J_w R^2}{D} \end{aligned} \tag{3.24}$$

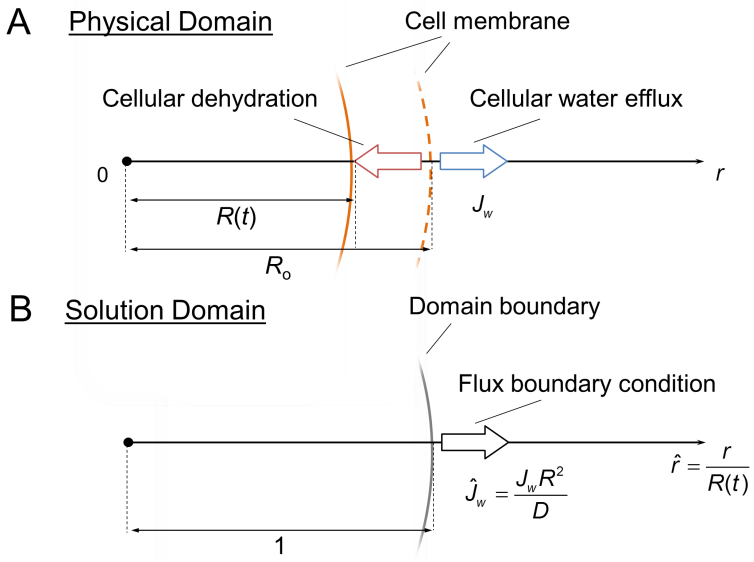

Figure 3.2. Problem setup and transformation of the problem from physical domain to solution domain.

And the moving boundary condition that comes from the mass conservation:

$$\frac{dR}{dt} = -J_w \tag{3.25}$$

The problem was solved by an in-house finite difference code developed in MATLAB®.

3.2.6 Measurement of Latent Heat Release by Differential Scanning Calorimetry

The rate of latent heat release by an engineered tissue was determined as a function of temperature using a differential scanning calorimeter (DSC) (DSC Q200, TA Instruments). Engineered tissues were prepared as described before. Then, gel sections with a diameter of approximately 2 mm were extracted by a biopsy punch and transferred to DSC pans. The sample pans were sealed hermetically to avoid any leakage of volatile components. The resulting sample masses were 5-6 mg. The

sample was initially cooled to -30 °C to nucleate and warmed close to the phase change temperature. Then, the sample was thermally equilibrated to have only a small amount of ice crystals. This step ensured the presence of ice growth sites in the sample prior to freezing and prevented the spontaneous ice nucleation that would otherwise invalidate the measurements. The sample was then slowly cooled to -30 °C with a cooling rate of 1 °C/min, which was considered to be slow enough to avoid supercooling and approximate thermodynamic equilibrium conditions. The rate of latent heat release was recorded as ice formed gradually in the sample. Three repetitions were performed. To account for sensible heat effects and equipment flaws, a linear baseline was constructed using the data points at temperatures: -20 and -25 °C, and extrapolated to the temperature range of interest. The rate of latent heat release was obtained by subtracting the baseline from the overall DSC signal.

3.2.7 Determination of the Rate and Extent of Extracellular Freezing

In order to quantify the extent of extracellular ice formation, the frozen fraction, F, was defined as the ratio of the volume of extracellular fluid that has formed ice to the total volume of the extracellular fluid:

$$F = \frac{\text{Volume of interstitial fluid frozen}}{\text{Total volume of interstitial fluid}} \tag{3.26}$$

For slow cooling rates, the freezing proceeds close to thermodynamic equilibrium and both the rate of latent heat release and the frozen fraction can be considered as functions of temperature only, i.e. $q = q(T)$, and $F = F(T)$, respectively. Then the temperature rate of change of the frozen fraction is related to the latent heat release as follows:

$$\frac{dF}{dT} = -\frac{1}{B}\frac{q}{Q_{total}} \text{ where } B = -\left(\frac{dT}{dt}\right)_{DSC} \tag{3.27}$$

Here, q is the time rate of latent heat release measured by the DSC, and Q_{total} is the total amount of latent heat release calculated by integrating with respect to time. B is the cooling rate imposed by the DSC on the sample. F was obtained by integrating eqn. (5) with respect to temperature accordingly. Note that the analysis was performed by normalizing the DSC measurements with the value of latent heat of fusion (276.4 $\pm$ 1.4 kJ/kg) so that the results are independent of the value of latent heat.

3.2.8 REV Analysis of Freezing-induced Tissue Deformation in the Presence of CWT

This section presents a representative elementary volume (REV) analysis to describe the freezing- induced dilatation as a function of extracellular ice formation and cellular dehydration dynamics. Figure 3.3 shows a schematic of REV, that provides a volume averaged representations of different ET compartments. States (I) and (II) correspond to times before and during extracellular freezing, respectively. The ET is composed of cellular and extracellular compartments, as indicated by subscripts (c) and (ec) in Figure 3.3. Each compartment is associated with a solid (s) part that corresponds to intracellular solutes, structures and organelles in the cell and extracellular solutes and collagen fibrous network in the extracellular space. Each compartment also has a fluid (fl) part standing for the intracellular and interstitial water surrounding the solid parts. The engineered tissue is assumed to be fully saturated with the interstitial fluid. As ice forms in the extracellular space, cells dehydrate and make more water available for extracellular freezing. Meanwhile, the extracellular space expands increasing the volume of the REV. In this analysis the possibility of intracellular ice formation are not taken into account and cells contribute to freezing induced expansion by CWT only. Furthermore, the REV is assumed to be a material volume such that no mass flux occurs through its boundaries. Thus, the deformation is caused by

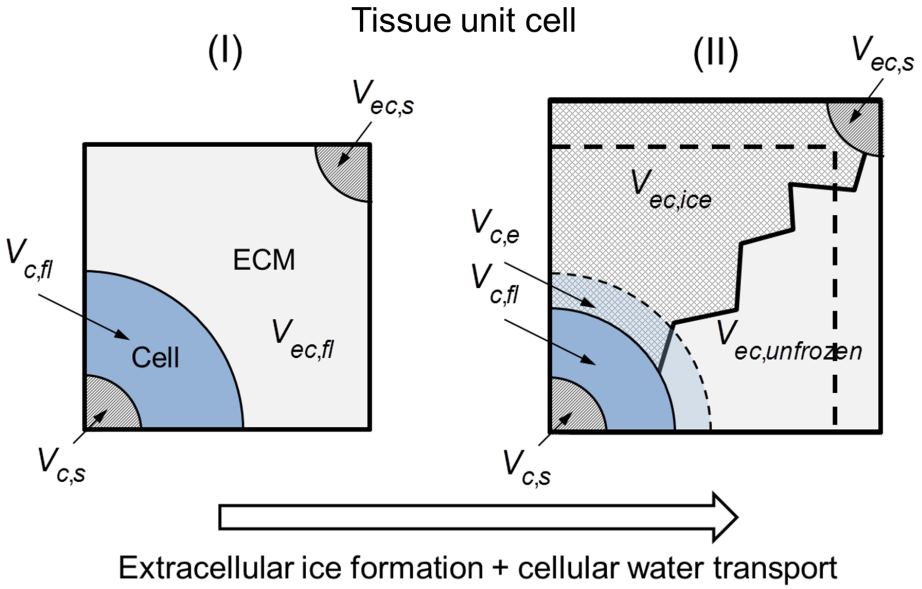

Figure 3.3. Schematic illustration of the representative elementary volume (REV) of an engineered tissue (ET). States (I) and (II) correspond to before and during extracellular freezing. The ET is composed of cellular (c) and extracellular (ec) compartments. Each compartment has both solid (s) and fluid (fl) components. As ice forms in the extracellular space, cells dehydrate and make more water available for extracellular freezing. In the meantime the extracellular space expands increasing the volume of the REV.

thermodynamic expansion only, and the redistribution of interstitial fluid due to interstitial pressure gradients across the ET are also not taken into account. Those assumptions are in accordance with the main purpose of this model, which is to study the significance of cellular water transport rather than simulating the complete spatiotemporal deformation of the ET.

The frozen fraction can also be expressed in terms of the variables in Figure 3.3 as follows:

$$F = \frac{V_{ec,frozen}}{V_{ec,fl}} = \frac{\rho_{ice}}{\rho_{fl}} \frac{V_{ec,ice}}{V_{ec,fl}} \tag{3.28}$$

where $V_{ec,frozen}$ is the volume of interstitial fluid that undergoes freezing, $V_{ec,ice}$ is the volume of ice that forms during this process and, ρ_{ice} and ρ_{fl} stand for the densities of ice and interstitial fluid (water), respectively. Furthermore, some portion of the cellular water becomes available for freezing as it is excluded to the extracellular space by CWT. The volume of this excess water is represented by $V_{c,e}$ in Figure 3.3.

Using Equation (3.28), the volume of the REV at an arbitrary time during freezing can be written in terms of the initial (unfrozen) volume, frozen fraction and excess water as follows:

$$V_{REV} = {V_{REV}}^I + F(t)R\left({V_{ec,fl}}^I + V_{c,e}(t)\right) \tag{3.29}$$

where $R = \rho_{fl}/\rho_{ice} - 1$ is the relative density difference between the fluid and ice. Here it was assumed that the volumes of the solid parts remain the same during freezing. The superscript (II) over V_{REV} was dropped for brevity. Thus, the rate of freezing-induced dilatation in the ET can be determined as follows:

$$\dot{e} = \frac{1}{V_{REV}} \frac{dV_{REV}}{dt} = \frac{R\left(\phi + CV_e\right)}{1 + R\left(\phi + CV_e\right)F} \frac{\partial F}{\partial t} + \frac{RFC}{1 + R\left(\phi + CV_e\right)F} \frac{\partial V_e}{\partial t} \tag{3.30}$$

where $\phi = \left(\frac{V_{ec,fl}}{V_{REV}}\right)^I$ is the initial (unfrozen) porosity, C is the initial cell concentration and V_e is the amount of water excluded per cell. Note that $\dot{e}$ describes the rate of areal

deformation in the tissue and is selected as the measure of freezing damage rather than dilatation itself for comparison with previous studies [24, 50, 69]. This is different than the case of intracellular deformation where dilatation is used as the measure of deformation.

In summary, $\dot{e}$ is expressed by Equation (3.30) as a function of the tissue properties: initial porosity, and cell concentration; as well as the freezing conditions: frozen fraction, the rate of ice formation, the amount of water excluded to the extracellular space from cells and the rate of this water exclusion.

In order to quantify the contribution of CWT in freezing-induced tissue defromation, relative dilatation rate was defined as:

$$\Delta\dot{e} = \frac{\dot{e}_{\mathrm{CWT}} - \dot{e}_{\mathrm{No\ CWT}}}{\max(\dot{e}_{\mathrm{CWT}})} \tag{3.31}$$

where the subscripts $\dot{e}_{\mathrm{CWT}}$ and $\dot{e}_{\mathrm{No\ CWT}}$ stand for the dilatation rates that occurred in the presence and absence of CWT, respectively.

3.3 Results and Discussion

3.3.1 CWT by Cryomicroscopy

Cellular dehydration caused by freezing-induced water transport is presented in Figure 3.4. Representative cryomicroscopy images of MCF7 are shown in Figure 3.4A. Cells are initially at osmotic equilibrium with the extracellular solution which contains only a few small round ice crystals. As the sample is cooled, the ice crystals rapidly grow and the cells dehydrate significantly to reestablish osmotic equilibrium. The dehydration continues but at a slower pace as the sample is cooled further to -40 °C. Predictions and measurements of the change of cell volume with respect to the isotonic volume with decreasing temperature are shown in Figure 3.4B. Both MCF7 and BR5

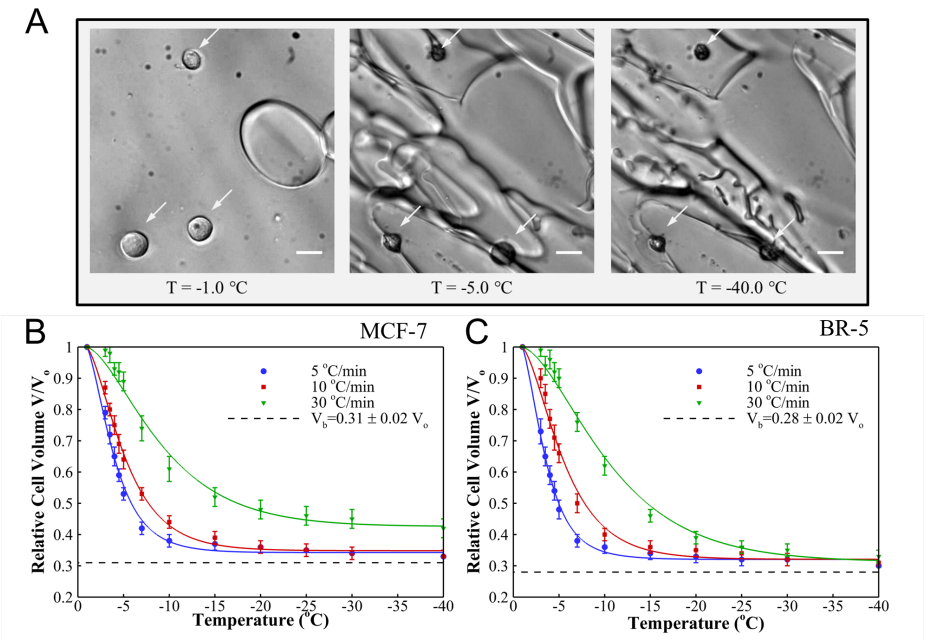

Figure 3.4. Cellular water transport observed by cryomicroscopy. (A) Micrographs showing dehydration of MCF-7 cells (marked by arrows) in the presence of ice as temperature is decreased to -40 °C by 10 °C/min. Cell volume change with respect to temperature are shown for cases of (B) MCF-7 and (C) BR-5 for three different cooling rates. Points indicate experimental data in terms of mean ± standard deviation. Solid lines are best fits of membrane transport model. V_b is osmotically inactive volume fraction obtained by equilibrium freezing.

dehydrate significantly for slow cooling rates: 5 and 10 °C/min and attains a volume close to the osmotically inactive cell volume, V_b determined by equilibrium cooling experiments. Th values of V_b are similar to ones reported for other cell lines [78, 93]. For the 30 °C/min cooling rate with MCF-7, about 10% of the freezable water was trapped in the cell. However, However all freezeable water was excluded in BR5, but in a delayed manner. The differences in the end volumes observed for different cooling rates suggest that the resistance to CWT, which can be considered to originate from the plasma membrane as well as the cytoplasm, depends on temperature and/or the cooling rate. Similar results were obtained in previous studies [78, 94].

3.3.2 Heterogeneity of Intracellular Deformation During CWT

In side experiments we used fluorescence particle tracking cryomicroscopy to measure intracellular deformation during CWT. measured. Figure 3.5 provides and example of time-lapse cryomicroscopy images and distribution of intracellular deformation for a cooling rate of 5 °C/min. Bright field images on the left panel show a marked decrease in cell projected area with increasing time. Trajectories of selected particles are superimposed on the fluorescence images (center panel). It can be seen that the cell of interest has undergone considerable amount of translation and rigid body rotation during freezing; however, contributions from rigid body motion were canceled out during the deformation analysis outlined in Section 3.2.4. Images in the right panel show the areal strain contours estimated from particle trajectories and deformation analysis. The negative sign and decreasing trends of the E_a are in accordance with the dehydration of cytoplasm during freezing. While the spatial resolution of the measurements is limited by the size of the coarse interpolation grid, some variations in dilatation across the cell can be observed. In order to quantify the variation of deformation in intracellular space, cell was divided into zones based on distance to cell centroid.

Figure 3.6 illustrates the grouping of the elements of computational grid into the three zones and the time variation of mean areal strain ($\bar{E}_a$) associated with each zone for three cases. Case (A) and (B) correspond to cells frozen with a rate of 5 °C/min and (C) is a case with 30 °C/min. It is observed that, for case (A), dilatation is generally lowest in the zone 3 which involves the regions closest to the cell membrane indicating that the greatest amount of deformation occurs here. Zone 1, on the other hand, remains at relatively undeformed state, with significantly higher values of dilatation during the first 150 seconds of freezing. The deformation of zone 2 stays in between the two throughout the process. Interestingly in (A) there is a recovery towards

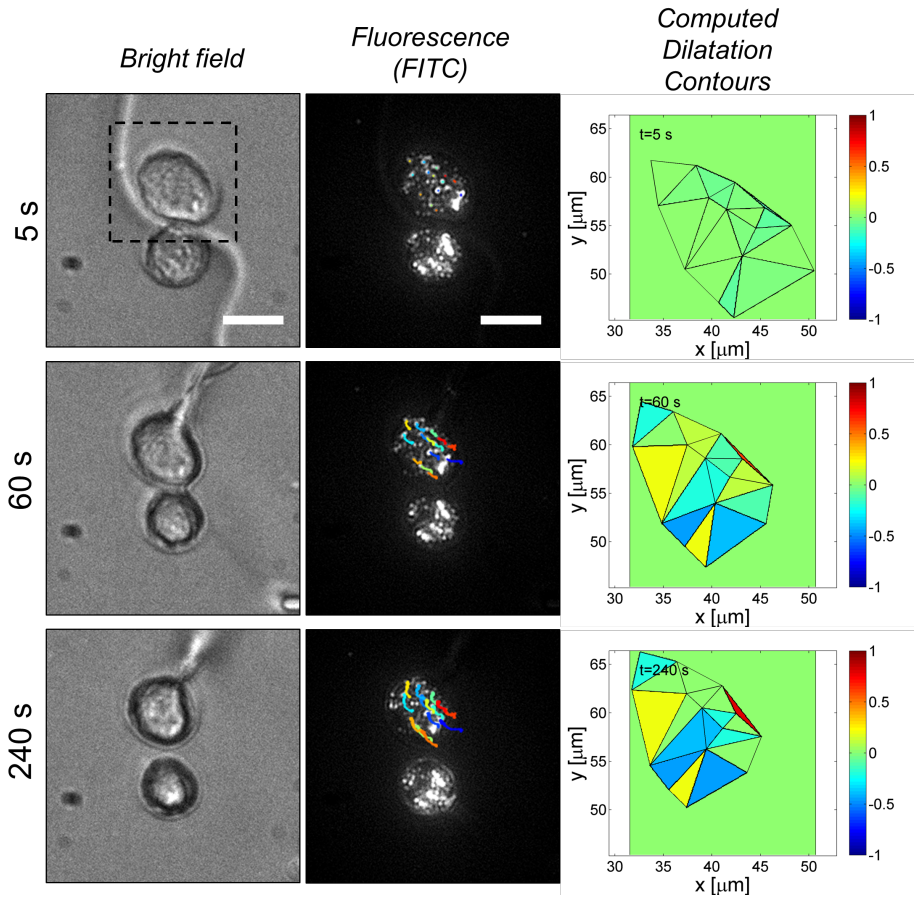

Figure 3.5. Measurement of intracellular deformation by fluorescence particle tracking cryomicroscopy. Displacement of cell boundary was manually traced from bright field images (left panel). Displacement of intracellular markers, indicated by colored lines, were determined by single particle tracking (middle panel). Deformation was obtained by differentiation of displacement field based on finite element approximation of discrete marker trajectories and reported in terms of areal strain (right panel).

the undeformed state after 100 s. In cases (B) and (C), the greatest deformation is again observed for zone 3. In contrast to case (A), both show a relatively uniform deformation with monotonic decrease of dilatation i.e. no recovery. Altogether, these results provide evidence that the deformation of cytoplasm during freezing can be heterogeneous, with regions near the membrane showing the greatest deformation. The spatial heterogeneity and temporal trends of regional dehydration varies from cell to cell in the same population and across cooling rates.

3.3.3 Predictions of CWT Computational Model with Poroelastic Cytoplasm

The model predictions for the spatiotemporal variation of E_a are presented in Figure 3.7. As hydraulic conductivity, K_{hyd}, is one of the key parameters in quantifying the resistance to flow in a porous medium, the main focus was on the effect of K_{hyd} in intracellular deformation. Typical values for K_{hyd} are reported to be between 7.5×10^{-14} and 2.2×10^{-15} m^2/Pa/s for human melanoma cells [91]. Therefore, the simulations were conducted over a physiologically relevant regime where undeformed hydraulic conductivity, $K_{hyd,o}$ was varied between 1.0×10^{-13} and 1.0×10^{-15}. It can be seen that for the case where $K_{hyd,o}$ is the highest ($K_{hyd,o} = 1.0 \times 10^{-13}$), the distribution of the intracellular water and therefore the deformation across the cell is uniform (Figure 3.7A). In this case, the flow resistance of cytoskeletal matrix can be considered negligible. However as the hydraulic conductivity is decreased by a factor of 10 and 100, the deformation of cytoplasm becomes increasingly non-uniform (Figures 3.7B and 3.7C) where the highest deformation occurs in the vicinity of the cell membrane and the center of the cell remains relatively undeformed. By comparing the initial porosity with the magnitude of dilatation, it can be seen that, for the case of $K_{hyd,o} = 1.0 \times 10^{-15}$ m^2/Pa/s, about 65% of cytosol is drained from the matrix near the cell membrane. The center of the cell on the other hand has lost less than

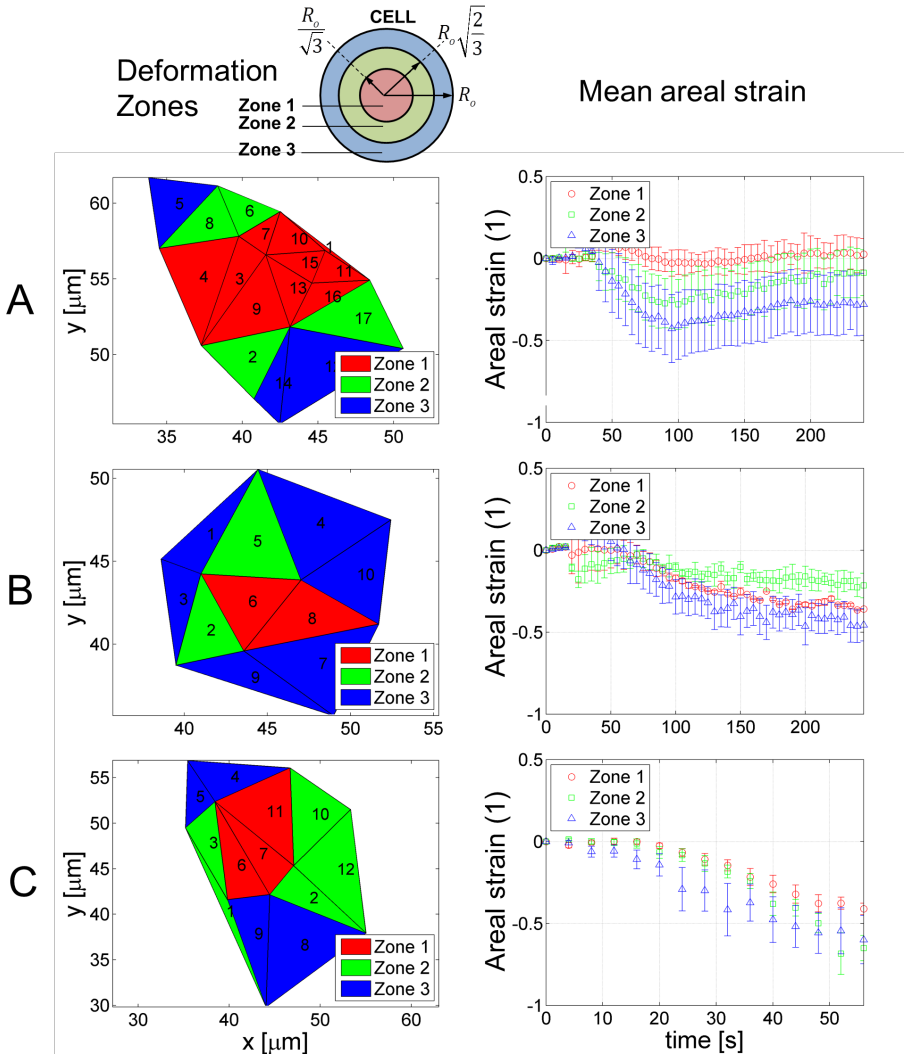

Figure 3.6. Heterogeneity of intracellular deformation during freezing. Finite elements are grouped into three different deformation zones based on their distances to cell centroid at $t = 0$. (left panel). Variation of mean areal strain with time for each deformation zone (right panel). Cases A and B are for a cooling rate of 5 °C/min. Case C is for 30 °C/min. Error bars indicate the standard deviation.

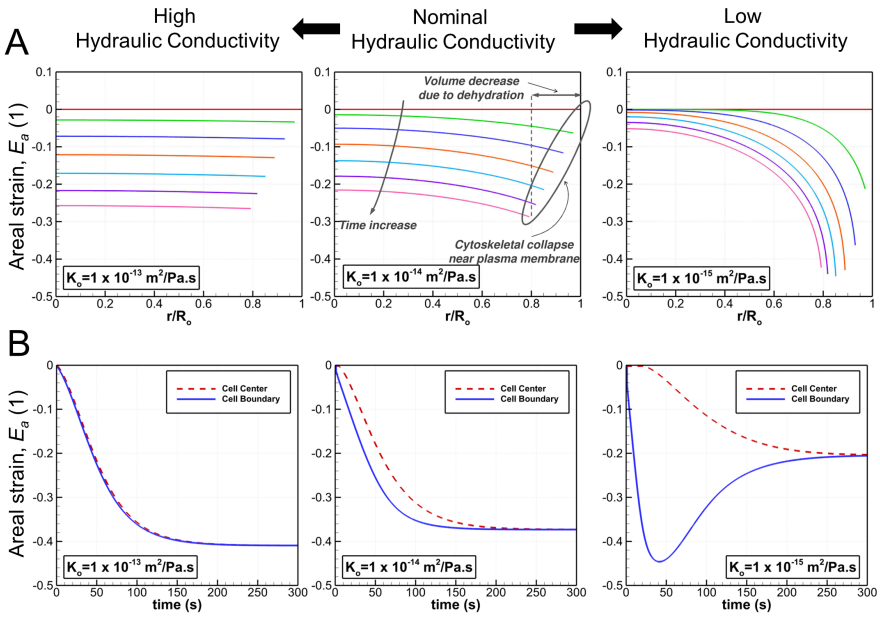

Figure 3.7. Predictions of intracellular areal strain, E_a, by CWT computational model for varying levels of hydraulic conductivity. Top panel shows the variation of E_a with normalized distance from cell center. The time interval between each line trend is 20 seconds. The bottom panel shows the variation of E_a at cell center vs. cell boundary with time.

10% of its cytosol. In essence, the deformation of cytoplasm shows a varying degree of heterogeneity for different hydraulic conductivities. This is an observation in agreement with the intracellular deformation measurements. In particular, the model predictions for low hydraulic conductivity compare well with case (A) in Figure 3.6 where the cell undergoes highly non-uniform deformation and a similar recovery process near the cell membrane. The responses observed in case (B) and (C) might correspond to cells with higher hydraulic conductivities as both show relatively uniform deformation without any recovery phase. Overall, these results suggest that hydraulic conductivity might be a significant factor in affecting the intracellular deformation patterns that occur during freezing. In above results the intracellular deformation, despite being highly heterogeneous, typically does not have a significant effect on the amount of water

transport from the cell during freezing. However for lower hydraulic conductivities, the deformation near the cell membrane is likely to become even more pronounced. The simulations conducted with hydraulic conductivities less than 1×10^{-15} $m^2/Pa/s$, would stop prematurely when the magnitude of the dilatation approached the initial porosity indicating complete collapse of cytoskeleton, and entrapment of the water inside the cell. This phenomenon, designated here by *hydraulic locking*, is illustrated in Figure 3.1, bottom panel. In that case the fluid efflux imposed by the boundary condition could no longer be sustained and the problem becomes ill-posed. The cellular dehydration trends for different K are compared in Figure 3.8A with the assumption that once hydraulic locking occurs in a cell, it prevails through the freezing. This is a reasonable assumption since the osmotic pressure gradient across the cell membrane rises and acts in favor of hydraulic locking with decreasing temperature. In that case, it is observed that, over a small range of hydraulic conductivities i.e. (1 to 6×10^{-16} $m^2/Pa/s$) just below the physiological range, membrane water transport stops abruptly at different levels of dehydration indicating that hydraulic locking is a possible mechanism that affects the cellular water transport during freezing.

This prediction is supported by the dehydration trends observed in cryomicroscopy experiments where some cells exhibit marked deviations from mean dehydration response as shown in Figure 3.8B. An example is the abrupt stopping of dehydration (red) with a trend similar to predictions, which might indicate the occurrence of hydraulic locking. In addition, a reswelling response where the cell recovers some of its volume after some time is also illustrated (blue). It is possible that, reswelling is caused by transport of intracellular solutes towards the cell membrane. As the cell membrane is impermeable to those solutes, they accumulate near the membrane and decrease, and eventually reverse the osmotic water flux outside the cell. It is also important to note that the locations of greatest cytoskeletal collapse are also

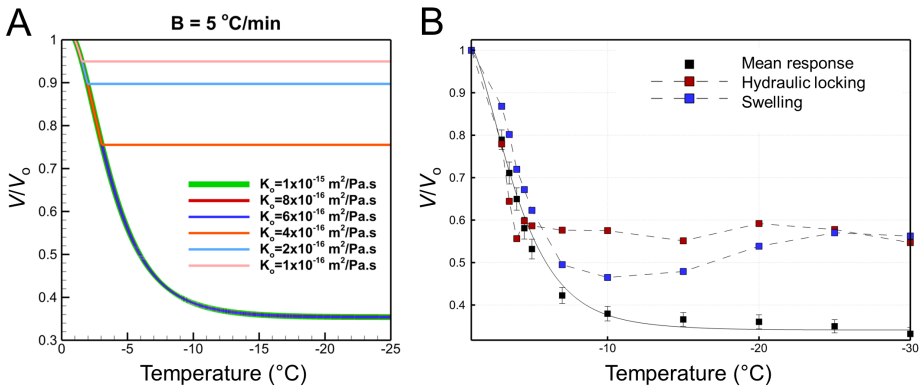

Figure 3.8. Hydraulic locking occurs for decreased values of cytoplasm hydraulic conductivities and results in arrested CWT. (A) Simulated cell volume changes with undeformed hydraulic conductivities lower than 1×10^{-15} m^2/Pa/s. (B) Experimentally observed deviations from mean dehydration response in individual cells. Abruptly stopped dehydration points to possibility of hydraulic locking. Some cells exhibited a reswelling behavior that may be related to transport of solutes in the cytoplasm.

the locations experiencing the greatest intracellular compressive stress. It is possible that, cytoskeletal collapse is one of the reasons of cytoskeletal damage that has been observed upon freezing in previous studies [95, 96].

3.3.4 Estimation of Extracellular Freezing Kinetics

In order to access the rate of ice formation in ETs, latent heat release associated with freezing was measured by DSC. The freezing thermogram showing the rate of latent heat release with decreasing temperature is provided in Figure 3.9. When normalized by the total latent heat release and integrated with respect to time, this signal gives the frozen fraction plotted against the right axes in the figure. It can be observed that ice formation is rapid with more than 80% of the ice forming before the temperature reaches -5 °C. This observation is consistent with the cryomicroscopy results showing that a significant portion of the dehydration occurs within that temperature range.

3.3.5 Simulation of Freezing-induced Tissue Deformation in the Presence of CWT

The directional freezing of engineered tissues was studied in an idealized one-dimensional setting consistent with previous experiments [24, 50, 69]. In this case the freeze front propagates along x-direction with initial location at the edge of the cold post. Results are presented in Figure 3.10. Based on the temperature profiles in Figure 3.10A, the change in the amount of water in the cell and the frozen fraction of the extracellular medium with time were computed for two axial locations: x = 2000 and 4000 m, and are provided in Figure 3.10B and C. The extent of water transport, Figure 3.10B, is greater for $x = 2000$ μm since that region is exposed to freezing temperatures for a longer period of time than for $x = 4000$ μm. The ice formation

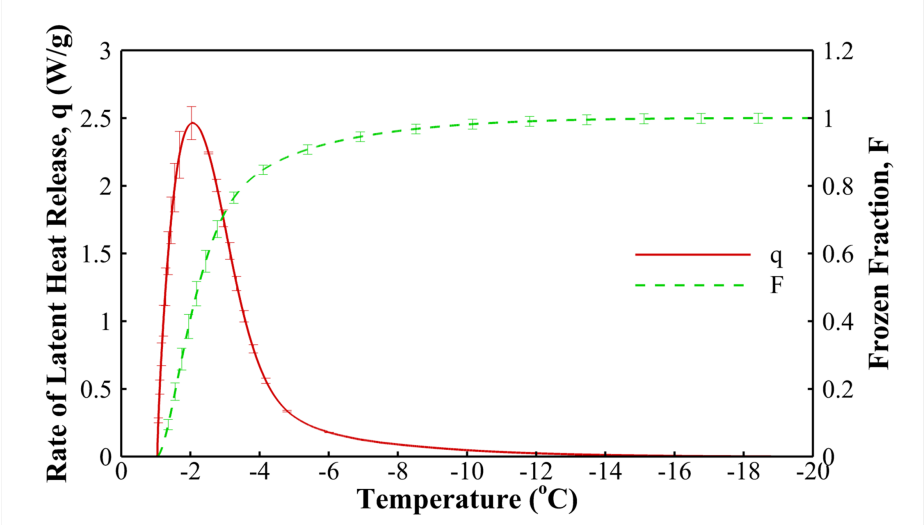

Figure 3.9. Extracellular freezing kinetics in engineered tissues. Rate of latent heat release (solid line) and the frozen fraction calculated by cumulative integration of the rate of latent heat release with respect to time (dashed line).

also occurs faster at $x = 4000$ μm as can be seen from the slope of the frozen fraction, 3.10C. This is mostly due to higher cooling rates observed at this location when compared to $x = 4000$ μm, which is farther away from the cold post. This trend also appears in the estimation of freezing-induced dilatation rate that is shown in Figure 3.10D. As the local temperature is below the phase change temperature, an expansion is predicted with a rate that increases rapidly, attains a peak and decreases gradually. Since both cellular water transport and extracellular ice formation are favored at locations close to the cold terminal, the engineered tissue undergoes a more rapid expansion at $x = 2000$ μm than at $x = 4000$ μm. This result agrees well with the experimental deformation rate profiles in previous studies [24, 50, 69], in which the maximum dilatation is observed right after the freezing interface.

Figure 3.11A shows the isolated effect of the CWT on freezing-induced dilatation for difference cell concentrations in the tissue. It is readily seen that the magnitude of freezing-induced dilatation rate remains approximately the same for concentrations less than 2×10^7 cells/mL but starts to decrease appreciably with further increase in the concentration for both in the presence and absence of CWT. Figure 3.11B shows the variation of relative dilatation rate, $\Delta\dot{e}$ with temperature at various cell concentrations. $\Delta\dot{e}$ indicates the contribution of CWT in tissue deformation rate as defined in eqn. (3.31) It is noted that $\Delta\dot{e}$ becomes larger with increasing concentration, and it can account for nearly half of the deformation for tissues densely packed with cells.

The analysis above reveals that neither the change in concentration of the cells within levels typically encountered in engineered tissues ($< 1 \times 10^6$ cells/mL) nor their osmotic activity in terms of CWT produced an important effect on the magnitude of dilatation rate across the tissue. However, CWT may be significant in native tissues which have significantly higher cellular density and a more complex spatial

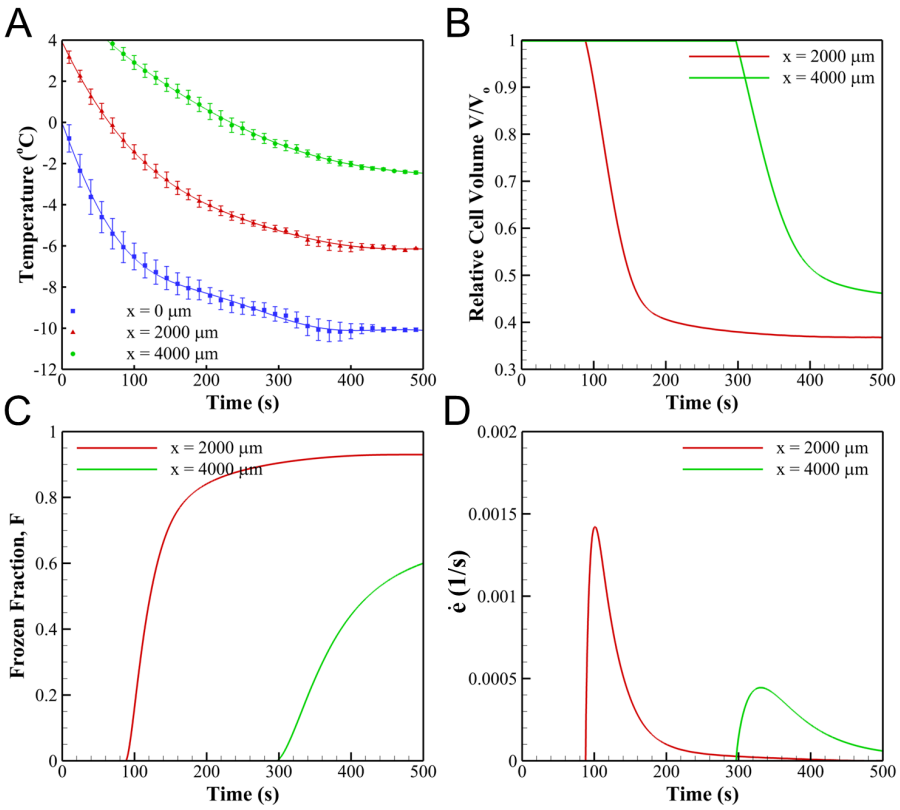

Figure 3.10. Simulation of tissue expansion during freezing in the presence of CWT. The simulations were performed for a one dimensional directional freezing scenario experimentally studied in previous works of Teo [24, 69] and Seawright [50]. (A) Experimentally determined temperature profiles. Adapted from Seawright and Ozcelikkale [50]. The simulated trends for (B) CWT trends, (C) Frozen Fraction, (D) Rate of freezing-induced expansion reported in terms of dilatation rate. x is the distance from the cold post where the freeze front is initiated.

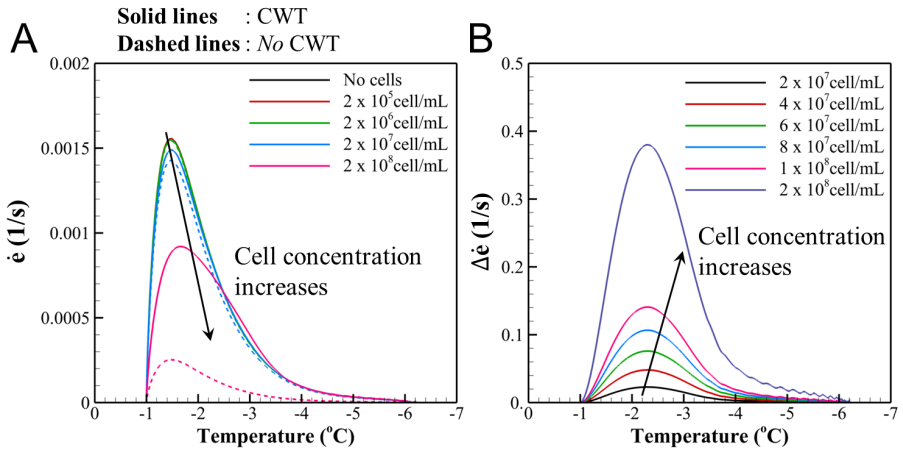

Figure 3.11. Contribution of CWT to freezing-induced tissue deformation rate. (A) The variation of estimated freezing-induced dilatation rate with decreasing temperature for different concentrations of cells in the presence (solid lines) and absence (dashed lines) of CWT. (B) The variation of relative difference of freezing-induced dilatation rate due to occurrence of CWT.

organization compared to ETs. As an example, the chondrocyte concentration in the articular cartilage ranges between 1 to 2×10^7 cells/mL, which is more than an order of magnitude greater than that of typical engineered tissue [4, 97]. The myocyte content in heart tissue is even higher with 1×10^8 cells/mL [98]. Therefore, the effects of the presence and the osmotic activity of the cells should be considered for native tissues as well. As the cell concentration is increased, although the amount of cellular water transport increases, the freezing-induced deformation can become smaller. This is explained by the fact that, for higher concentrations, the cells occupy more space in the tissue, which decreases the porosity and the relative amount of interstitial fluid. The reduction in the water content that is available for extracellular freezing results in a decrease in the freezing-induced deformation rate. The differences between the cases in the presence and absence of CWT indicate that the amount of cellular water excluded to the extracellular space becomes appreciable at high cell concentrations, e.g. $10^7 - 10^8$ cells/mL. As a result, CWT is expected to play a significant role in the freezing-induced deformation of biological tissues.

3.3.6 Implications to Tissue Cryopreservation

Cooling rate is one of the key parameters that determine the outcomes of cryopreservation protocols. Our model provides insight into how cooling rate affects the tissue deformation depending on the composition and biophysical characteristics of the tissue. Examination of Equation (3.30) reveals that tissue deformation rate is directly proportional to the rate of ice formation in the extracellular space, $\partial F/\partial t$. In addition, the magnitude of $\partial F/\partial t$ is related to the cooling rate, B, as follows:

$$\left|\frac{\partial F}{\partial t}\right| = \left|\frac{\partial F}{\partial T} \cdot \frac{\partial T}{\partial t}\right| = B \left|\frac{\partial F}{\partial T}\right| \tag{3.32}$$

where $\partial F/\partial t$ is a function of temperature that has been determined experimentally in our study. Alternatively a functional relationship for $\partial F/\partial t$ based on binary phase diagram of physiological solutions can be found in the literature [99]. Secondly, tissue porosity, ϕ, and cell concentration, C, are the two main tissue characteristics that appear in Equation (3.30) and they are also expected to be important to the deformation of the tissue.

For the sake of discussion, let us consider two limiting cases where, (i) $CV_e \ll \phi$, representing a tissue with low cell content and (ii) $CV_e \gg \phi$, representing a tissue densely packed with cells. The former is an idealization of engineered tissues ($\phi > 0.99$ and $CV_e \ll 1$) and the latter is a case that is well approximated with native tissues. An example to case (ii) is mammalian liver tissue where $\phi < 0.05$ and $CV_e \simeq 0.6$ [100].

For case (i), it can be shown that the first term on the right hand side of Equation (3.30) becomes much greater than the second term. Therefore the dilatation rate can be approximated by:

$$e \simeq \frac{R\phi}{1 + R\phi F}\frac{\partial F}{\partial t} \quad (CV_e \ll \phi) \tag{3.33}$$

where the coefficient of $\partial F/\partial t$ becomes a monotonically decreasing function of time during freezing. Considering Equations (3.32) and (3.33) together, it is seen that, deformation rate is expected to increase with increasing cooling rate. As a result, a slow cooling rate is desirable to minimize the freezing-induced deformation of engineered tissues during cryopreservation.

In case (ii), Equation (3.30) becomes,

$$e \simeq \frac{RC}{1 + RCFV_e}\frac{\partial (FV)_e}{\partial t} \tag{3.34}$$

Therefore dilatation rate is limited by the rate of water exclusion from the cells multiplied by the frozen fraction. Then competing effects of cooling rate on both

extracellular ice formation and cellular water transport dynamics become equally important in determining tissue deformation. In fact, hindrance of water transport by increased cooling rate can be significant enough to counteract the effects of increasing cooling rate on extracellular ice formation. Therefore, for the case of cells with high cell content, it might be possible that there exists an optimal cooling rate that minimizes deformation of the tissue during cryopreservation. This optimal cooling rate depends on the composition of the tissue and cellular water transport parameters of the cells within.

4. EFFECTS OF FREEZE/THAW ON CELL-ECM INTERACTIONS DURING MIGRATION OF FIBROBLAST ON COLLAGEN HYDROGELS

4.1 Introduction

Cryopreservation can enable long term storage of tissues and organs while preserving their structure and functionality [7, 50]. On-shelf graft availability will ultimately improve the logistics of demand-supply chain in transplantation industry [101]. Development of new tissue engineering products also presents a current need for successful tissue cryopreservation protocols. In order to achieve these goals, effects of freezing on biomaterial functionality needs to be understood.

Biosynthetic skin substitutes are tissue engineering constructs that are being developed to improve healing response in deep tissue wounds and skin reconstruction. They find application particularly in treatment of chronic (non-healing) wounds where augmentation of wound closure is necessary [102]. Collagen based acellular constructs are considered for these applications especially as an exogenous provisional matrix at wound site that is initially infiltrated by host cells, remodeled and eventually replaced by regenerated tissue [5]. Fibroblasts play a critical role in this process by synthesizing and remodeling the ECM. For successful healing fibroblasts must migrate into the wound site [103]. The later stages of granulation tissue formation and wound closure depend on proper infiltration of this provisional matrix by fibroblasts. Interactions of fibroblast with the ECM defines the basic functional response that needs to be preserved upon cryopreservation of collagen acellular constructs.

Cell-ECM interactions are complex, involving both migration of cells and deformation of ECM that needs to be considered together to assess functionality. Mechanical

cues induced on cells by the ECM are now known to play a major role in migration [104, 105]. The regulation of single cell migration by ECM mechanical properties and microstructure are well studied [106–109]. However it has been reported that fibroblasts are recruited to the wound site as a group, by so-called en masse movement, rather than as a single cell [110]. This en masse movement suggest a degree of coordination in fibroblast wound healing behavior that can be explained by mechanical cues that arise due to cell-ECM interactions. Traction forces generated simultaneously by multiple cells can deform the compliant ECM and result in bi-directional interactions between cells and their mechanical environment.

While active role of cells in modulating their environment during en masse migration have recently been recognized [111] the dynamics of this process have not been clearly understood. The transients of migration process is important to understand the cell-matrix interactions. For instance, coordinated tissue expansion of epithelial cells is guided by formation of mechanical waves traveling across cells [112, 113]. Fibroblasts lack the strong cell-cell adhesions found in epithelial cells, limiting the effect of such direct forces on cell-cell interactions on migration. It is possible that spatiotemporal substrate deformation and stresses are the guiding factors in en masse fibroblast migration. In this study, this question is addressed by performing time-resolved measurements of cell and ECM movement during en masse migration of fibroblasts on collagen hydrogels. Collagen hydrogels served as the model system for collagen based acellular constructs. Effects of freeze/thaw (F/T) were tested against unfrozen controls where independent changes were induced in unfrozen hydrogel microstructure by varying collagen concentration. Migration on these compliant hydrogels were also compared to that on collagen coated coverslips. Hydrogel deformation was quantified by a newly developed image based tissue deformetry technique using incremental particle image velocimetry [114, 115]. Results indicate to decreased cell-mediated

matrix deformation in the case of F/T that is not explained by either the decrease of bulk mechanical properties upon F/T or weakening of hydrogel microstructure by decreasing collagen concentrations. The results suggest freezing-induced changes in collagen structure adversely affect cell-matrix adhesion.

4.2 Material and Methods

4.2.1 Cell Culture and Reagents

Early passage human foreskin fibroblasts, by courtesy of Dr. Frederick Grinnell at Department of Cell Biology, University of Texas Southwestern Medical Center were maintained in culture medium (DMEM/F12, Invitrogen, NY) supplemented with 10% fetal bovine serum, 2 mM L-glutamine, and 100 g/ml penicillin/streptomycin. The fibroblasts were cultured up to 15^{th} passage in 75 cm^2 T-flasks at 37°C and 5% CO2. The cells were consistently harvested at 80% confluency by using 0.05% trypsin and 0.53 mM EDTA.

For selective cell seeding, 2×10^5 cells were retrieved from flask and centrifuged at 2000 rpm for 4 minutes. Cell pellet was transferred into 500 μL of targeted quantum dot solution (Q-tracker 655, Invitrogen, NY) diluted in culture medium at 1:500 ratio according to manufacturer's protocol and incubated for 30 minutes. Then cells were centrifuged two times while being washed with unsupplemented culture medium in between. The resulting cell pellet was resuspended in 80 μL of unsupplemented culture medium and used in tissue expansion assay as described in section 4.2.3.

Experiments were conducted in a promigratory growth factor medium with reduced serum content that contained culture medium supplemented with 1% fetal bovine serum, 2 mM L-glutamine, and 100 g/ml penicillin/streptomycin and 50 ng/mL human platelet-derived growth factor (PDGF-BB, Millipore, MA).

4.2.2 Collagen Hydrogels

Collagen hydrogels were prepared as described previously in section 2.2.1 with a few modifications.

500 μL of neutralized collagen solution was prepared with previous protocol except 25 μL of distilled water was substituted for stock solution of fluorescent microspheres (G1000B, Thermoscientific) with 10 μm diameter and stock concentration of 1.8 $\times$ 10^7 particles/mL. Hydrogels were allowed to polymerize by incubating at 37°C for 30 minutes. Then sample was sealed with laboratory parafilm to keep the hydrogels hydrated during incubation. The hydrogels were used in experiments after overnight incubation.

Experiments were conducted with three collagen concentrations, 1.5, 3.0 and 6.0 mg/mL. In order to study the effects of freeze/thaw treatment, hydrogels with 6.0 mg/mL concentration were frozen to -60°C as described in section 2.2.3. During this process, the sample was positioned on DSS such that prospective location of seeding region was frozen and freezing temperature increased towards other side of the hydrogel starting from the migration baseline. This protocol mimicked the direction of temperature gradients that occur during typical tissue cryopreservation procedures [70]. F/T hydrogels were incubated for 3 hours post-thaw before being used in experiments.

4.2.3 Tissue Expansion Assay

Figure 4.1 illustrates the tissue expansion assay in this study. A customized sample holder was prepared by bonding a rectangular frame, a blocker and four support posts, all made from polydimethylsiloxane (PDMS), to the interior of a 1-well chamber slide (Nunc^{TM} Labtek-II^{TM}, Fisher Sci.) as shown in Figure 4.1A. The bonding was carried out by treatment of each surface by oxygen plasma, bringing them into contact and

baking at 75 °C overnight. Use of this customized chamber with reduced size and additional structural support enabled reproducible preparation of samples with small amounts of collagen solution and growth factor medium.

Cells were selectively seeded on collagen hydrogels in four steps illustrated in Figure 4.1B and described below as follows:

(i) Neutralized collagen solutions were prepared as described in section 4.2.2. Then 400 μL of solution was dispensed and uniformly distributed in the region bounded by the PDMS frame. Upon incubation at 37 °C, hydrogels with rectangular sections that have thicknesses varying between 0.9 and 1.3 mm were obtained.

(ii) A hollow PDMS stamp was sterilized by 70% ethanol and ozone and cleaved by an adhesive tape. Then it was placed on top of the hydrogel. The PDMS stamp sealed with the underlying hydrogel surface and formed a rectangular cavity. 80 μLof culture medium containing fibroblasts was dispensed in that region and the sample was incubated for 30 minutes during which cells settled down onto the surface and attached to the substrate.

(iii) At the end of incubation culture medium was removed and stamp was carefully lifted from hydrogel surface by a pair of tweezers.

(iv) The chamber was filled by 1 mL of promigratory growth factor medium.

Figure 4.2 presents the sample layout obtained as a result of above procedure. Cells formed a densely packed rectangular monolayer from which they freely migrated out into the unpopulated regions. In the absence of posts, traction forces generated by cells in this region often caused detachment of hydrogel at boundaries. In that case substantial translation and distortion of the hydrogel over the course of experiment precluded meaningful measurements of deformation and migration. Use of support posts helped reduce the overall stress in hydrogel and enabled reproducible generation

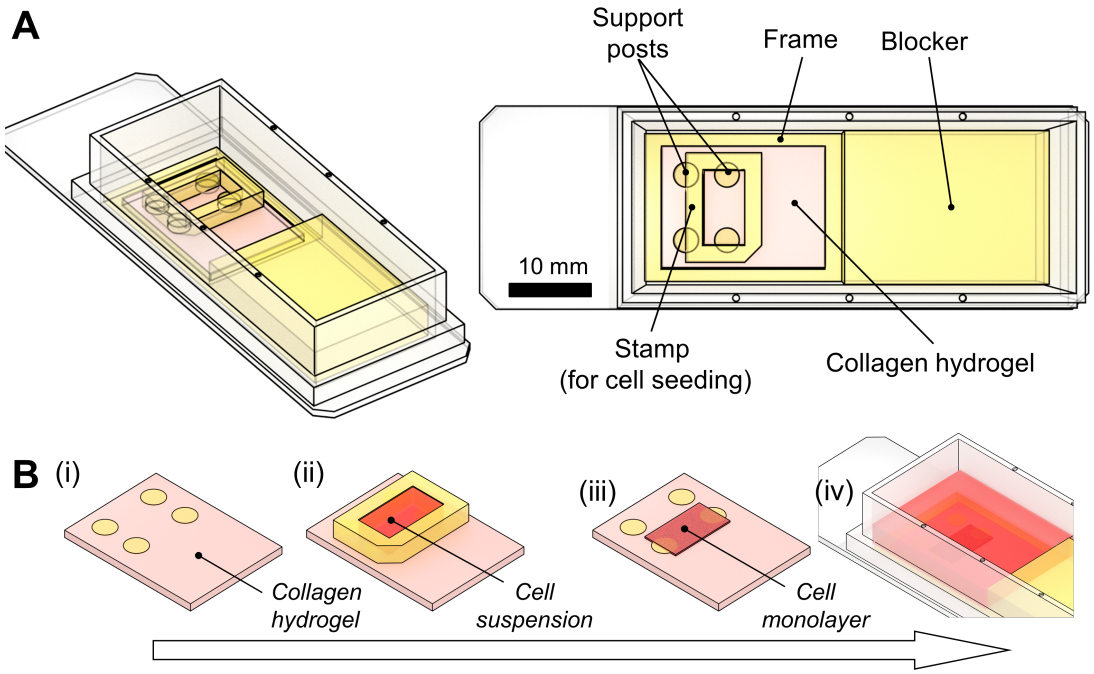

Figure 4.1. An illustration of tissue expansion assay (A) Customized chamber slide as a sample holder. (B) Steps of selective cell seeding.

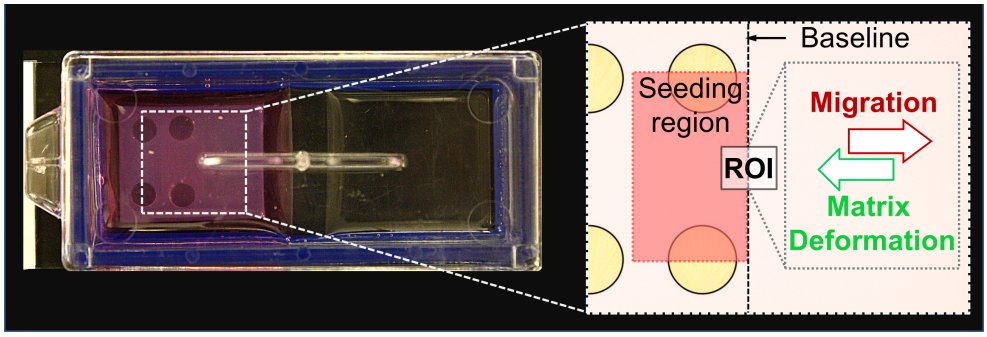

Figure 4.2. Sample layout and region of interest in experiments.

of migration settings. Time-lapse measurements were performed at a region of interest (ROI) located at the center of right hand side seeding boundary. Both cell migration and hydrogel deformation were observed in this ROI during the experiments.

4.2.4 Fluorescence Microscopy

Sample was placed in a stage top incubator (Okolab H501-EC, Warner Instruments, CT USA) and imaged under an inverted epifluorescence microscope (IX71, Olympus, Japan) with 10X objective every 15 minutes for 24 hours. Figure 4.3A presents a partial view of the initial imaging field of view (FOV) where fibroblast monolayer and unpopulated collagen gels are separated by a distinct baseline. The origin of the coordinates used for data analysis also coincides with the baseline. At each time point images were acquired at multiple focal planes 100 μm apart with positions between hydrogel surface and 500 μm depth into the hydrogel. In addition to the bright field illumination, fluorescence imaging at with two excitation/emission (ex/em) wavelengths was performed. The fluorescence signals associated with extracellular markers i.e. 10 μm microspheres, and intracellular markers i.e. quantum dots, were acquired at FITC (ex/em: 495 nm / 519 nm) and TRITC (ex/em: 547 nm / 573 nm) channels respectively. All images were captured by a CCD camera (Retiga

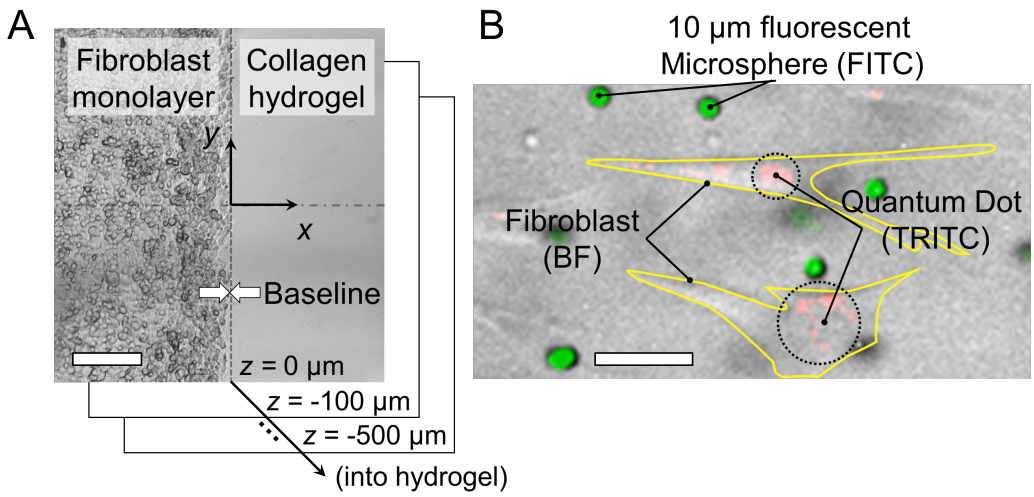

Figure 4.3. Time-lapse fluorescence microscopy for observation of simultaneous cell migration and tissue deformation. (A) A partial view of imaging ROI showing the migration baseline and coordinate system. Images were acquired at multiple focal planes with positions ranging from hydrogel surface ($z = 0$ μm) to 500 μm into the hydrogel ($z = 500$ μm). (B) Composite images with fibroblast and intracellular and extracellular markers.

2000R, Qimaging, Canada). Figure 4.3B shows an example of composite images with fibroblast and intracellular and extracellular markers.

Cell migration was quantified by considering the changes in distribution of the cells over time with respect to baseline. For this purpose, quantum dot intensity was averaged over y-direction and normalized based on the intensity at seeding region at each time point.

4.2.5 Dynamic Mechanical Analysis (DMA)

Mechanical properties of collagen gels were measured by a dynamic mechanical analyzer (Q800, TA Instruments, DE) using circular hydrogel specimens with 12 mm diameter and approximately 3 mm thickness. Force-displacement measurements were performed during unconfined compression of the hydrogel between two parallel plates

by application of a loading ramp from 0 to 10 mN with a rate of 2 mN/min. During compression, the gel was fully immersed in physiological saline solution (PBS) and free flow of interstitial fluid in and out of the gel was allowed through its lateral boundaries.

The dominant hydrogel behavior during unconfined compression was considered to be poroelastic. The problem was modeled based on previous work of Armstrong et al. [116] that reported an analytical solution for unconfined compression of a poroelastic solid. Armstrong et al. [116] provides a relationship between the nondimensional force and resulting strain in Laplace transform space. The details of their analysis is provided in the reference [116] and only the results are outlined here.

$$\hat{\varepsilon}(s) = \hat{f}(s) \cdot \left[\frac{I_0(\sqrt{s}) - \frac{2\mu_s}{H_s} \frac{I_1(\sqrt{s})}{\sqrt{s}}}{3I_0(\sqrt{s}) - \frac{8\mu_s}{H_s} \frac{I_1(\sqrt{s})}{\sqrt{s}}} \right] \tag{4.1}$$

where $\hat{\varepsilon}(s)$ and $\hat{f}(s)$ are the Laplace transform of axial strain $\varepsilon(t)$ and nondimensional force $f_*(t)$. I_0 and I_1 are the Bessel functions of second kind. Then experimental stress strain curve was fitted with model predictions to estimate the elastic modulus and hydraulic conductivity.

4.2.6 Tissue Deformetry by Incremental Particle Image Velocimetry (I-PIV)

In order to determine the hydrogel displacement, Time-lapse fluorescence images of extracellular markers were analyzed by digital particle image velocimetry (PIV) [117]. PIV is used to estimate the velocity field by cross-correlation of a pair of images acquired at successive time points. The velocity field is spatially resolved due to division of images into multiple interrogation windows. PIV image analysis in this study is based on a multi-pass window deformation technique [118] implemented in commercial software, DaVis, (LaVision, MI). Interrogation windows size was iteratively

decreased from 256×256 to 64×64 pixels. 3 to 4 iterations were performed at each window size. The overlap between interrogation windows was set to 50% for all window sizes.

The result of PIV analysis is a velocity field obtained at fixed points on image i.e. based on a Eulerian reference frame. The actual movement of hydrogel,on the other hand, is represented by material points that travel through this velocity field. The trajectories of material points were therefore obtained by seeding a grid of hypothetical particles in the FOV at first time point and following their path through integration along the PIV velocity field. The integration was performed using a second order accurate time marching scheme. Since the material displacement was obtained by integration of PIV velocity field, this technique is referred to as *incremental* PIV (I-PIV). Similar image based deformetry techniques have been reported in the literature [114]

As an alternative method to estimate the hydrogel displacement and a mean to validate the PIV field, trajectories of extracellular markers were also determined by single particle tracking (SPT). SPT was performed using Trackmate [119] distributed in Fiji/ImageJ image analysis software [59]. The resulting trajectories were manually inspected for accuracy before comparing them with trajectories obtained based on PIV. Ideally, trajectories integrated from the PIV field should be same as the trajectories of extracellular markers. The resulting material point tracks are shown in Figure 4.4A. In order to assess the accuracy of tracking by PIV, the motion of the ECM markers tracked by PTV were simulated by PIV as described above. The displacements of the resulting tracks were compared against those obtained from PTV as illustrated in Figure 4.4B. The results obtained by PIV were found to be in good agreement with PTV but showed slight underestimation at high levels of displacement.

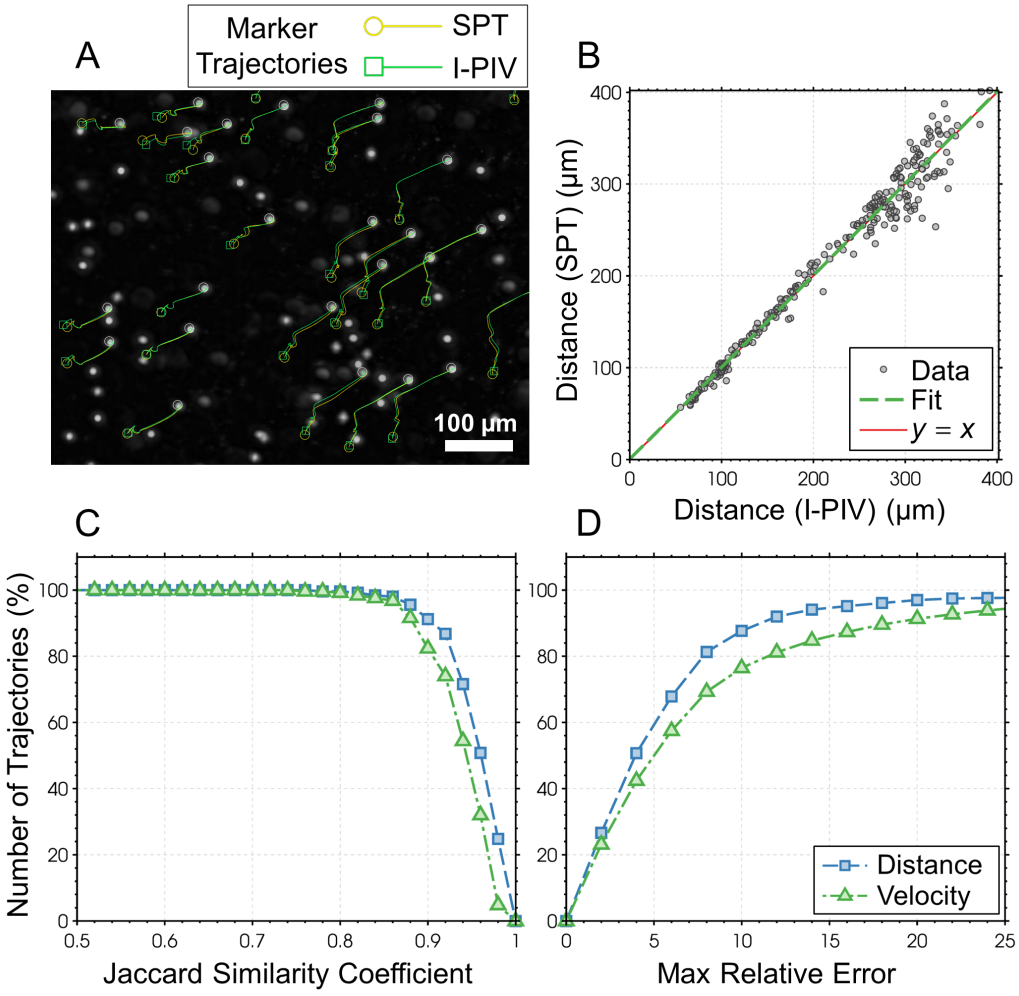

Figure 4.4. Validation of incremental PIV tissue deformetry. (A) Marker trajectories determined by incremental PIV (I-PIV) and single particle tracking (SPT). (B) Comparison of final marker displacements I-PIV and SPT for 250 randomly selected markers. y = x line indicates perfect match. (C) The degree of similarity between I-PIV and SPT based distance and velocity magnitudes. y-axis indicates the percentage of trajectories that satify the minimum level of similarity coefficient given in x-axis. (D) Maximum relative error of I-PIV based distance and velocity magnitudes with respect to SPT.

Calculation of areal strain was performed as described in Section 3.2.4. The calculated deformation metrics can be related to hydrogel stresses by an appropriate material model. In this study, collagen hydrogel was assumed to be a hyperelastic solid with Neo-Hookean constitutive model where Cauchy stress tensor, σ is given by,

$$\sigma = \frac{\mu_1}{J^{5/3}} \left(\mathbf{B} - \frac{1}{3} tr\left(\mathbf{B}\right) \mathbf{I} \right) + K_1 \left(J - 1\right) \mathbf{I} \tag{4.2}$$

where $\mathbf{B}$ is the left Cauchy-Green deformation tensor related to deformation gradient by $\mathbf{B} = \mathbf{F}\mathbf{F}^T$, J is the infinitesimal volume change as defined previously, $\mathbf{I}$ is the Kronecker Delta and μ_1 and K_1 are material constants that are approximated by the shear modulus and bulk modulus of the hydrogel, respectively [120]. Therefore, based on the knowledge of the material properties obtained by DMA measurements, and deformation metrics obtained by I-PIV tissue deformetry, it was possible to estimate the hydrogel stresses.

4.3 Results and Discussion

4.3.1 Cell Migratory Behavior on Collagen Hydrogels

Cell migratory behavior on hydrogels was markedly different from that on collagen coated coverslip. Figure 4.5 presents micrographs of migration baseline acquired at several time points for the two cases. It was seen that cells on hydrogel first remodeled this deformable substrate by contraction. The mass contraction of fibroblast resulted in displacement of migration baseline from its initial position towards seeding region. Only after a partial release of this stress, cells started migrating without any apparent sign of coordination. This initial remodeling phase was not observed on coverslip. In that case, cells emerged from the baseline as a group after around 4 hours and performed a unidirectional stream-like movement.

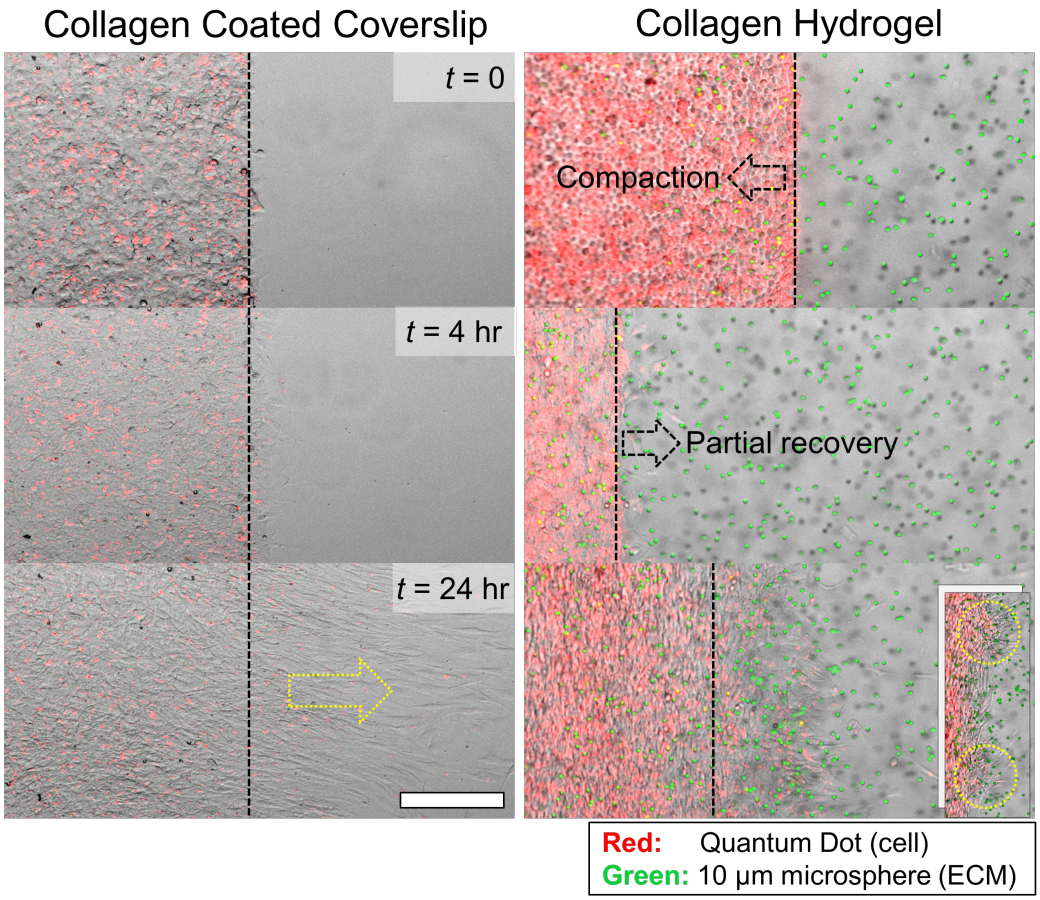

Figure 4.5. Cell migratory behavior on collagen coated coverslip (left) vs. collagen hydrogel (right).

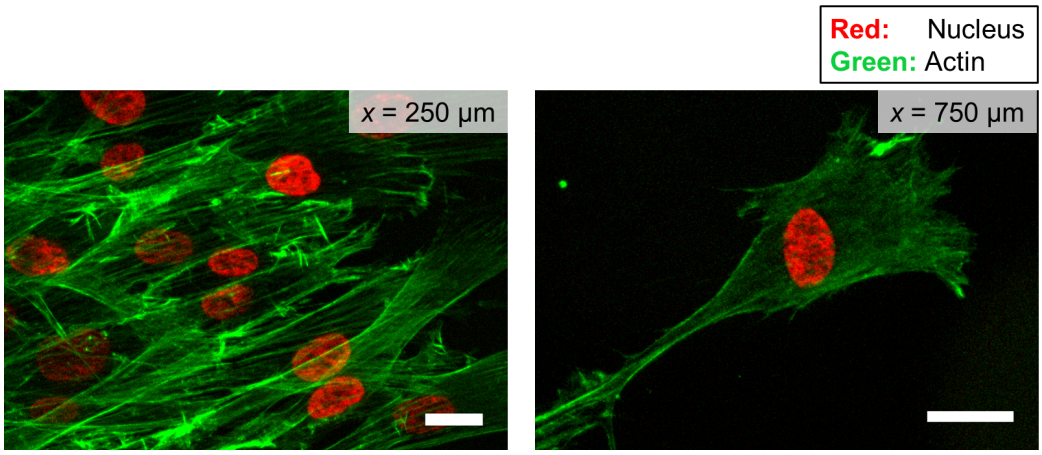

Figure 4.6. Cell morphology near vs. far away from the migration baseline. Scale bars are 20 μm.

Cell morphology was different at near and far away from the baseline. The migration field near the baseline was densely populated with cells that were partially overlapped and showed elongated morphology. Individual cells that migrated far away from baseline exhibited spreading with extended lamellipodia as shown in Figure 4.6.

The localization of cells through the course of experiments as determined by quantum dot intensities is illustrated in Figure 4.7A for representative coverslip and hydrogel cases. The previously observed differences of cell migratory behavior between coverslip and hydrogel are also observed here. In both cases, cells start to migrate after several hours as noted by an increase in quantum dot intensity on the right hand side of baseline. The comparison of migration distances after 24 hours is presented in Figure 4.7B. Cells traveled significantly longer distances on coverslip than on hydrogel. The distance traveled on hydrogel increased by increasing collagen concentration, however the differences were not significant. The migration distance wasn't affected by freeze/thaw either. Furthermore, the onset of migration was delayed on hydrogels (Figure 4.7C) and the amount of delay increased by decreasing gel concentration and freeze/thaw.

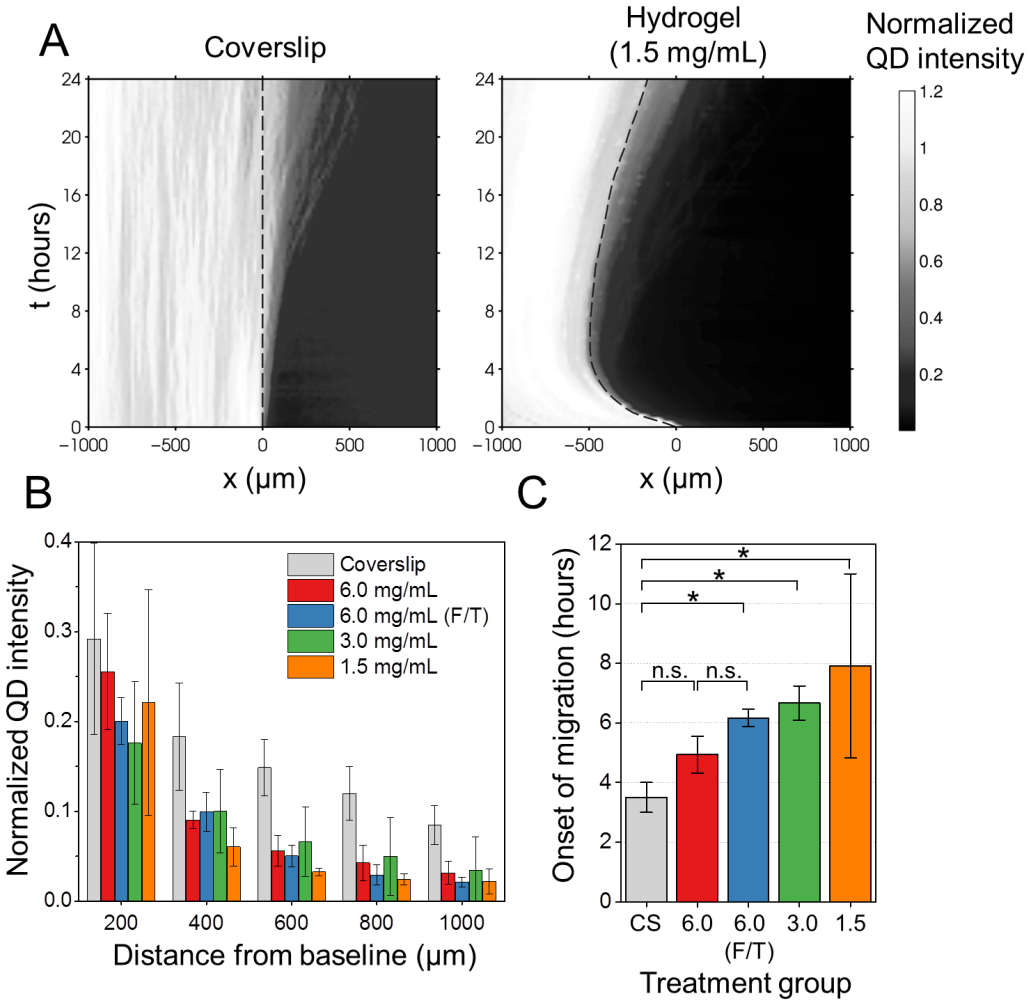

Figure 4.7. Quantification of cell migration. (A) Evolution of y-averaged quantum dot (QD) intensity over the course of experiments. Intensity is normalized at each time point with respect to the mean intensity in the seeding region. (B) Migration distances after 24 hours. (C) Onset of migration.

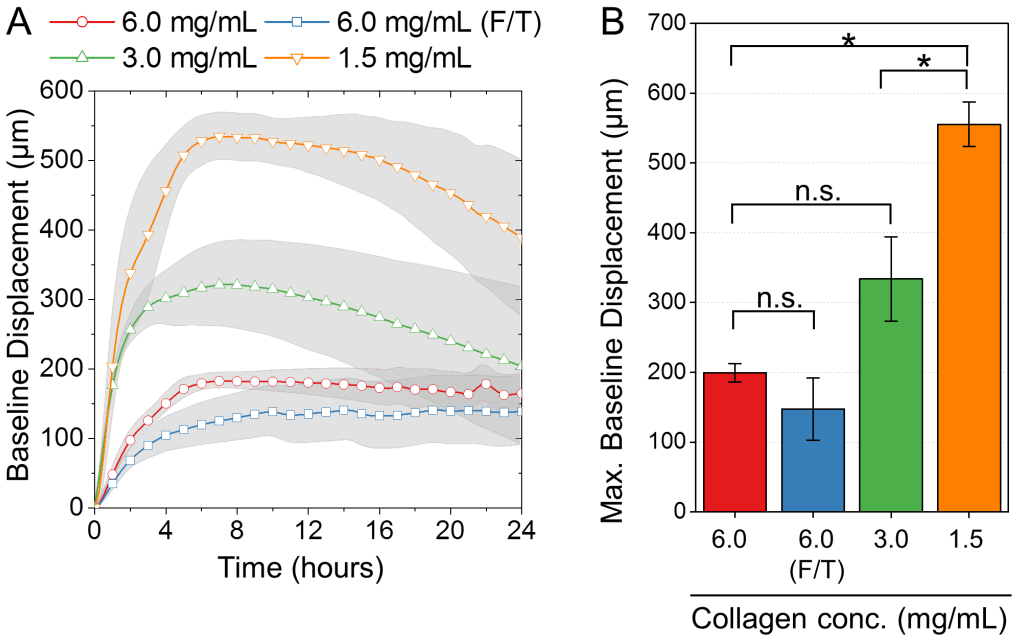

Figure 4.8. (A) Evolution of baseline displacement. (B) Maximum baseline displacement.

4.3.2 Cell-mediated Hydrogel Deformation

Using I-PIV based tissue deformetry, the extent, distribution and evolution of cell-mediated hydrogel deformation were estimated. Figures 4.8A and 4.8B compare the amount of baseline displacement on hydrogels that was observed during the remodeling phase. 1.5 mg/mL showed the greatest amount of baseline displacement. The amount of displacement decreased by increasing collagen concentration and the differences between groups were significant. Interestingly hydrogel treated by F/T showed less baseline displacement than the unfrozen case, however the difference was not significant.

Timelapse deformation contours presented in 4.9 compare deformations of hydrogels with low (1.5 mg/mL) and high (6.0 mg/mL) density collagen. Within the first few hours, seeding region ($X < 0$) underwent gradual compaction indicated by the negative

values of areal strain. The compaction is considered to be due to attachment and spreading of fibroblast. An increasing expansion in the migration region was also observed. After onset of migration the trend started to get reversed and matrix in migration region was compressed. The region of compression increased as the migration front advanced. After 24 hours, there was a net expansion in the seeding region and a net compression in the migration region particularly in the vicinity of the baseline. The magnitude of compression was greater and the region affected was wider for low collagen density when compared to high collagen density. The evolution of mean areal strain as affected by different factors is displayed in Figure 4.10. First of all, it is seen that deformation is most prominent at the gel surface and it is attenuated into the hydrogel indicating that deformation is a local surface phenomena (Figure 4.10A). Furthermore the amount of deformation increases and deformation becomes less uniform with decreasing collagen concentration (Figure 4.10B). Interestingly the amount of deformation decreases by freeze/thaw. Figure 4.11A shows the mean baseline deformation through the course of experiments. It is clear that overall deformation at the baseline was compressive and increased by decreasing collagen concentration. Highest magnitudes of deformation were attained at the end of experiments. However the deformations at the onset of migration were significantly less and were comparable for all treatment groups as presented in Figure 4.11B.

4.3.3 Cell-mediated Hydrogel Stresses

In the next step, cell-mediated stresses applied on hydrogels were estimated based on the measured deformation. In order to link deformation to stress the knowledge of hydrogel mechanical properties is necessary. For this purpose, poroelastic properties of hydrogels were characterized using dynamic mechanical analysis. Results are shown in Figure 4.12. Elastic modulus was found to be between 150 and 700 Pa and showed

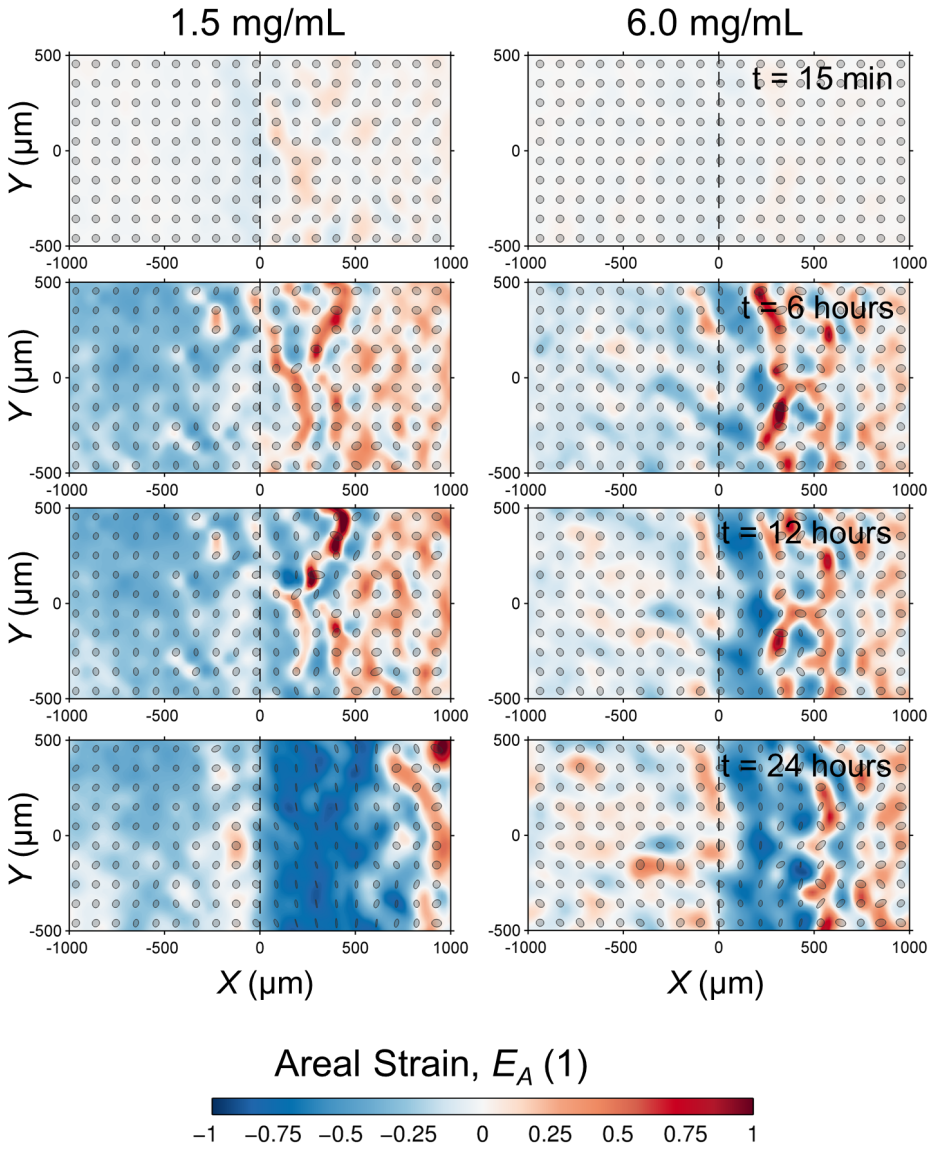

Figure 4.9. Spatiotemporal volumetric strain contours for low density (1.5 mg/mL) and high density (6.0 mg/mL) hydrogels. Ellipses indicating principal stretch directions are also shown.

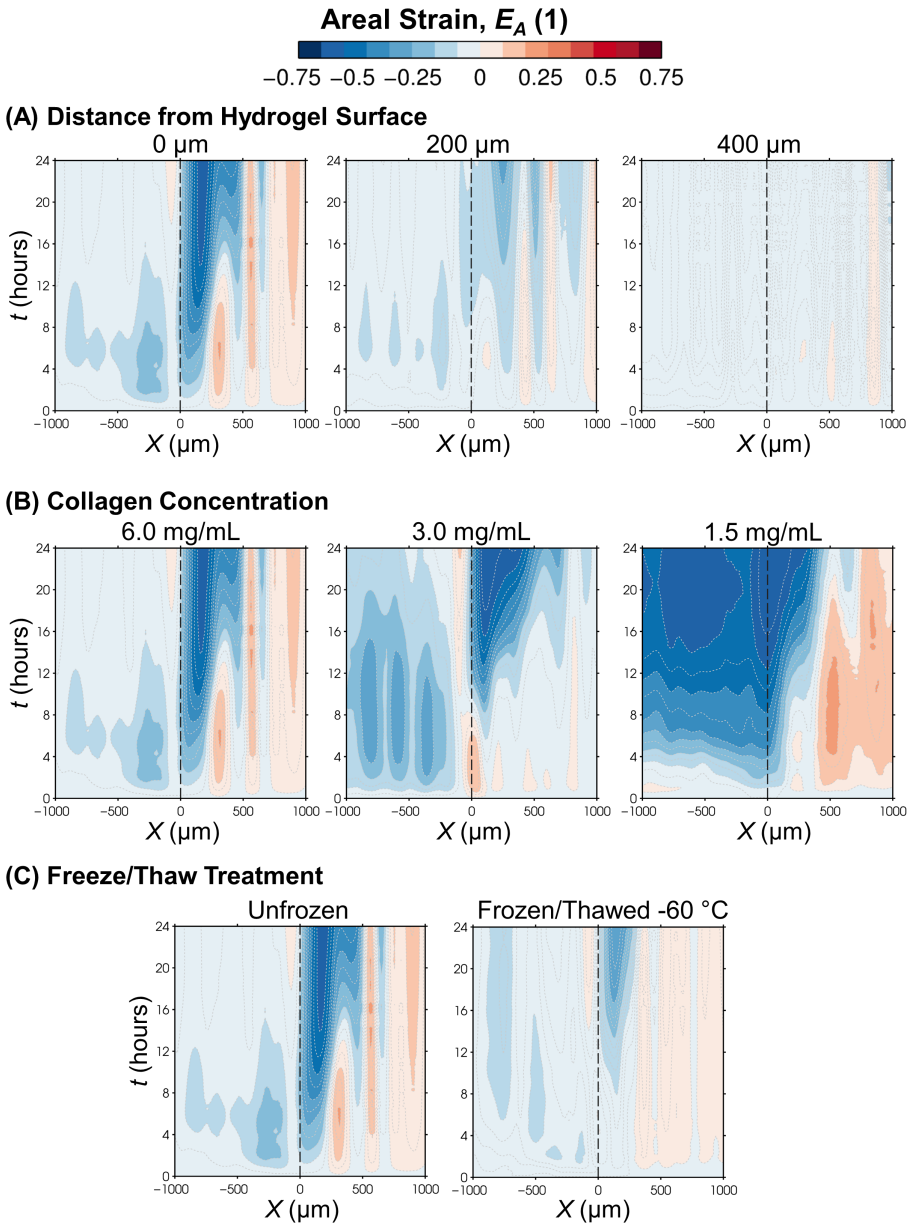

Figure 4.10. Mean areal strain kymographs. Effects of (A) distance from hydrogel surface (into the hydrogel), (B) collagen concentration, (C) freeze/thaw treatment.

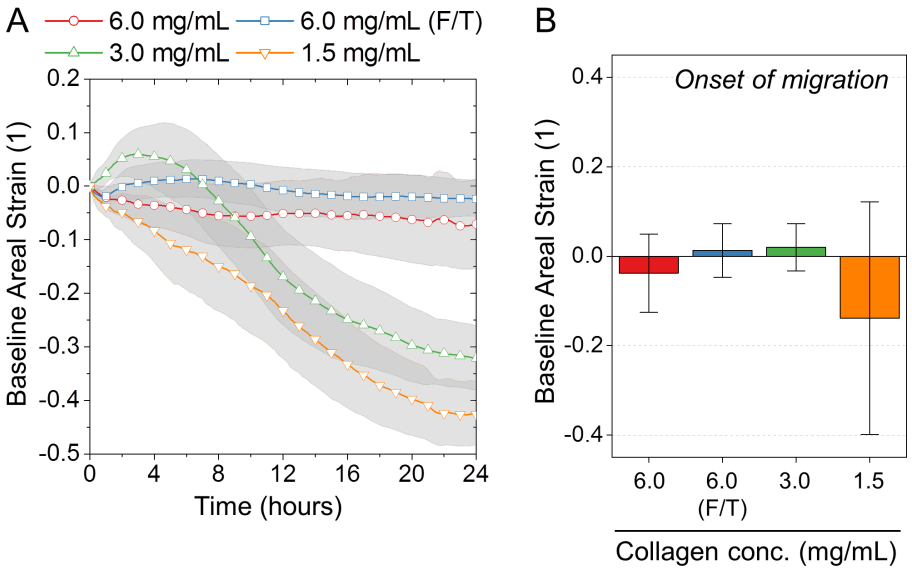

Figure 4.11. (A) Evolution of baseline areal strain in terms of areal strain over 24 hours of experiment. (B) Baseline areal strain at onset of migration.

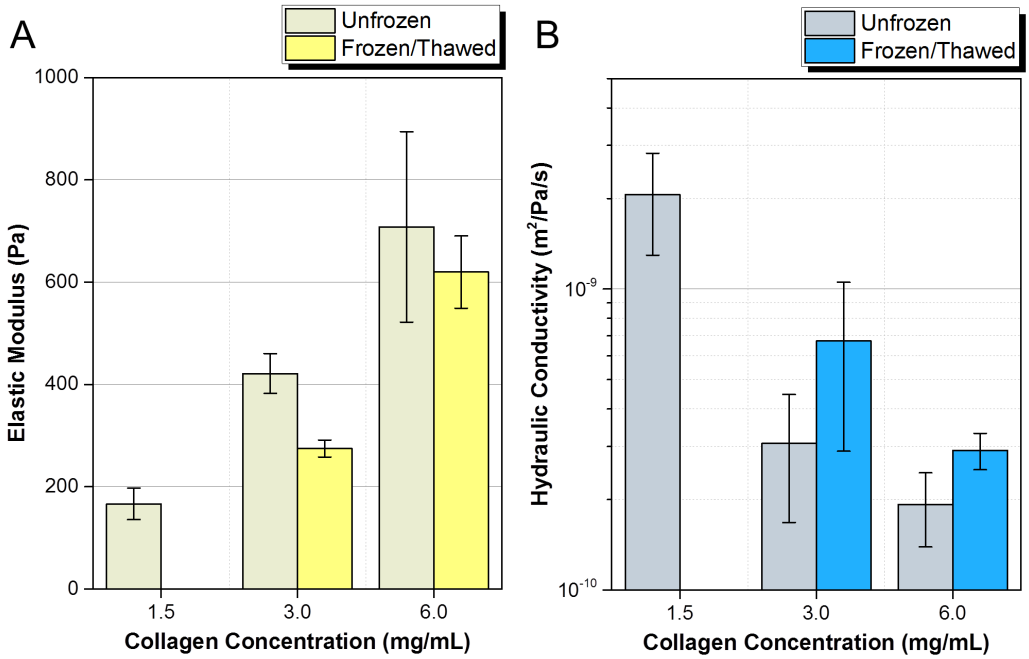

Figure 4.12. (A) Elastic modulus and (B) hydraulic conductivity of collagen hydrogels as measured by DMA.

a significant increase with collagen concentration. F/T treatment resulted in a notable decrease, between 10 and 35%, in elastic modulus with respect to unfrozen. However the differences were not statistically significant for either 6.0 or 3.0 mg/mL collagen concentrations. Hydraulic conductivity showed a reverse trend. It decreased with increasing collagen concentration and increased upon freeze/thaw treatment. The values were between 1×10^{-10} and 2×10^{-9} m^2/Pa·s. The elastic modulus and hydraulic conductivity values for collagen hydrogels are summarized in Table 4.1. The elastic modulus values were used to estimate hydrogel stresses from deformation.

Figure 4.13A illustrates the comparison of cell-mediated traction forces on unfrozen vs. F/T hydrogels. Cells apply lower levels of traction stresses on F/T when compared to unfrozen hydrogel. It is also observed that stresses applied on the hydrogel at the onset of migration get diminished at lower collagen concentrations as shown

Table 4.1. Elastic modulus and hydraulic conductivity of collagen hydrogels as measured by DMA. Values are reported as mean ± standard deviation.

Treatment	Collagen Conc. (mg/mL)	E_s (Pa)	$K_{hyd} \times 10^{10}$ (m^2/Pa·s)
UF	1.5	166.5 ± 30.8	21 ± 7.6
	3	421.5 ± 38.9	3.1 ± 1.4
	6	708.1 ± 186.3	1.9 ± 0.5
F/T	1.5	-	-
	3	274.9 ± 16.5	6.7 ± 3.8
	6	620.0 ± 70.7	2.9 ± 0.4

in Figure 4.13B. These stresses include normal stress in x-direction, magnitude of maximum principle stress and cell-mediated traction force in x-direction per unit area. It is important to note that traction force is associated with significant variability within treatment groups. This is partly explained by differentiation of stress field for calculation of traction force, that could have amplified the noise in displacement measurements.

4.3.4 Effects of F/T on Cell-ECM Interactions

In the light of these findings, it is concluded that F/T treatment can result in changes in hydrogel structure that affects cell migration behavior. The changes are subtle in the sense that they generally didn't resulted in statistically significant differences with respect to unfrozen. However, overall trends indicate that onset of cell migration on F/T hydrogels is delayed. Furthermore bulk mechanical properties are decreased upon F/T. This trend is similar to reduction of mechanical property in unfrozen hydrogels by the use of lower collagen concentrations (3.0 and 1.5 mg/mL compared to 6.0 mg/mL). However F/T and lowered collagen concentrations resulted in distinctly different deformation responses of hydrogels. Hydrogels with 3.0 and 1.5 mg/mL collagen concentrations deformed significantly more than 6.0 mg/mL. In contrast 6.0 mg/mL (F/T) deformed even less than its unfrozen counterpart. This was accompanied by decreased amount of traction forces that were applied by the cells on matrix upon F/T. These results could indicate to diminished ability of cells to attach on F/T collagen matrix. Microstructural changes associated with independent modulation of collagen concentration in unfrozen hydrogels do not show this trend. Altered collagen fibril structure upon F/T that was studied in Chapter 2 is a potential reason for differences observed in interactions between fibroblast and collagen ECM upon F/T.

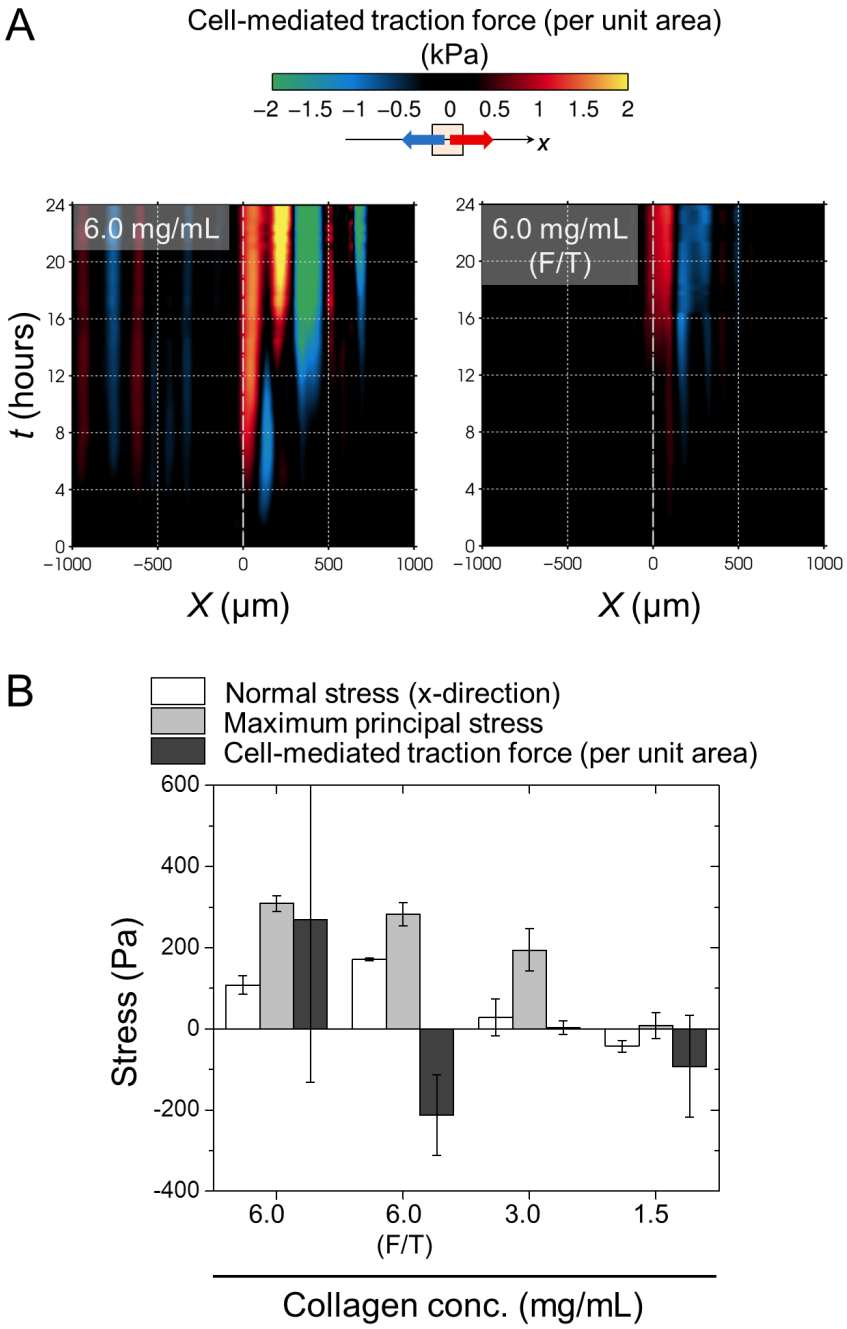

Figure 4.13. Cell-mediated stresses on collagen hydrogel. (A) Kymographs comparing development of cell-mediated traction forces on unfrozen vs. F/T hydrogels. (B) Comparison of baseline normal stresses and traction forces at the onset of migration.

5. CONCLUSIONS

In this dissertation, freezing induced deformation processes that occur at multiple length scales involving nanometer-scale protein fibrils, single cells and whole tissues were studied.

In Chapter 2 it is found that thermal stability of collagen ECM can be different before and after freeze/thaw. However the difference is observed only in a hydrogel environment where collagen has assembled into fibrils. Supported by structural evaluation of collagen and biophysical modeling, these results indicate to a type of fibril damage that is by freezing-induced expansion of intrafibrillar fluid. Therefore the main cryo damage mechanism in this study is found to be a deformation process that elicits itself in post-thaw thermal stability. In contrast, thermal stability is preserved upon freeze/thaw if collagen is maintained at macromolecular state. In other words momentary exposure to temperatures as low as -60 °C does not seem to have a lasting effect on molecular collagen. These findings are reassuring given the concerns on low temperature stability of proteins [28–30]. Collagen considered in this study[1] appears to be tougher than some other proteins that has undergone cold denaturation well above -60 °C [34, 35].

The findings of Chapter 2 also calls attention to main mode of cryo damage in tissue ECM. ECM is deformed by freeze/thaw at both fibril and microstructural levels. Therefore, even in the absence of thermodynamic/biochemical cryo damage, structural/mechanical effects associated with ice formation can lead to changes in collagen

[1]Type-1 rat tail collagen, Type-1 collagen is the most abundant variant of this protein in human body. There are over 20 other types of collagen each with distinct molecular structure and potentially different freeze/thaw response [121].

ECM. Ironically, some of these changes are reflected in post-thaw thermodynamic properties such as thermal denaturation temperature. Therefore it is interesting to note that one of the common practices in calorimetric research that uses collagen tissue extracts is to keep the specimens at frozen storage until they are used in experiments e.g. [53, 122]. This practice now needs to be avoided given it is clear that freeze/thaw introduces a confounding effect in post-thaw thermal denaturation measurements.

Since the bulk tissue ECM is destabilized when frozen/thawed, this makes it more vulnerable to subsequent heating effects. Therefore it may be possible to use this newly found destabilizing effect of freeze/thaw as a way of *preconditioning* the target tissue in hyperthermia therapy where treatment action is partly by denaturation of extracellular collagen. Collagen destabilized by freeze/thaw would require reduced amount of heat during the treatment and could help lower the risk of damage to surrounding tissues by limiting the diffusion of locally applied heat. Since freezing alone is damaging to various tissue components analysis of the ultimate outcome of treatments with such preconditioning would be complex. However the computational model presented in Chapter 2 can provide a starting point by predicting the destabilizing effects freeze/thaw on tissue ECM based on specific information of collagen fibril-level porosity. Finally, since collagen molecule remains intact but its fibril assembly and matrix level microstructure are damaged, changes in other functional properties of ECM in tissue environment, such as such load bearing capacity are also expected. This expectation is indeed verified in Chapter 4 where a decrease in elastic modulus is found upon freeze/thaw.

Chapter 3 focused on cell and tissue-level deformation mechanisms centered around osmotically driven cellular water transport which occurs during freezing. The first part of this study investigated implications of a previously unconsidered coupling between intracellular deformation and cellular water transport. A poroelastic model

of cytoplasm developed in this study, combined with previously established membrane transport models [43], predicts that the hydraulic conductivity of the cytoplasm is the key transport property that governs intracellular deformation. For physiologically relevant hydraulic conductivities, cell exhibits a spatially heterogeneous deformation pattern where the highest deformation occurs in the vicinity of the cell membrane while the center of the cell remained relatively undeformed. Consideration of lower hydraulic conductivities were marked by complete collapse of cytoskeleton, and entrapment of water inside the cell, phenomena termed in this study as *hydraulic locking*. The predictions of the model was experimentally verified by side experiments that estimated intracellular deformation during freezing by fluorescence particle tracking. The findings of this study can explain the cell-dependent freezing deformation response, observed even among cells from the same population.

In the second part of Chapter 3 the role of cellular water transport in freezing-induced tissue deformation was investigated by development of a semi-empirical representative elementary volume model [50]. In this model, tissue freezing-induced expansion was simulated based on experimentally determined freezing kinetics and cellular water transport characteristics. Results indicate that cellular water transport becomes the critical limiting factor of freezing-induced deformation when cells are present at native tissue like concentrations. In cryopreservation of engineered tissues, with reduced cell content, however extracellular freezing is the dominating factor. In that case it is expected that, deformation rate should increase with increasing cooling rate. As a result, a slow cooling rate is desirable to minimize the freezing-induced deformation of engineered tissues during cryopreservation. In native tissues, competing effects of cooling rate on extracellular freezing and cellular water transport are equally important in determining tissue deformation. In that case, there exists an optimal cooling rate that minimizes deformation of the tissue during cryopreservation. This

optimal cooling rate depends on the composition of the tissue and cellular water transport characteristics of the cells within.

Chapter 4 presented an applied study on biological functionality of collagen based tissue engineering constructs used for improvement of wound healing. Possible effects of freeze/thaw on the ways cells interact with the extracellular matrix were investigated. When fibroblasts, a mechanically active and contractile cell line, were placed on top of collagen hydrogels, they deformed the underlying substrate and migrated on it at the same time. The amount of hydrogel deformation was measured by a newly developed image based tissue deformetry technique. It was found that deformation of ECM is lower in frozen/thawed hydrogels when compared to unfrozen control. However, when the unfrozen collagen microstructure is altered by reducing the collagen concentration of hydrogels, the cell-mediated deformation of the matrix gets increased in agreement with the diminished mechanical properties of the hydrogel. This result indicates that cell-matrix coupling becomes deviant by freeze/thaw of ECM possibly due to poor adhesion between cells and ECM. Interestingly, this freeze/thaw effect on cell-matrix coupling does not cause significant hindrance on cell migration.

In the same study, changes in elastic modulus and hydraulic conductivity were measured independently for freeze/thaw treatment and decreasing collagen concentration. Both freeze/thaw treatment and decreased collagen concentration resulted in a decrease in elastic modulus and an increase in hydraulic conductivity, in agreement with observed changes in microstructure. This was in contrary to deformation response where decreased collagen concentration resulted in significantly higher deformation than reference concentration, which was also higher than freeze/thaw case. Therefore, microstructural changes are unlikely to explain the diminished deformation due to freeze/thaw. The fibril damage in terms of mechanical expansion of fibrils, presented

in Chapter 2 might be the reason for poor cell-matrix adhesion that could also explain the diminished capacity of the cells to deform the frozen/thawed ECM.

The work summarized above addresses three different but related aspects of cryo damage by a combination of rigorous experimentation and computational modeling to characterize post-thaw biomaterial structure and properties, prediction of biomaterial behavior based on underlying biphysical processes and assessment of its biological functionality. The end result is new fundamental knowledge on cryo damage mechanisms and a collection of novel multi-purpose engineering tools that will open the way for rational design of cryomedicine technologies.

LIST OF REFERENCES

LIST OF REFERENCES

[1] B. Rubinsky. Cryosurgery. *Annual Review of Biomedical Engineering*, 2:157187, 2000.

[2] R. W. Habash, R. Bansal, D. Krewski, and H. T. Alhafid. Thermal therapy, part 1: an introduction to thermal therapy. *Crit Rev Biomed Eng*, 34:459489, 2006.

[3] R. Langer and J. P. Vacanti. Tissue engineering. *Science*, 260:920926, 1993.

[4] E. A. Sander and V. H. Barocas. *Biomimetic Collagen Tissues: Collagenous Tissue Engineering and Other Applications Collagen*, page 475504. Springer US, 2008.

[5] E. A. Abou Neel, L. Bozec, J. C. Knowles, O. Syed, V. Mudera, R. Day, and J. K. Hyun. Collagen - emerging collagen based therapies hit the patient. *Advanced Drug Delivery Reviews*, 65(4):429–456, 2013.

[6] J. O. Karlsson and M. Toner. Long-term storage of tissues by cryopreservation: critical issues. *Biomaterials*, 17:243256, 1996.

[7] B. Han and J. Bischof. Direct cell injury associated with eutectic crystallization during freezing. *Cryobiology*, 48(1):8–21, 2004.

[8] G. M. Fahy, B. Wowk, and J. Wu. Cryopreservation of complex systems: the missing link in the regenerative medicine supply chain. *Rejuvenation research*, 9:279291, 2006.

[9] H. T. Meryman. Cryopreservation of living cells: principles and practice. *Transfusion*, 47:935945, 2007.

[10] J. Burk, I. Erbe, D. Berner, J. Kacza, C. Kasper, B. Pfeiffer, K. Winter, and W. Brehm. Freeze-thaw cycles enhance decellularization of large tendons. *Tissue Engineering Part C-Methods*, 20(4):276–284, 2014.

[11] A. Sheytsov, B. Leybovich, I. Artyuhov, Y. Maleev, and A. Peregudov. Production of organ extracellular matrix using a freeze-thaw cycle employing extracellular cryoprotectants. *Cryoletters*, 35(5):400–406, 2014.

[12] A. A. Gage, J. M. Baust, and J. G. Baust. Experimental cryosurgery investigations in vivo. *Cryobiology*, 59:229243, 2009.

[13] B. J. Fuller, N. Lane, and E. E. Benson. *Life in the Frozen State*. CRC Press, Florida, 2004.

[14] Z. Xu, A. Ozcelikkale, Y. L. Kim, and B. Han. Spatiotemporal characterization of extracellular matrix microstructures in engineered tissue: A whole-field spectroscopic imaging approach. *J Nanotechnol Eng Med*, 4:110051110059, 2013.

[15] A. Ozcelikkale, Y. Li, X. Xu, and B. Han. Effects of freezing on collagen nanoscale structure in engineered tissues. In *ASME 2013 2nd Global Congress on NanoEngineering for Medicine and Biology*, Boston, 2013.

[16] K. G. M. Brockbank, K. Schenke-Layland, E. D. Greene, Z. Chen, O. Fritze, M. Schleicher, R. Kaulitz, I. Riemann, F. Fend, J. M. Albes, U. A. Stock, and M. Lisy. Ice-free cryopreservation of heart valve allografts: better extracellular matrix preservation in vivo and preclinical results. *Cell and Tissue Banking*, 13(4):663–671, 2012.

[17] K. Schenke-Layland, J. Xie, S. Heydarkhan-Hagvall, S. F. Hamm-Alvarez, U. A. Stock, K. G. Brockbank, and W. R. MacLellan. Optimized preservation of extracellular matrix in cardiac tissues: implications for long-term graft durability. *Ann Thorac Surg*, 83:16411650, 2007.

[18] D. E. Pegg. The relevance of ice crystal formation for the cryopreservation of tissues and organs. *Cryobiology*, 60:S3644, 2010.

[19] B. Han, J. D. Miller, and J. K. Jung. Freezing-induced fluid-matrix interaction in poroelastic material. *J Biomech Eng*, 131(2):021002, 2009.

[20] P. Mazur. Kinetics of water loss from cells at subzero temperatures and likelihood of intracellular freezing. *The Journal of General Physiology*, 47:347–369, 1963.

[21] M. Toner, E. G. Cravalho, and M. Karel. Thermodynamics and kinetics of intracellular ice formation during freezing of biological cells. *Journal of Applied Physics*, 67:15821593, 1990.

[22] K. Muldrew and L. E. McGann. The osmotic rupture hypothesis of intracellular freezing injury. *Biophys J*, 66:532541, 1994.

[23] J. O. Karlsson. Theoretical analysis of unidirectional intercellular ice propagation in stratified cell clusters. *Cryobiology*, 48:357361, 2004.

[24] K. Y. Teo, J. C. Dutton, and B. Han. Spatiotemporal measurement of freezing-induced deformation of engineered tissues. *J Biomech Eng*, 132:31003, 2010.

[25] K. G. Brockbank, W. R. MacLellan, J. Xie, S. F. Hamm-Alvarez, Z. Z. Chen, and K. Schenke-Layland. Quantitative second harmonic generation imaging of cartilage damage. *Cell and Tissue Banking*, 9:299307, 2008.

[26] V. Isachenko, I. Lapidus, E. Isachenko, A. Krivokharchenko, R. Kreienberg, M. Woriedh, M. Bader, and J. M. Weiss. Human ovarian tissue vitrification versus conventional freezing: morphological, endocrinological, and molecular biological evaluation. *Reproduction*, 138:319327, 2009.

[27] A. Lawson, H. Ahmad, and A. Sambanis. Cytotoxicity effects of cryoprotectants as single-component and cocktail vitrification solutions. *Cryobiology*, 62:115122, 2011.

[28] J. E. Lovelock. The denaturation of lipid-protein complexes as a cause of damage by freezing. *Proceedings of the Royal Society Series B-Biological Sciences*, 147(929):427–433, 1957.

[29] J. C. Bischof and X. He. Thermal stability of proteins. *Annals of the New York Academy of Sciences*, 1066(1):12–33, 2006.

[30] B. S. Bhatnagar, R. H. Bogner, and M. J. Pikal. Protein stability during freezing: Separation of stresses and mechanisms of protein stabilization. *Pharmaceutical Development and Technology*, 12(5):505–523, 2007.

[31] P. L. Privalov. Cold denaturation of protein. *Critical Reviews in Biochemistry and Molecular Biology*, 25:281306, 1990.

[32] G. Graziano, F. Catanzano, A. Riccio, and G. Barone. A reassessment of the molecular origin of cold denaturation. *J Biochem*, 122(2):395–401, 1997.

[33] M. Davidovic, C. Mattea, J. Qvist, and B. Halle. Protein cold denaturation as seen from the solvent. *J Am Chem Soc*, 131:10251036, 2009.

[34] A. Pastore, S. R. Martin, A. Politou, K. C. Kondapalli, T. Stemmler, and P. A. Temussi. Unbiased cold denaturation: Low- and high-temperature unfolding of yeast frataxin under physiological conditions. *Journal of the American Chemical Society*, 129:53745375, 2007.

[35] C. R. Babu, V. J. Hilser, and A. J. Wand. Direct access to the cooperative substructure of proteins and the protein ensemble via cold denaturation. *Nat Struct Mol Biol*, 11:352357, 2004.

[36] E. Reategui and A. Aksan. Effects of water on the structure and low/high temperature stability of confined proteins. *Phys Chem Chem Phys*, 12:1016110172, 2010.

[37] J. C. Bischof, W. F. Wolkers, N. M. Tsvetkova, A. E. Oliver, and J. H. Crowe. Lipid and protein changes due to freezing in dunning at-1 cells. *Cryobiology*, 45:2232, 2002.

[38] T. J. Wess. *Collagen Fibrillar Structure and Hierarchies*, pages 49–80. Springer US, 2008.

[39] R. T. Venkatasubramanian, W. F. Wolkers, M. M. Shenoi, V. H. Barocas, D. Lafontaine, C. L. Soule, P. A. Iaizzo, and J. C. Bischof. Freeze-thaw induced biomechanical changes in arteries: role of collagen matrix and smooth muscle cells. *Ann Biomed Eng*, 38(3):694–706, 2010.

[40] S. Giannini, R. Buda, F. Di Caprio, P. Agati, A. Bigi, V. De Pasquale, and A. Ruggeri. Effects of freezing on the biomechanical and structural properties of human posterior tibial tendons. *International Orthopaedics*, 32(2):145–151, 2008.

[41] P. E. Gelber, G. Gonzalez, J. L. Lloreta, F. Reina, E. Caceres, and J. C. Monllau. Freezing causes changes in the meniscus collagen net: a new ultrastructural meniscus disarray scale. *Knee Surgery Sports Traumatology Arthroscopy*, 16(4):353–359, 2008.

[42] H. J. Park, K. Urabe, K. Naruse, K. Onuma, N. Nemoto, and M. Itoman. The effect of cryopreservation or heating on the mechanical properties and histomorphology of rat bone-patellar tendon-bone. *Cell and Tissue Banking*, 10:1118, 2009.

[43] P. Mazur. Freezing of living cells: mechanisms and implications. *Am J Physiol*, 247(3 Pt 1):C125–42, 1984.

[44] D. J. Smith, M. Schulte, and J. C. Bischof. The effect of dimethylsulfoxide on the water transport response of rat hepatocytes during freezing. *J Biomech Eng*, 120(5):549–58, 1998.

[45] B. Rubinsky and D. E. Pegg. A mathematical model for the freezing process in biological tissue. *Proc R Soc Lond B Biol Sci*, 234:343358, 1988.

[46] G. A. Truskey, F. Yuan, and D. F. Katz. *Transport phenomena in biological systems*. Pearson Prentice Hall, Upper Saddle River, N.J., 2nd edition, 2009.

[47] M. A. Biot. General theory of three-dimensional consolidation. *Journal of Applied Physics*, 12(2):155–164, 1941.

[48] M. B. Albro, N. O. Chahine, M. Caligaris, V. I. Wei, M. Likhitpanichkul, K. W. Ng, C. T. Hung, and G. A. Ateshian. Osmotic loading of spherical gels: a biomimetic study of hindered transport in the cell protoplasm. *J Biomech Eng*, 129:503510, 2007.

[49] A. Ozcelikkale and B. Han. Nano-scale fluid-structure interactions in cytoplasm during freezing. In *Proceedings of the ASME International Mechanical Engineering Congress and Exposition (IMECE2012)*, Houston, TX, 2012.

[50] A. Seawright, A. Ozcelikkale, C. Dutton, and B. Han. Role of cells in freezing-induced cell-fluid-matrix interactions within engineered tissues. *J Biomech Eng*, 135:91001, 2013.

[51] R. O. Hynes. The extracellular matrix: Not just pretty fibrils. *Science*, 326:12161219, 2009.

[52] F. Grinnell and W. M. Petroll. Cell motility and mechanics in three-dimensional collagen matrices. *Annual Review of Cell and Developmental Biology*, 26(1):335–361, 2010.

[53] C. A. Miles, T. V. Burjanadze, and A. J. Bailey. The kinetics of the thermal denaturation of collagen in unrestrained rat tail tendon determined by differential scanning calorimetry. *J Mol Biol*, 245(4):437–46, 1995.

[54] E. I. Tiktopulo and A. V. Kajava. Denaturation of type i collagen fibrils is an endothermic process accompanied by a noticeable change in the partial heat capacity†. *Biochemistry*, 37(22):8147–8152, 1998.

[55] S. Vyazovkin, L. Vincent, and N. Sbirrazzuoli. Thermal denaturation of collagen analyzed by isoconversional method. *Macromolecular Bioscience*, 7:11811186, 2007.

[56] S. J. Lin, W. Lo, H. Y. Tan, J. Y. Chan, W. L. Chen, S. H. Wang, Y. Sun, W. C. Lin, J. S. Chen, C. J. Hsu, J. W. Tjiu, H. S. Yu, S. H. Jee, and C. Y. Dong. Prediction of heat-induced collagen shrinkage by use of second harmonic generation microscopy. *J Biomed Opt*, 11:34020, 2006.

[57] E. Leikina, M. V. Mertts, N. Kuznetsova, and S. Leikin. Type i collagen is thermally unstable at body temperature. *Proceedings of the National Academy of Sciences*, 99:13141318, 2002.

[58] C. A. Miles and M. Ghelashvili. Polymer-in-a-box mechanism for the thermal stabilization of collagen molecules in fibers. *Biophys J*, 76:32433252, 1999.

[59] C. A. Schneider, W. S. Rasband, and K. W. Eliceiri. Nih image to imagej: 25 years of image analysis. *Nature Methods*, 9:671675, 2012.

[60] S. Vyazovkin, A. K. Burnham, J. M. Criado, L. A. Pérez-Maqueda, C. Popescu, and N. Sbirrazzuoli. ICTAC kinetics committee recommendations for performing kinetic computations on thermal analysis data. *Thermochimica Acta*, 520(12):1–19, 2011.

[61] H. J. Borchardt and F. Daniels. The application of differential thermal analysis to the study of reaction kinetics. *Journal of the American Chemical Society*, 79(1):41–46, 1957.

[62] H.-X. Zhou, G. Rivas, and A. P. Minton. Macromolecular crowding and confinement: Biochemical, biophysical, and potential physiological consequences. *Annual Review of Biophysics*, 37:375397, 2008.

[63] M. D. Edwards and S. F. *The Theory of Polymer Dynamics*. Oxford University Press, New York, 1986.

[64] J. Z. Y. Chen. Free energy and extension of a wormlike chain in tube confinement. *Macromolecules*, 46:98379844, 2013.

[65] M. R. Smyda and S. C. Harvey. The entropic cost of polymer confinement. *Journal of Physical Chemistry B*, 116:1092810934, 2012.

[66] D. J. Winzor and C. M. Jackson. Interpretation of the temperature dependence of equilibrium and rate constants. *Journal of Molecular Recognition*, 19(5):389–407, 2006.

[67] J. P. Orgel, J. D. San Antonio, and O. Antipova. Molecular and structural mapping of collagen fibril interactions. *Connect Tissue Res*, 52:217, 2011.

[68] M. Reading and D. J. Hourston. *Modulated Temperature Differential Scanning Calorimetry: Theoretical and Practical Applications in Polymer Characterisation (Hot Topics in Thermal Analysis and Calorimetry)*. Springer, 2006.

[69] K. Y. Teo, T. O. DeHoyos, J. C. Dutton, F. Grinnell, and B. Han. Effects of freezing-induced cell-fluid-matrix interactions on the cells and extracellular matrix of engineered tissues. *Biomaterials*, 32:53805390, 2011.

[70] B. Han, K. Y. Teo, S. Ghosh, J. C. Dutton, and F. Grinnell. Thermomechanical analysis of freezing-induced cell-fluid-matrix interactions in engineered tissues. *Journal of the Mechanical Behavior of Biomedical Materials*, 18:67–80, 2013.

[71] C. A. Miles, N. C. Avery, V. V. Rodin, and A. J. Bailey. The increase in denaturation temperature following cross-linking of collagen is caused by dehydration of the fibres. *Journal of Molecular Biology*, 346(2):551–556, 2005.

[72] M. R. Neidert, R. V. Devireddy, R. T. Tranquillo, and J. C. Bischof. Cryopreservation of collagen-based tissue equivalents. ii. improved freezing in the presence of cryoprotective agents. *Tissue Eng*, 10:2332, 2004.

[73] F. Franks. Protein destabilization at low-temperatures. *Advances in Protein Chemistry, Vol 46*, 46:105–139, 1995.

[74] P. Budrugeac and A. Cucos. Application of kissinger, isoconversional and multivariate non-linear regression methods for evaluation of the mechanism and kinetic parameters of phase transitions of type i collagen. *Thermochimica Acta*, 565(0):241–252, 2013.

[75] J. Saragusty, H. Gacitua, I. Rozenboim, and A. Arav. Do physical forces contribute to cryodamage? *Biotechnol Bioeng*, 104:719728, 2009.

[76] E. J. Woods, J. Liu, C. W. Derrow, F. O. Smith, D. A. Williams, and J. K. Critser. Osmometric and permeability characteristics of human placental/umbilical cord blood CD34+ cells and their application to cryopreservation. *J Hematother Stem Cell Res*, 9(2):161–73, 2000.

[77] J. Choi and J. C. Bischof. Cooling rate dependent biophysical and viability response shift with attachment state in human dermal fibroblast cells. *Cryobiology*, 63(3):285–291, 2011.

[78] S. K. Balasubramanian, J. C. Bischof, and A. Hubel. Water transport and iif parameters for a connective tissue equivalent. *Cryobiology*, 52(1):62–73, 2006.

[79] J. Dong, J. Malsam, J. C. Bischof, A. Hubel, and A. Aksan. Spatial distribution of the state of water in frozen mammalian cells. *Biophysical Journal*, 99(8):2453–2459, 2010.

[80] K. Muldrew, J. Schachar, P. Cheng, C. Rempel, S. Liang, and R. Wan. The possible influence of osmotic poration on cell membrane water permeability. *Cryobiology*, 58(1):62–8, 2009.

[81] E. H. Zhou, X. Trepat, C. Y. Park, G. Lenormand, M. N. Oliver, S. M. Mijailovich, C. Hardin, D. A. Weitz, J. P. Butler, and J. J. Fredberg. Universal behavior of the osmotically compressed cell and its analogy to the colloidal glass transition. *Proceedings of the National Academy of Sciences of the United States of America*, 106:1063210637, 2009.

[82] S. Ghosh, J. C. Dutton, and B. Han. Measurement of spatiotemporal intracellular deformation of cells adhered to collagen matrix during freezing of biomaterials. *Journal of Biomechanical Engineering-Transactions of the Asme*, 136(2), 2014.

[83] R. V. Devireddy, D. J. Swanlund, K. P. Roberts, and J. C. Bischof. Subzero water permeability parameters of mouse spermatozoa in the presence of extracellular ice and cryoprotective agents. *Biol Reprod*, 61:764775, 1999.

[84] M. Akhoondi, H. Oldenhof, C. Stoll, H. Sieme, and W. F. Wolkers. Membrane hydraulic permeability changes during cooling of mammalian cells. *Biochim Biophys Acta*, 1808(3):642–8, 2011.

[85] F. Grinnell and B. Geiger. Interaction of fibronectin-coated beads with attached and spread fibroblasts: Binding, phagocytosis, and cytoskeletal reorganization. *Experimental Cell Research*, 162(2):449–461, 1986.

[86] R. V. Devireddy and J. C. Bischof. Measurement of water transport during freezing in mammalian liver tissue: Part iiâ€"the use of differential scanning calorimetry. *Journal of Biomechanical Engineering*, 120:559569, 1998.

[87] J. Schindelin, I. Arganda-Carreras, E. Frise, V. Kaynig, M. Longair, T. Pietzsch, S. Preibisch, C. Rueden, S. Saalfeld, B. Schmid, J.-Y. Tinevez, D. J. White, V. Hartenstein, K. Eliceiri, P. Tomancak, and A. Cardona. Fiji: an open-source platform for biological-image analysis. *Nat Methods*, 9:676682, 2012.

[88] M. Toner, R. G. Tompkins, E. G. Cravalho, and M. L. Yarmush. Transport phenomena during freezing of isolated hepatocytes. *Aiche Journal*, 38(10):1512–1522, 1992.

[89] R. L. Levin, E. G. Cravalho, and C. E. Huggins. A membrane model describing the effect of temperature on the water conductivity of erythrocyte membranes at subzero temperatures. *Cryobiology*, 13(4):415–29, 1976.

[90] K. Levenberg. A method for the solution of certain non-linear problems in least squares. *Quarterly of Applied Mathematics*, 2:164–168, 1944.

[91] G. T. Charras, M. Coughlin, T. J. Mitchison, and L. Mahadevan. Life and times of a cellular bleb. *Biophys J*, 94(5):1836–53, 2008.

[92] J. M. Kim and R. R. Parizek. A mathematical model for the hydraulic properties of deforming porous media. *Ground Water*, 37(4):546–554, 1999.

[93] R. V. Devireddy, D. J. Swanlund, T. Olin, W. Vincente, M. H. Troedsson, J. C. Bischof, and K. P. Roberts. Cryopreservation of equine sperm: optimal cooling rates in the presence and absence of cryoprotective agents determined using differential scanning calorimetry. *Biol Reprod*, 66:222231, 2002.

[94] R. V. Devireddy, S. Thirumala, and J. M. Gimble. Cellular response of adipose derived passage-4 adult stem cells to freezing stress. *J Biomech Eng*, 127:10811086, 2005.

[95] V. Ragoonanan, A. Hubel, and A. Aksan. Response of the cell membrane-cytoskeleton complex to osmotic and freeze/thaw stresses. *Cryobiology*, 61(3):335–44, 2010.

[96] R. Magalhães, B. Nugraha, S. Pervaiz, H. Yu, and L. L. Kuleshova. Influence of cell culture configuration on the post-cryopreservation viability of primary rat hepatocytes. *Biomaterials*, 33(3):829–836, 2012.

[97] T. M. Quinn, E. B. Hunziker, and H. J. Hauselmann. Variation of cell and matrix morphologies in articular cartilage among locations in the adult human knee. *Osteoarthritis Cartilage*, 13:672678, 2005.

[98] G. Vunjak-Novakovic, N. Tandon, A. Godier, R. Maidhof, A. Marsano, T. P. Martens, and M. Radisic. Challenges in cardiac tissue engineering. *Tissue Eng Part B Rev*, 16:169187, 2010.

[99] R. E. Pitt. Cryobiological implications of different methods of calculating the chemical-potential of water in partially frozen suspending media. *Cryo-Letters*, 11:227240, 1990.

[100] P. V. Pazhayannur and J. C. Bischof. Measurement and simulation of water transport during freezing in mammalian liver tissue. *J Biomech Eng*, 119:269277, 1997.

[101] G. M. Abouna. Organ shortage crisis: Problems and possible solutions. *Transplantation Proceedings*, 40(1):34–38, 2008.

[102] K. C. Broussard and J. G. Powers. Wound dressings: Selecting the most appropriate type. *American Journal of Clinical Dermatology*, 14:449–459, 2013.

[103] A. J. Singer and R. A. F. Clark. Cutaneous wound healing. *New England Journal of Medicine*, 341(10):738–746, 1999.

[104] D. E. Discher, P. Janmey, and Y. L. Wang. Tissue cells feel and respond to the stiffness of their substrate. *Science*, 310:11391143, 2005.

[105] C. Wiegand and R. White. Microdeformation in wound healing. *Wound Repair and Regeneration*, 21:793799, 2013.

[106] C. M. Lo, H. B. Wang, M. Dembo, and Y. L. Wang. Cell movement is guided by the rigidity of the substrate. *Biophysical Journal*, 79:144152, 2000.

[107] W. H. Guo, M. T. Frey, N. A. Burnham, and Y. L. Wang. Substrate rigidity regulates the formation and maintenance of tissues. *Biophysical Journal*, 90:22132220, 2006.

[108] E. Hadjipanayi, V. Mudera, and R. A. Brown. Guiding cell migration in 3D: a collagen matrix with graded directional stiffness. *Cell Motil Cytoskeleton*, 66(3):121–8, 2009.

[109] M. Miron-Mendoza, J. Seemann, and F. Grinnell. The differential regulation of cell motile activity through matrix stiffness and porosity in three dimensional collagen matrices. *Biomaterials*, 31(25):6425–6435, 2010.

[110] S. A. McClain, M. Simon, E. Jones, A. Nandi, J. O. Gailit, M. G. Tonnesen, D. Newman, and R. A. F. Clark. Mesenchymal cell activation is the rate-limiting step of granulation tissue induction. *American Journal of Pathology*, 149(4):1257–1270, 1996.

[111] Z. Pan, K. Ghosh, V. Hung, L. K. Macri, J. Einhorn, D. Bhatnagar, M. Simon, R. A. F. Clark, and M. H. Rafailovich. Deformation gradients imprint the direction and speed of en masse fibroblast migration for fast healing. *Journal of Investigative Dermatology*, 133:24712479, 2013.

[112] X. Trepat, M. R. Wasserman, T. E. Angelini, E. Millet, D. A. Weitz, J. P. Butler, and J. J. Fredberg. Physical forces during collective cell migration. *Nature Physics*, 5(6):426–430, 2009.

[113] X. Serra-Picamal, V. Conte, R. Vincent, E. Anon, D. T. Tambe, E. Bazellieres, J. P. Butler, J. J. Fredberg, and X. Trepat. Mechanical waves during tissue expansion. *Nature Physics*, 8:628634, 2012.

[114] B. A. Roeder, K. Kokini, J. P. Robinson, and S. L. Voytik-Harbin. Local, three-dimensional strain measurements within largely deformed extracellular matrix constructs. *Journal of Biomechanical Engineering-Transactions of the Asme*, 126(6):699–708, 2004.

[115] B. A. Roeder, K. Kokini, and S. L. Voytik-Harbin. Fibril microstructure affects strain transmission within collagen extracellular matrices. *Journal of Biomechanical Engineering-Transactions of the Asme*, 131(3), 2009.

[116] C. G. Armstrong, W. M. Lai, and V. C. Mow. An analysis of the unconfined compression of articular-cartilage. *Journal of Biomechanical Engineering-Transactions of the Asme*, 106(2):165–173, 1984.

[117] C. E. Willert and M. Gharib. Digital particle image velocimetry. *Experiments in Fluids*, 10(4):181–193, 1991.

[118] F. Scarano. Iterative image deformation methods in piv. *Measurement Science & Technology*, 13(1):R1–R19, 2002.

[119] K. Jaqaman, D. Loerke, M. Mettlen, H. Kuwata, S. Grinstein, S. L. Schmid, and G. Danuser. Robust single-particle tracking in live-cell time-lapse sequences. *Nature Methods*, 5(8):695–702, 2008.

[120] A. F. Bower. *Applied mechanics of solids*. CRC press, 2009.

[121] D. J. S. Hulmes. *Collagen Diversity, Synthesis and Assembly Collagen*, page 1547. Springer US, 2008.

[122] C. A. Miles. Kinetics of collagen denaturation in mammalian lens capsules studied by differential scanning calorimetry. *Int J Biol Macromol*, 15:265271, 1993.

VITA

VITA

Altug Ozcelikkale holds M.S. and B.S. degrees in Mechanical Engineering from Middle East Technical University (METU) in Ankara, Turkey. He held the first place in the department rankings through his undergraduate studies in METU and graduated in second place in university rankings. He continued his graduate studies in the same department where he worked on development and implementation of a computational tool for automated solution of incompressible laminar flow problems with minimum user intervention based on adaptive refinement strategies.

Altug joined the Ph.D. program in School of Mechanical Engineering at Purdue University where he received the Ross Fellowship for the first year of his studies. During his Ph.D. studies, he worked as a graduate research assistant in Biotransport Phenomena Lab and performed research on various areas including biomedical device development for chemotherapy drug testing, drug delivery for cancer therapy, transport characteristics of nanoparticles and drug molecules, freezing-induced deformation of cell and tissues in cryomedical applications and soft tissue extracellular matrix mechanics during cell migration. His research have been published in several peer-reviewed journal articles and were presented in numerous conferences where he received an outstanding paper award for his work on collagen fibril-level freezing damage. Upon graduation in 2015, Altug will remain at Purdue University for an additional year as a post-doctoral researcher. He can be reached by email at altugozcelikkale@gmail.com.